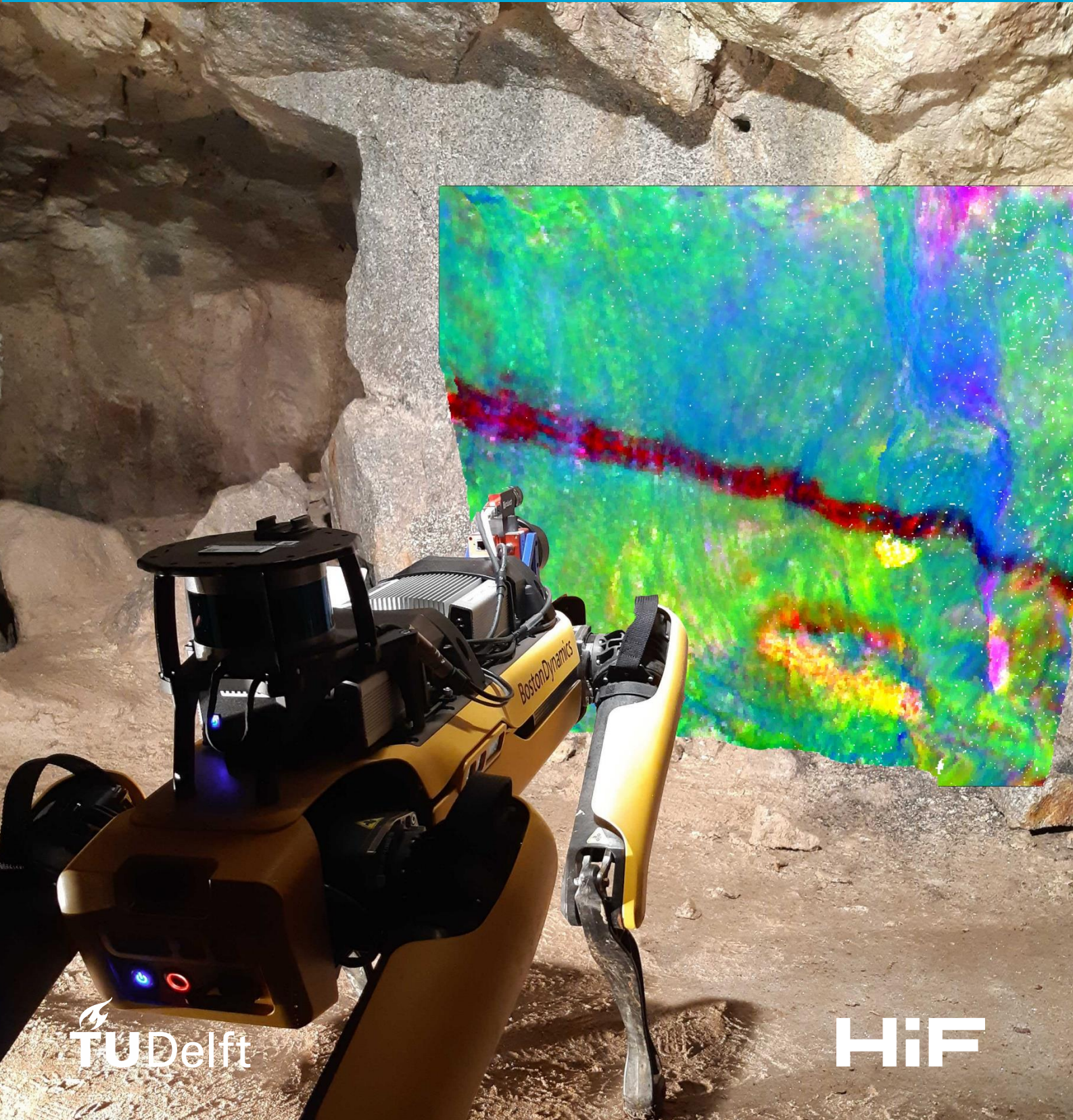


# Robot-aided Hyperspectral Imaging For Mineral Exploration in Underground Mining Environments

Sibren Dieters





# Robot-aided Hyperspectral Imaging for Mineral Exploration in Underground Mining Environments

By

S. Dieters

in partial fulfilment of the requirements for the degree of

**Master of Science**  
in Applied Earth Sciences  
European Mining Course (EMC)

at the Delft University of Technology,  
to be defended publicly on Thursday November 2nd, 2023 at 11:00 AM.

|                   |   |  |
|-------------------|---|--|
| Supervisor:       | Dr. T. Schmiedel  | TU Delft   |
| Thesis committee: | Dr. T. Schmiedel,<br>Dr. R.C. Lindenberg,<br>Prof. Dr. B. Lottermoser,<br>Dr. J. Leveinen | TU Delft<br>TU Delft<br>RWTH Aachen University<br>Aalto University |
| Advisors:         | Dr. S. Lorenz,<br>Dr. M. Kirsch   | Helmholtz Institute Freiberg<br>Helmholtz Institute Freiberg       |

*This thesis is confidential and cannot be made public until October 26th, 2023.*

An electronic version of this thesis is available at <http://repository.tudelft.nl/>.



# Preface

This thesis presents the research conducted by Sibren Dieters on developing a robot-aided hyperspectral imaging method for mineral exploration in underground mining environments. The research is conducted at the Helmholtz Institute Freiberg for Resource Technology (HIF) Department for Exploration under the supervision of Tobias Schmiedel (TUDelft), Sandra Lorenz and Moritz Kirsch (Helmholtz Institute Freiberg). The research is completed for the fulfilment for the degree in Master of Science as part of the European Mining Course (EMC) program at TU Delft, RWTH Aachen and Aalto University.

|                  |   |  |
|------------------|---|--|
| Title            | : | Robot-aided Hyperspectral Imaging for Mineral Exploration in Underground Mining Environments   |
| Author           | : | Sibren Dieters   |
| Date             | : | 02-11-2023   |
| Supervisor       | : | Dr. T. Schmiedel<br>TU Delft   |
| Thesis committee | : | Dr. T. Schmiedel, TU Delft<br>Dr. R.C. Lindenbergh, TU Delft<br>Prof. Dr. B. Lottermoser, RWTH Aachen University<br>Dr. J. Leveinen Aalto University           |
| Advisors         | : | Dr. S Lorenz, Helmholtz Institute Freiberg<br>Dr. M. Kirsch Helmholtz Institute Freiberg   |
| Address          | : | Section of Resource Engineering<br>Department of Geosciences & Engineering<br>Delft University of Technology<br>Stevinweg 1<br>2628CN Delft<br>The Netherlands |

*All rights reserved.  
No parts of this publication may be reproduced,  
Stored in a retrieval system, or transmitted,  
In any form or by any means, electronic,  
Mechanical, photocopying, recording, or otherwise,  
Without the prior written permission of the  
Section for Resource Engineering*



# Contents

|   |           |
|---|-----------|
| Abstract.....                                   | 9         |
| Acknowledgements .....                          | 10        |
| <b>1 Introduction.....</b>                      | <b>11</b> |
| 1.1 Mineral Exploration.....                    | 11        |
| 1.2 Hyperspectral Imaging .....                 | 11        |
| 1.3 Robot-aided Data Acquisition .....          | 12        |
| 1.4 Scope of the Thesis.....                    | 12        |
| 1.5 Geological Setting .....                    | 13        |
| 1.5.1 Regional Geology .....                    | 13        |
| 1.5.2 Zinnwald/Cinnovec Deposit and Mine .....  | 14        |
| 1.5.3 Spectral Theory and Characteristics ..... | 15        |
| <b>2 Equipment and Instruments.....</b>         | <b>17</b> |
| 2.1 Boston Dynamics Spot .....                  | 17        |
| 2.1.1 Hardware .....                            | 17        |
| 2.1.2 CORE Computer.....                        | 18        |
| 2.1.3 Controlling Spot .....                    | 18        |
| 2.2 Payload Configuration .....                 | 19        |
| 2.3 Cubert ULTRISX20P .....                     | 21        |
| 2.3.1 Hardware .....                            | 21        |
| 2.3.2 CUVIS SDK .....                           | 22        |
| 2.4 Velodyne VLP16 .....                        | 22        |
| 2.4.1 Hardware .....                            | 22        |
| 2.4.2 Velodyne Driver .....                     | 24        |
| 2.5 Network and Command Configuration.....      | 24        |
| <b>3 Methods.....</b>                           | <b>25</b> |
| 3.1 General Workflow.....                       | 25        |
| 3.2 Hyperspectral Data.....                     | 26        |
| 3.3 LiDAR Data .....                            | 29        |
| 3.4 Hypercloud Projection .....                 | 30        |
| 3.5 Application of Proposed Workflow .....      | 30        |
| 3.5.1 Exposure Time Study.....                  | 30        |
| 3.5.2 Lab Application .....                     | 30        |
| 3.5.3 Underground Application .....             | 32        |
| 3.6 Validation .....                            | 33        |
| <b>4 Results .....</b>                          | <b>34</b> |
| 4.1 Lab Application.....                        | 34        |
| 4.1.1 Exposure Time Comparison.....             | 34        |
| 4.1.2 RGB Image.....                            | 35        |
| 4.1.3 Band Ratio Analysis.....                  | 35        |
| 4.1.3 MNF and PCA.....                          | 36        |
| 4.1.4 Endmember Extraction .....                | 36        |
| 4.1.5 Abundance Maps.....                       | 37        |
| 4.1.2 LiDAR Pointcloud.....                     | 38        |
| 4.1.3 Hyperclouds.....                          | 39        |
| 4.2 Underground .....                           | 41        |
| 4.2.1 Exposure Time Comparison.....             | 41        |

|   |           |
|---|-----------|
| 4.2.2 LiDAR Pointcloud.....                                   | 42        |
| 4.2.3 UG-1 Hyperclouds .....                                  | 42        |
| 4.2.4 UG-2 Hyperclouds .....                                  | 45        |
| <b>5 Discussion .....</b>                                     | <b>48</b> |
| 5.1 Hyperspectral .....                                       | 48        |
| 5.1.1 Exposure Time.....                                      | 48        |
| 5.1.2 Band Ratio Analysis.....                                | 48        |
| 5.1.3 Mineral Correlation.....                                | 49        |
| 5.1.4 Mineral Context.....                                    | 50        |
| 5.2 LiDAR Pointcloud .....                                    | 53        |
| <b>6 Error Analysis .....</b>                                 | <b>54</b> |
| 6.1 Hypercloud Merging Artefacts .....                        | 54        |
| 6.2 Halo Effect.....  | 54        |
| <b>7 Conclusion .....</b>                                     | <b>56</b> |
| 7.1 Future Research .....                                     | 57        |
| 7.2 Outlook.....  | 57        |
| <b>Bibliography.....</b>                                      | <b>58</b> |
| <b>8 Appendices .....</b>                                     | <b>64</b> |
| Appendix A: MNF and PCA Output .....                          | 64        |
| Appendix B: Analysis.....                                     | 69        |
| Appendix C: Digital Hyperclouds .....                         | 74        |
| Appendix D: Cubert X20P Manual for HIF .....                  | 75        |
| Appendix E: Operation and Data Acquisition Guide for HIF..... | 75        |

## Abstract

New mining and exploration projects have revived across Europe with an increasing demand for critical raw materials driven by the energy transition and unstable political conditions. Hyperspectral imaging proves to be an excellent tool for quick and efficient non-invasive mineral exploration. By mounting hyperspectral- and LiDAR sensors on drones and other robots, inaccessible and dangerous areas can safely be mapped for geological information. With increasingly deeper and more hazardous underground mines, a robot-aided hyperspectral mineral exploration method in underground environments is needed. This study configures a Cubert X20P hyperspectral camera (VNIR) and VLP16 LiDAR on the versatile Boston Dynamics Spot robot, creating a multi-sensor robotic platform for data acquisition in underground mining environments. A data workflow is proposed and applied to the granite greisen rocks of the Zinnwald/Cinnovec mine (Germany). Combining hyperspectral and geometric data provides unique 3D hypercloud results interpreted for mineral and structural features. Hyperspectral analysis successfully identifies iron and clay minerals along with multiple vein and fault structures. A remote mineral exploration method in underground mines significantly improves safety by keeping the operator away from hazardous areas. The proposed platform and workflow show potential to contribute to underground mineral exploration, especially if future improvements in data quality and autonomous capabilities are made.

## Acknowledgements

My deepest gratitude goes to my supervisor Dr. Tobias Schmiedel who helped me find this research opportunity and aided me during the research with his unrivalled support and critical mindset. He was always available for questions and involved in my future academic development. I would also like to thank my advisors at the institute, Dr. Sandra Lorenz and Dr. Moritz Kirsch for their incredible guidance and lessons that taught me about hyperspectral imaging and mineral exploration.

I have felt incredibly welcome during my time in Freiberg and it has been my greatest pleasure to work with the Exploration department at HIF. Many thanks to the members of the team especially Yuleika Madriz Diaz, Gopi Regular, Junaidh Shaik Fareedh, Atilla Barış Başıoğlu and Dr. Sam Thiele. The Helmholtz Institute Freiberg has allowed me to develop in a professional and cooperative environment for which I am deeply grateful. The research would not have been possible without the equipment and instruments provided by HIF, for which I would like to thank Dr. Richard Gloaguen.

A special thanks to my family and Julia for their loving support and visits in Freiberg. I also want to thank all my friends in Utrecht and the entire EMC cohort for their friendship and motivation throughout my master's degree, especially Aditya Krishnan who has been my companion and discussion partner during our time at HIF.

# 1 Introduction

## 1.1 Mineral Exploration

Due to an increasing demand for critical raw materials in Europe (European Commission, 2014), the need for new mining projects on European territory has been revived. Despite Europe being rich in critical raw material resources (Bertrand et al., 2016), it is difficult to create economically feasible mineral reserves due to high mining costs, strict environmental policies, and increasingly complex ore bodies. These factors are more fortunate in other parts of the world, such as Asia, Africa, and South America. By importing most of the critical raw materials from different continents, Europe creates a supply dependency and risk (European Commission, 2020). Unstable political, pandemic and climate conditions could disrupt the supply chain and halt the European transition to renewable energy or fail to supply basic material demands. In addition to material supply, Europe aims for a decarbonised economy and energy industry. The energy transition is a transfer from a fossil fuel to a critical metals supply for green, non-carbonizing energy technologies, which add to the demand for critical metals.

Underground mineral exploration will become increasingly important with the rise of global share in underground mines (Martino et al., 2021). With increasingly depleted surface reserves, high costs and the ambition of the mining industry to reduce its environmental footprint, deeper ore deposits will be considered for exploitation (Nwaila et al., 2022; Sahu et al., 2015). Underground mining is a highly selective mining method compared to open-pit mining. Where significant gangue characterises open-pit mining, underground mining can directly exploit ore rock without overburden removal. Innovative mining and exploration methods are needed to reduce costs and support new or existing reserve studies to improve conditions for resourcing critical raw materials in Europe. The complex nature of underground mining and ore bodies requires a quick and cost-efficient method for large-scale mineral exploration. Underground geological mapping traditionally uses invasive drill core extraction and geochemical analysis. Non-invasive exploration methods, such as hyperspectral imaging, can contribute to large-scale and cost-efficient mineral exploration methods that comply with European exploration policy, which aims to minimise environmental footprint (Ares, 2018). This way, hyperspectral imaging can support mineral exploration studies in increasingly important underground mining environments and improve conditions for future mining and exploration in Europe.

## 1.2 Hyperspectral Imaging

Hyperspectral imaging is a remote sensing tool for analysing surface characteristics or processes. It has shown its worth in various applications, such as agriculture and geological surveys (Lu et al., 2020; van der Meer et al., 2012; Zhou et al., 2017). Hyperspectral data can be processed into geological products like mineral abundance maps. These products support effective decision-making in, for example, exploration, mine planning, process control and geotechnical risk assessments. Geological products affect decision-making and directly impact mining or exploration operations (Michalakopoulos, 2000).

Multiple types of information can be obtained from hyperspectral imaging used for geological products and mapping. Geometric information can be used for Rock Mass Classification, structural mapping and other geotechnical purposes. Mineralogical data provides information about mineral assemblages or distribution. Conventionally, these data types are analysed and interpreted separately. However, it has been shown that combining geometric and spectral data into a so-called 'hypercloud' gives new insights and opportunities for geological interpretation (Buckley et al., 2013; Thiele et al., 2021). This method has been widely used for outcrop mapping purposes and has shown its value in open-pit mines (Buckley et al., 2013; Kurz et al., 2011).

In a recent study, Kirsch et al. (2023) showed the potential and feasibility of underground hyperspectral imaging despite suboptimal illuminating conditions, irregular topography, moisture, and limited accessibility. The study proposed a workflow for underground mineral exploration, which was validated by a lab and case study. However, geological mapping and data acquisition can be risky in underground mining environments. These environments are known to be potentially hazardous for humans. Major hazards include tunnel collapse, raveling (shallow mines), gas combustions, poor air quality, extreme temperatures, and inaccessibility (Howden Company, 2019). The hazard's impact and probability increase with the increasing depth of mining operations. Therefore, a safer method for underground geological mapping and hyperspectral imaging is needed to produce similar data quality and information as (Kirsch et al., 2023b) showed in the study of underground hyperspectral imaging.

### 1.3 Robot-aided Data Acquisition

Robot-aided data acquisition for mineral exploration provides a solution for a safe and efficient method for hyperspectral data acquisition and has proven its value in many previous studies (Booyesen et al., 2020; Hyunseob et al., 2023a; Kirsch et al., 2018). Uncrewed Aerial Vehicles (UAVs), or drones equipped with hyperspectral sensors, have been shown to produce high-quality mineral information. Using drones with mounted LiDAR and hyperspectral sensors provides an agile and effective method of mineral exploration in environments deemed inaccessible or hazardous for humans. Drones can be equipped with spherical bumpers or advanced anti-collisional systems to enhance manoeuvrability in underground environments (Mahmud, 2021; Wang et al., 2023). Alternatively, Uncrewed ground Vehicles (UV) mounted with similar LiDAR and hyperspectral sensors can manoeuvre through more narrow environments. Previous studies have shown the potential of wheeled uncrewed vehicles in underground data acquisition and reality capture (Hyunseob et al., 2023b; Koval et al., 2022).

### 1.4 Scope of the Thesis

This thesis aims to develop and validate a robot-aided hyperspectral imaging method for mineral exploration in underground mining environments. The research is conducted at the Helmholtz Institute Freiberg for Resource Technology (HIF) Department for Exploration, which specialises in developing innovative methods for hyperspectral imaging for mineral exploration and has significant expertise in performing data acquisition missions with manually controlled drones for many outcrop types and lithologies.

A Boston Dynamics Spot forms the basis for the multi-sensor platform. The Spot robot has proven itself in underground and construction environments, performing data acquisition or safety-related tasks (Lindqvist et al., 2022; Wetzal et al., 2022). The Spot robot platform provides a multifunctional and highly customisable platform for remote operations. Spot is equipped with a lightweight Cubert X20P hyperspectral camera (VNIR) and a compact Velodyne VLP16 LiDAR laser scanner. Both instruments are provided and maintained by HIF.

This study concerns the correct configuration of instruments on the Spot robotic platform to achieve a functioning multi-sensor system. Then, a workflow is proposed for hyperspectral and geometric data acquisition. This involves Spot walking up to the target outcrop, acquiring data, and moving to the next target. The workflow further includes corrections and processing the geometric and hyperspectral data into pointcloud and hyperspectral data cubes or combining the data into so-called 'hyperclouds'. These hyperclouds are then interpreted in terms of mineral and geological information.

The proposed workflow is applied to a dark lab environment using artificial lighting to simulate underground conditions and an underground case study. The lab test is performed on samples from the Zinnwald/Cinnovec visitors mine in Germany. These samples were also used by Kirsch et al. (2023) with a non-robotic sensor tripod setup. The results from Kirsch et al. (2023) are then used to compare and validate the acquired data and processing workflow. After a successful lab test, an underground acquisition is performed in the Zinnwald/Cinnovec mine and localities as a case study. The Zinnwald/Cinnovec mine is a

historic Sn-W mine and is accessed by horizontal adits, making it easily accessible and suitable for scientific testing. The underground conditions are representative of shallow underground mining conditions. The feasibility and quality of the developed method can be appropriately evaluated by conducting a lab test, an underground case study, and using an existing study for validation. Although the method involves many manual steps, this thesis provides a solid foundation for future process optimisation and automation of the platform.

## 1.5 Geological Setting

### 1.5.1 Regional Geology

The Zinnwald/Cinnovec mine is located in the Eastern Erzgebirge and part of the Saxo Thuringian Zone, which formed during the late Variscan orogeny. Late- and post-collisional processes of uplift and exhumation caused widespread felsic magmatism, forming multiple volcano-plutonic complexes in the crust, including the largest Altenberg-Teplice caldera (ATC), as a result of orogeny-related crustal extension and rapid uplift, granitic and rhyolitic rocks extruded and intruded along an NNW-striking fault zone, forming the caldera (Breiter et al., 1999; Tischendorf & Förster, 1990). These rocks have been shown to originate from a heterogeneous source region without basic magma input (Casas-García et al., 2021) and have formed over a 15Ma period during the Variscan post-collisional collapse (Romer et al., 2007a). The extruding granites and rhyolites resulted in syn-collapse fill, forming a thick sequence of several rhyolite formations. The caldera complex is covered by younger sedimentary and volcanic successions, forming the current geological surface structures shown in Figure 1.1 (A).

The caldera formation was followed by two phases of albite granitoid magmatism (Tomek et al., 2022). The granites successively intruded into the Altenberg-Teplice caldera. The oldest Niederbobritzsch granites intruded at 328–314 Ma, followed by topaz-bearing rare metal granites at 326–308 Ma (Romer et al., 2007b). These younger intrusions are related to the Schellerhau granite and smaller Zinnwald/Cinnovec Sn-W granitoid intrusion, containing Li-Fe mica mineralisation (Breiter et al., 1999; Förster, 1999; Seifert et al., 2011; Štemprok et al., 2003). The Zinnwald/Cinnovec albite granite roughly strikes N-S and crosses the German-Czech border, as shown in Figure 1.1 (B).

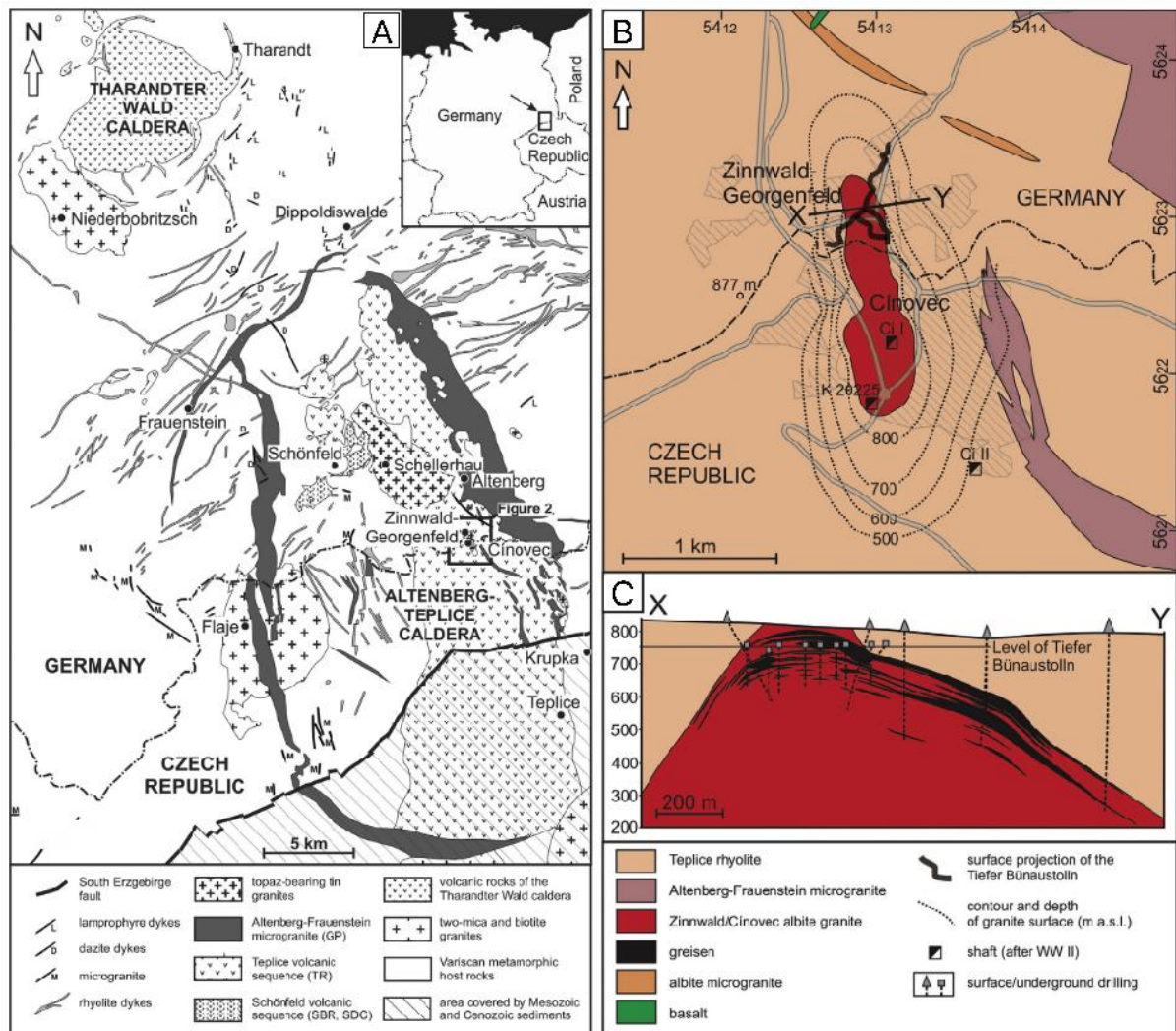


**Figure 1.** (A) Geological map of the Altenberg-Teplice Caldera and surroundings. (B) Zinnwald/Cinnovec albite granite with Tiefen Bünaustollen adit, and (C) cross-section, modified from Müller et al. [33].

### 1.5.2 Zinnwald/Cinnovec Deposit and Mine

Compared to the older Niederbobritzsch granites, the younger Zinnwald/Cinnovec granites show the highest level of differentiation in the granites and rare metal content (Förster, 1999). The Zinnwald/Cinnovec granite is unique in its abundance of Li-Fe mica mineralisation. These micas show great chemical diversity and are typical for greisen granites. They occur in either the host rock or hydrothermal veins (Rieder, 1970). Among the Li-Fe micas is the relatively high Li-content mineral called zinnwaldite. Considering its Li-enrichment, this mineralisation is economically attractive in current exploration projects (Dittrich, 2020). Several processes allowed Li and rare metal enrichment in the Zinnwald/Cinnovec albite granite. During the pluton's slow cooling, hydrothermal fluids could move along brittle structures as pathways towards the top of the pluton. These magmatic-derived Li-rich fluids altered the rock into greisen granites along the pluton edges, as shown in Figure 1.1 (C) (Förster, 1999). Horizontal and sub-horizontal structures of greisen alterations were formed along the top of the pluton. These greisen granites are characterised by generally low Ge/Al ratios, allowing uptake of Li in the quartz crystal lattice (Müller et al., 2018), forming the strongly Li-enriched zinnwaldite minerals. The ore rock consists of these massive greisen granites, including smaller sub-horizontal coarse quartz-zinnwaldite-casserite veins. Epigenetic processes like hematization and argillitization altered the greisen rock surface, forming accessory oxides and clays (Müller et al., 2018; Štemprok & Šulcek, 1969). Oxidation and kaolinisation of the Li-Fe mica zinnwaldite lead to the formation of iron minerals and kaolinite on the rock surface (Štemprok & Šulcek, 1969). Kaolinisation regularly occurs

along hydrothermal vein structures and can also be seen along the sub-horizontal vein structures in the Zinnwald/Cinnovec mine (Müller et al., 2018; Stoch & Sikora, 1976).

Originally called Flöz, these vein structures defined mine works along the Tiefer Bünaustolln adit. When a vein was found, a stope or Flözgange was mined along its strike, creating many mine caverns. This study collects data from multiple surfaces in Flöz 8, similar to Kirsch et al. (2023). The selected outcrops contain the greisen granites (quartz, zinnwaldite, muscovite, k-feldspar, topaz, kaolinite, and fluorite), the quartz-zinnwaldite veins and additional clay or hematite alterations. Flöz 8 was chosen for this study because it is considered a high-grade zone and the availability of an already existing dataset and hyperspectral study. The stope floor is irregular; therefore, it is a good representation of underground conditions to test the robotic configuration and workflow.

### *1.5.3 Spectral Theory and Characteristics*

Hyperspectral imaging is based on the principle of capturing spectral reflectance of a surface or target. Light, in the form of photonic energy from the sun or an artificial source, reaches the target where it interacts with the particles on the surface. Some of the photon energy is absorbed, and the majority of the energy is reflected away from the surface. Each mineral or element will behave differently when struck by photonic energy based on its crystallographic or molecular structure. This causes the photonic energy to be absorbed at different wavelengths in the electromagnetic spectrum, creating distinct spectral absorption features. The absorbed photonic energy creates minima in the total electromagnetic spectrum captured by the hyperspectral sensor. The difference in absorbed and reflected energy is characteristic of the mineral or element (EIMasry & Sun, 2010). By correlating absorption features to known minerals, the target surface can be classified in terms of mineralogy (Laukamp et al., 2021).

Different types of hyperspectral cameras or sensors are designed for specific ranges in the visible and infrared part of the electromagnetic spectrum, such as the near (VNIR), shortwave (SWIR), mid-wave (MWIR) and long-wave (LWIR) infrared. Minerals have diagnostic absorption features in different spectral ranges, meaning not all minerals can be identified in the VNIR range (Clark, 1999; Pontual et al., 1997).

Based on the mineral assemblages and alteration minerals of the Flöz 8 in the Zinnwald/Cinnovec mine, a spectral library is formed. This library shows what spectral signatures to expect based on present minerals. Since the hyperspectral study is in the VNIR range, only spectral characteristics in this range are considered. A library reflectance spectrum is a spectrum from a specific mineral acquired under an ideal illuminating condition. The library reflectance in the VNIR range of the most abundant minerals in the sample material and outcrop, as mentioned in section 1.5.2, is shown in Figure 1.2. Mineral spectra in the VNIR range are commonly characterised by the absorption of light due to electron and charge transitions at atomic scale. Electron transition metals like Fe, Cr, Co and Ni have discrete energy states and absorb some photonic energy, resulting in electron transitions in the crystal lattice (Clark, 1999; Zhou et al., 2017). Charge transfer absorption occurs when a metal changes valence states and transfers the absorbed photonic energy. In our setting, this occurs as the distinct transition of ferrous to ferric iron. However, these features can occur over a range of wavelengths due to variations in mineral orientation, chemical composition and crystallographic structure (Figure 1.2). These spectral features can be seen in the library spectra of iron-bearing minerals like jarosite, hematite, and goethite. Zinnwaldite, being a Li-Fe mica, shows a ferrous-ion absorption feature. Ferric-iron-bearing minerals can also be characterised by identifying the typical 570 to 600 nm slope, as indicated in Figure 1.2. The library spectra are plotted without hull correction to improve the visibility of ferrous iron features in the spectra (Murphy & Monteiro, 2012; Pontual et al., 1997). Other present minerals like kaolinite, quartz, topaz, and muscovite do not have diagnostic spectral features in the VNIR range. However, they can be distinguished by looking at diagnostic slopes or absolute reflectance (Clark, 1999). Kaolinite can be distinguished by a gradually increasing reflectance spectrum towards the 1000 nm wavelength, as seen in Figure 1.2.

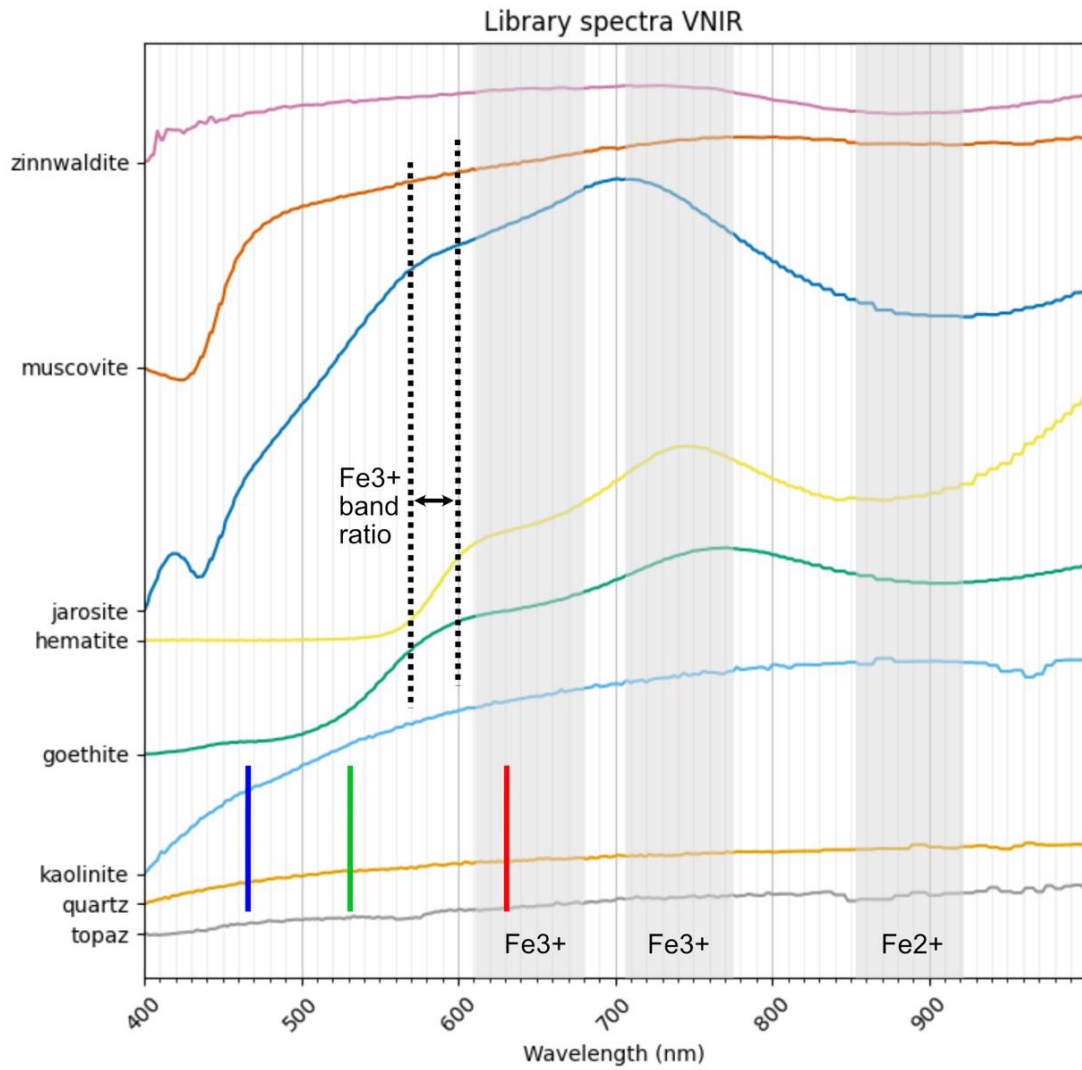


**Figure 1.2.** Spectral library of abundant minerals in Flöz 8. Mineral spectra from USGS Spectral Library v7 (Kokaly et al., 2017), zinnwaldite spectra (~25 pixel averaged) were obtained using the SisuRock hyperspectral scanning system with a sample from the Geoscientific Collection of TU Bergakademie Freiberg.

# 2 Equipment and Instruments

This chapter presents a background and configuration of equipment and instruments that form a functioning and versatile robotic platform which can perform data acquisition missions in an underground mining environment. The first two sections describe the Spot robotic platform on which the payload instruments are configured, followed by detailed sections of instrument background on hardware and operating software of the Cubert X20P and Velodyne VLP16 LiDAR. The final section describes the network and command structure to enable proper communication.

## 2.1 Boston Dynamics Spot

### 2.1.1 Hardware

The Boston Dynamics developed Spot is a versatile quadruped robot with a wide range of functionalities and mobility Spot is designed to navigate difficult terrain and perform user-created missions (Boston Dynamics, 2023e). Its robust design and size make Spot resilient to rough operating conditions such as narrow spaces, bad weather, high humidity, and extreme temperatures (Table 2.1). This makes Spot an excellent fit for underground mining environments. Spot can manoeuvre more easily compared to other wheeled platforms.

**Table 2.1.** Selection of Spot specifications (Boston Dynamics, 2023a).

|                         | <b>Boston Dynamics Spot</b> |
|-------------------------|-----------------------------|
| Dimensions              | 1000 x 500 x 191 mm         |
| Battery Capacity        | 564 Wh                      |
| Average Battery Runtime | 90 mins                     |
| Max Speed               | 1.6 m/s                     |
| Max Slope               | 30°                         |
| Operating Temp.         | -20°C to 45°C               |
| Max Payload mounting    | 14 kg                       |

Spot has 360-degree built-in stereo cameras that provide real-time imagery of its surroundings. The stereo cameras are located in the front and side of Spot's body frame, as shown in Figure A. Along with these cameras come built-in additional depth cameras that simultaneously generate depth data and maps. An anti-collision system uses this information to prevent Spot from colliding with objects and maintaining a good movement trajectory. The stereo cameras generate real-time RGB imagery of Spot surroundings, which can be viewed in real time. The native Spot software also visualises the generated heat maps but can only be extracted through the Robotic Operating System. Spot has two payload cable ports on its back for connecting custom payload applications.

Up to two payloads can be mounted on Spot using the rails on its back. The rails mounting points are adjustable and allow custom payload design. They are connected using two DB25 ports (Boston Dynamics, 2023a). These ports enable a Gigabit Ethernet and power connection to Spot's main body frame.

### 2.1.2 CORE Computer

The Spot CORE is Boston Dynamics' on-board computer that can be easily mounted as a payload on Spot. Up to two CORE computers can be mounted on Spot's back. A CORE computer is connected through a payload port to register on the LAN. This enables high-bandwidth connectivity and power. Contrary to the computer system inside Spot, the CORE is fully customisable and can be developed in either the Spot SDK or other software (Boston Dynamics, 2022). It runs an Ubuntu 18.04 (Bionic Beaver) distribution. However, it can be upgraded or changed to a different operating system and still connect to Spot. Before use, the payload COREs need to be registered in the Spot software. The payload must be registered to receive power and prevent Spot from touching the payload instruments during operation. Payloads can either be manually or automatically registered in the Admin Panel. A payload is registered with a (default) IPv4 address and adjacent network port on the Local Area Network created by Spot. The user's device can connect to the payload using a Soft-Shell connection (SSH) over its Wi-Fi access with the LAN (Boston Dynamics, 2023b). Once a connection with an Ubuntu 18.04 device is established, the payload can be configured using Cockpit software. Cockpit is a general robotics interface web UI that communicates with operating software while providing specific parameters and settings. It can also access multiple terminals on the CORE computer. Since Cockpit is only accessible in Ubuntu 18.04, changing the operating system will disable access to the Cockpit software. This means payload configuration and settings will no longer be accessible.

Boston Dynamics provides an operating platform with extensive user customisation for applications such as safety monitoring in industrial sites or reality capture (Lindqvist et al., 2022; Wetzels et al., 2022). Many of these applications use LiDAR technology for data capture and navigation, combined with a second or third payload that acquires a different data type.

### 2.1.3 Controlling Spot

All Spot software is configured in the Admin Panel. This panel User Interface (UI) can be accessed through the supplied tablet or by accessing a Google Chrome browser on Spot's IP address when a connection with the LAN is established. User settings, licensing, software updates, payload registration, and network settings can be configured in the panel. The Admin Panel does not contain any functions for robot operation. There are three different methods of controlling Spot:

1. The tablet software application runs on the supplied Samsung Galaxy Tab Active3 tablet. This application has a Graphical User Interface (GUI) and control joysticks for controlled locomotion. The joysticks make general manoeuvrability easier for the user than other controlling methods. All 360° stereo cameras can be visualised. The application can create and execute choreography files at any moment (Boston Dynamics, n.d.). However, accessing the mounted payloads for data acquisition is impossible, meaning the tablet software only allows for simple locomotion.
2. The Spot Robotic Operating System (ROS) driver developed by heuristics (heuristics, 2023) allows for simultaneous access to the mounted payloads and operating the Spot locomotion. The driver runs in a ROS1 noetic workspace on a Linux Ubuntu 20.04 operating device connected to Spot's LAN through Wi-Fi. The driver is accessed through multiple terminals and launches the Rviz GUI. This interface enables robot start-up and locomotive functions. Simultaneously, in other terminals, the payloads can then be accessed. All commands must be provided manually and do not contain automation functions or support.
3. The Spot Python Software Development Kit (SDK) (Boston Dynamics, 2023c) contains more functions for automating Spot operations. In the Python SDK, Spot is operated through multiple Command Line Interfaces (CLI) in a Python environment. Automated operations and

missions are more directly executed and customised in this environment but do not visualise real-time data in a graphical interface. This SDK can be run on either Windows or Linux systems, where the Spot ROS driver is Linux-exclusive.

## 2.2 Payload Configuration

Combining the Cubert X20P and VLP16 LiDAR payloads on the customisable Spot platform creates an Uncrewed Vehicle suitable for data acquisition in underground environments. Both instruments require an unobstructed field of view to maximise the data acquisition range. The Cubert X20P and VLP16 are connected with Spot through Boston Dynamics-developed CORE computers and are mounted on the back of Spot's body frame, which can be seen in Figure 2.1.

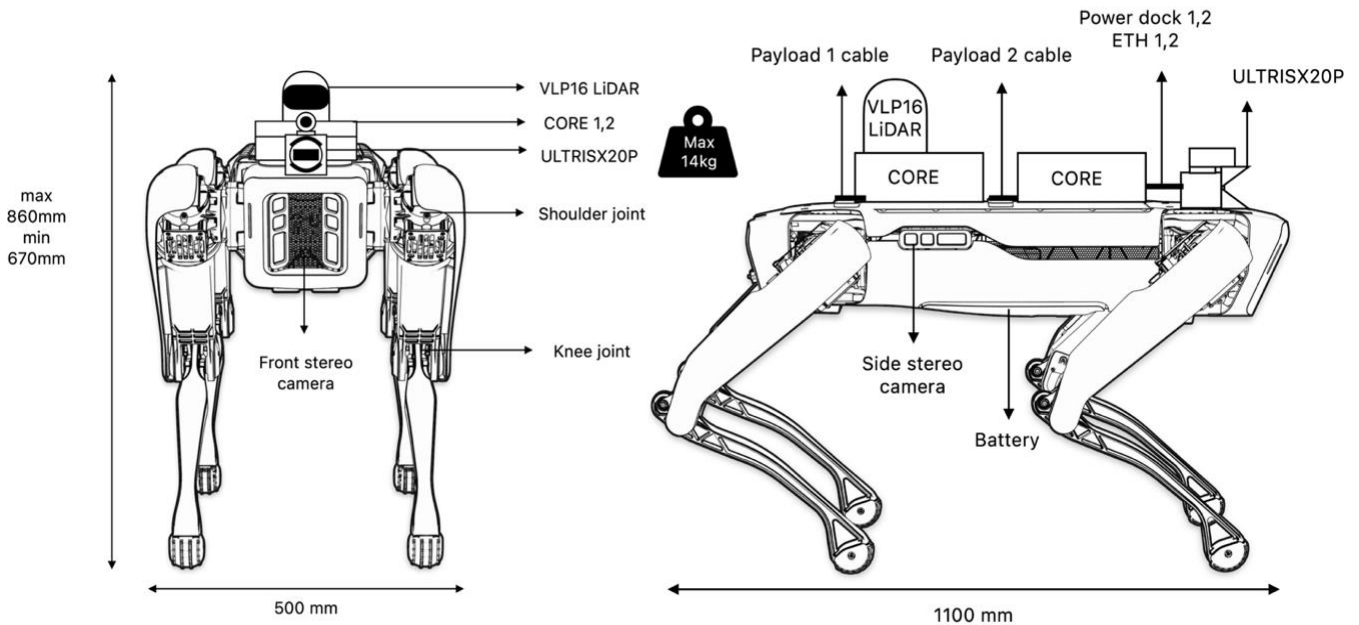


**Figure 2.1.** Schematic overview (front and side) of complete mechanical configuration, with Spot, VLP16 and Cubert X20P.

The VLP16 LiDAR scanner is mounted on Spot as part of the Enhanced Autonomy Payload (EAP) developed by Boston Dynamics to enhance Spot navigational abilities by adding LiDAR information to the existing stereo-camera anti-collisional system. Adding LiDAR data in the anti-collisional system increases Spot's viewing range by 100m (Boston Dynamics, 2023d). The EAP is supplied with a mount and protective roll cage for the VLP16 LiDAR. It is in an elevated position relative to the Spot mainframe and the Cubert X20P to maximise the laser field of view and range (Boston Dynamics, 2023d). The connecting cable outside of Spot's main frame should not obstruct the LiDAR or Spot camera view.

The Cubert X20P is mounted on the front of Spot to maximise camera FOV and simplify focus during operation. In contrast to the VLP16, the Cubert X20P does not have a mount for Spot; thus, a custom mount was designed, as shown in Figure 2.2. The mount is designed using Onshape Computer-Aided Design (CAD) web software for designing 3D objects and printed using the MakerBot method X FDM 3D printer. The custom mount attaches to 4 screw holes on the front of Spot, as seen in Figure 2.2. The camera is then screwed onto the mount using four smaller hex screws. The mount is designed to be rigid and robust to prevent the camera from moving. The Cubert X20P is mounted facing forward, parallel to the front stereo camera of Spot. Misaligning the camera on the mount might result in unexpected skewed images. Therefore, a small margin of 1 mm is left between the mount and the camera. This margin allows

for adjusting the camera's position relative to Spot's longitudinal axis. It is not possible nor desired to rotate the camera with this mount.

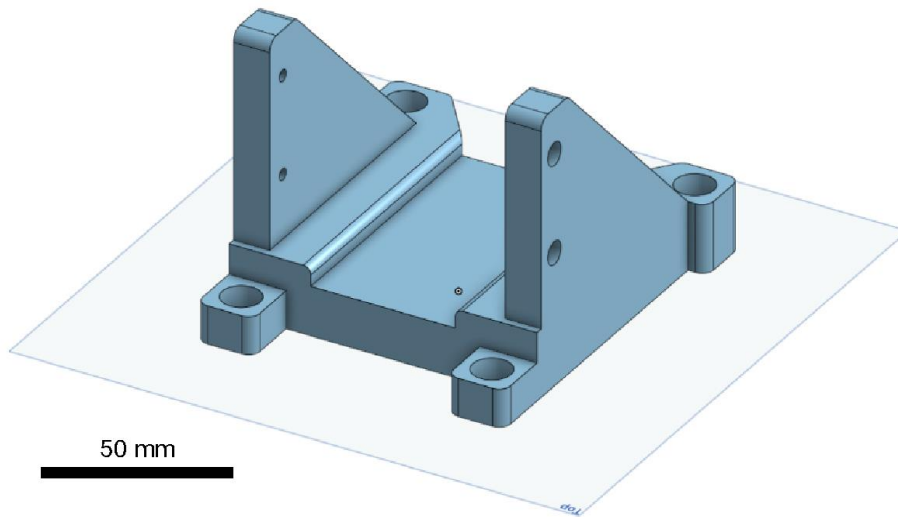


**Figure 2.2.** 3D mount design for the Cubert X20P on Spot.

The Cubert X20P hyperspectral camera is connected to the CORE computer through a combined power cable for the spectral and panchromatic camera. Network communication with the CORE computer is accomplished through two category 7 Ethernet cables (Figure 2.1). The many cables are bundled and moved away from the VLP16 LiDAR's point of view as much as possible. The final mechanical configuration is shown in Figure 2.3.



**Figure 2.3.** Side view of Spot with two CORE computers, Cubert X20P hyperspectral camera and VLP16 LiDAR fully mounted.

## 2.3 Cubert ULTRISX20P

### 2.3.1 Hardware

The Cubert ULTRIS X20 PLUS is a dual-sensor hyperspectral camera developed by Cubert GmbH. It was originally designed to be mounted on an Uncrewed Aerial Vehicle (UAV) but can also be used for Uncrewed Vehicles (UV) on the ground. The Cubert X20P hyperspectral camera consists of a spectral camera (CMOS) and a panchromatic camera mounted on its top, which can be seen in Figure D. Both the spectral and panchromatic cameras operate in the VNIR spectral range. The panchromatic information is used to perform pansharpening and enhance the spatial resolution of the image (Cubert GmbH, 2023e). Its small size and low weight (Table Y) make the camera suitable for mobile operations. A robust and weather-resistant casing makes it ideal for operation in underground or outside conditions.

**Table 2.1.** Selection Cubert X20P specifications (Cubert GmbH, 2023d).

|                     | <b>Cubert ULTRISX20P</b> |
|---------------------|--------------------------|
| Weight              | 630 g                    |
| Dimensions          | 86 x 121 x 105 mm        |
| Spatial Resolution  | 410 x 410 pixels         |
| Wavelength Range    | 350 – 1000 nm            |
| Spectral Bands      | 164                      |
| Spectral Sampling   | 4 nm                     |
| FOV (Field of View) | 35 °                     |
| Max Frame Rate      | 4 Hz                     |
| Data Link           | GigE (2x)                |

The CMOS spectral camera performs a single exposure (global shutter) image capture, capturing all spectral bands simultaneously. The camera lens can be seen in Figure D. Each small reflective circle in the camera lens is a suboptic. These suboptics generate their own image channels with a unique spectral response. All suboptics are geometrically offset and view the target at a slightly different angle. This is corrected by default for a distance to target of about 6 m to infinity. When taking pictures from a shorter distance, a custom distance calibration is needed (Cubert GmbH, 2023b). The panchromatic sensor is also physically offset from the CMOS spectral camera and is aligned by the hardware- and software by default for 6 m. When taking images closer than 6 m, an additional distance calibration must be performed to determine the image offset between the panchromatic and hyperspectral camera. The exposure time can be adjusted in the settings or through an auto-exposure function. Moving the Spot body frame during exposure will result in a blurry image.



**Figure 2.4.** Cubert X20P spectral camera suboptic lens (below) and panchromatic lens (top).

### 2.3.2 CUVIS SDK

The Cubert X20P is operated through the CUVIS Software Development Kit. This SDK allows customising the executing code and developing automated image capture and processing commands. Using the SDK maximises control of data acquisition and data workflow design. The SDK comes with precompiled example executables for image capture, processing and export. The exposure time is not determined automatically but is defined in the SDK image capture executables. An elaborate manual on using the CUVIS SDK can be found in Appendix D. The software performs a dark subtract, white reference correction and export to ENVI format (Cubert GmbH, 2023a). The CUVIS SDK runs on Ubuntu 20.04 distribution systems, while the Spot CORE runs on Ubuntu 18.04. Therefore to execute the CUVIS SDK software, the CORE ubuntu distribution must be upgraded. Upgrading to Ubuntu 20.04 disables the ability to access the CORE Cockpit software, which runs on Ubuntu 18.04. Therefore, changing payload settings, such as adjusting the IPv4 address, is done before upgrading the Ubuntu distribution on the Spot CORE.

## 2.4 Velodyne VLP16

### 2.4.1 Hardware

The VLP-16 by Velodyne LiDAR is a small and rugged 3D reflectance puck laser scanner designed for uncrewed vehicle operations (Velodyne LiDAR, 2015). Its puck-like shape and weather-resistant housing, in combination with no visible or exposed rotating parts, make it suitable for underground environments. Originally designed to complement navigation and collision avoidance software, multiple applications have shown that the VLP16 can be consistently used for reality capture, making it a multifunctional instrument (Andrew Lassiter et al., 2020; Glennie et al., 2016). On Boston Dynamics uncrewed vehicle Spot, the VLP16 is integrated as the Enhanced Autonomy Payload (EAP) (Boston Dynamics, 2023d). As part of the EAP, the VLP16 was originally designed to enhance Spot's navigation and autonomy by combining LiDAR with Spot's built-in stereo and depth cameras. This increases the sensing range from 4 to 100 m. It enhances robot autonomy and allows for the creation of more extensive 3D maps.

**Table 2.3.** Selection of Velodyne VLP16 specifications (Velodyne LiDAR, 2019), configured in the Spot EAP.

|   | Velodyne VLP-16 LiDAR  |
|---|------------------------|
| Weight                                      | 3.6 kg                 |
| Dimensions                                  | 300 x 190 x 162 mm     |
| Sensor                                      | 16 Channels (IR)       |
|   | 903 nm                 |
| Measurement Range                           | 100 m                  |
| Field of View<br>(vertical/horizontal)      | +15° to -15°<br>/ 360° |
| Angular Resolution<br>(vertical/horizontal) | 2.0°<br>/ 0.1° - 0.4°  |
| Rotation Rate                               | 5 Hz – 20 Hz           |
| Operating Temp.                             | -40°C to 60°C          |

The VLP16 has 16 fixed-angle IR lasers (Table 2.3). Each laser has its ID and is paired with a detector to measure the distance to a target. The array of 16 laser spins in the puck housing fires at least 18,000 times per second, resulting in 300,000 data points per second. When a laser emits a pulse, the time of shooting and direction are registered. The emission will travel until it hits a target and then reflect. That energy is received by the paired detector, and the time-of-acquisition is registered. The principle of combining time-of-shooting and acquisition is called Time of Flight (ToF) (Velodyne LiDAR, 2019). Since the 16 lasers are all at a fixed angle and continuously rotate, the data is collected in 16 parallel lines (Figure 2.5). The density of points along the data lines generated by one laser depends on the total data capture time. The longer the data capture, the more data points form along the line. Image A in Figure X had less capture time than image B, clearly showing a denser laser data line.

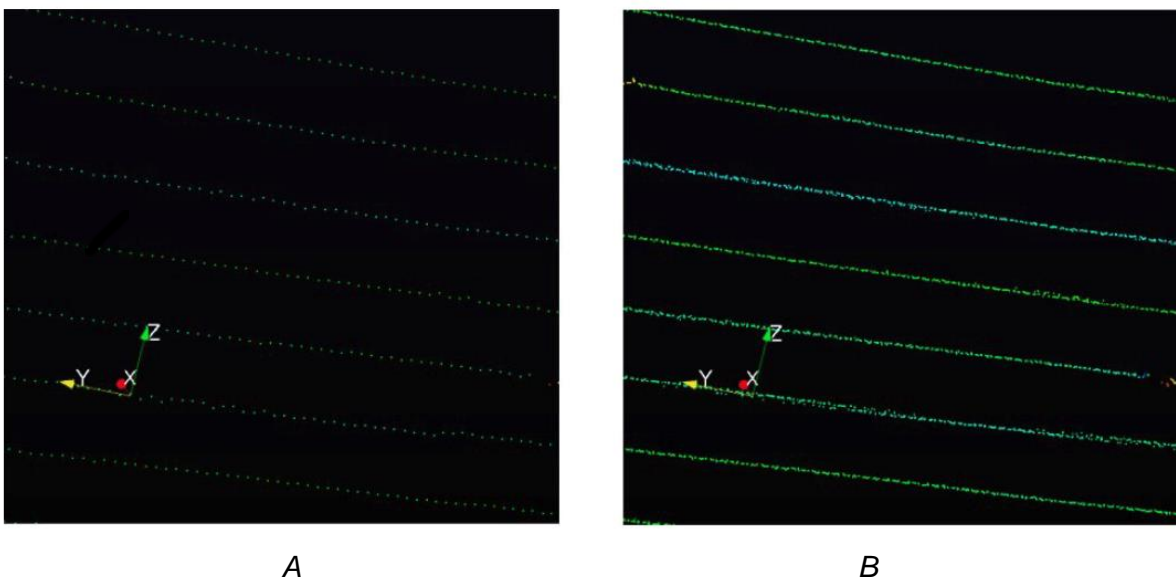


**Figure 2.5.** Point density example, copied from VLP16 User Manual (Velodyne LiDAR, 2019).

The distance between parallel lines is determined by the distance to the target and is described in Equation 1.

$$Gap = distance\ to\ target \times \tan(\text{vertical angle between scan lines}) \quad (1)$$

Since the lasers are positioned at a fixed angle, the closer the distance to the target, the smaller the distance between vertical lines. Logically, this will decrease the target surface's total data footprint (Velodyne LiDAR, 2019).

### 2.4.2 Velodyne Driver

Since the VLP16 is configured as the EAP on Spot, the software is installed and accessed on the CORE computer. The CORE computer runs an Ubuntu distribution to successfully build and run the Velodyne Driver ROS package and driver (Velodyne LiDAR, 2023). This means a complete ROS melodic or noetic must also be installed on the CORE device. The driver can then generate live point cloud data from Spot's current position through network interface data capture. This copies all transported data over the network interface with which Spot and the VLP16 LiDAR are connected.

## 2.5 Network and Command Configuration

To communicate with all instruments, it is necessary to have a non-conflicting network architecture. The command PC is remotely connected to Spot's unique IP address (static) (Boston Dynamics, 2023b). It can execute the Spot operating software and enables multiple SSH connections to each CORE computer. However, by default, both CORE computers are registered on the same IP address: 192.168.6.5 (Boston Dynamics, 2023b, 2023c). When connecting to this IP, both CORE computers will attempt a connection, and the SSH fails. This is solved by adjusting the front CORE computer's priority IP address (in Cockpit). This IP is then accessed through a different network port as seen in Figure 2.6. The command PC can now simultaneously connect to both CORE computers without conflicting IP structures. Appendix E provides instructions on navigating and connecting to the network architecture.

Each instrument has a default IP address on which it communicates over the Ethernet cables with its connected CORE computer. For the Cubert X20P, the spectral and panchromatic camera each have a unique IPv4 address, which is statically defined on the CORE network interface ports, so that after reboot, the CORE computer is automatically connected to the correct IPv4 address. These network interface ports are defined as 'enp1' and 'enx' for the hyperspectral- and panchromatic camera, respectively. The VLP16 LiDAR is connected through a single Ethernet connection. The EAP configuration, by default, has the correct static IP settings to connect to the VLP16 LiDAR automatically.

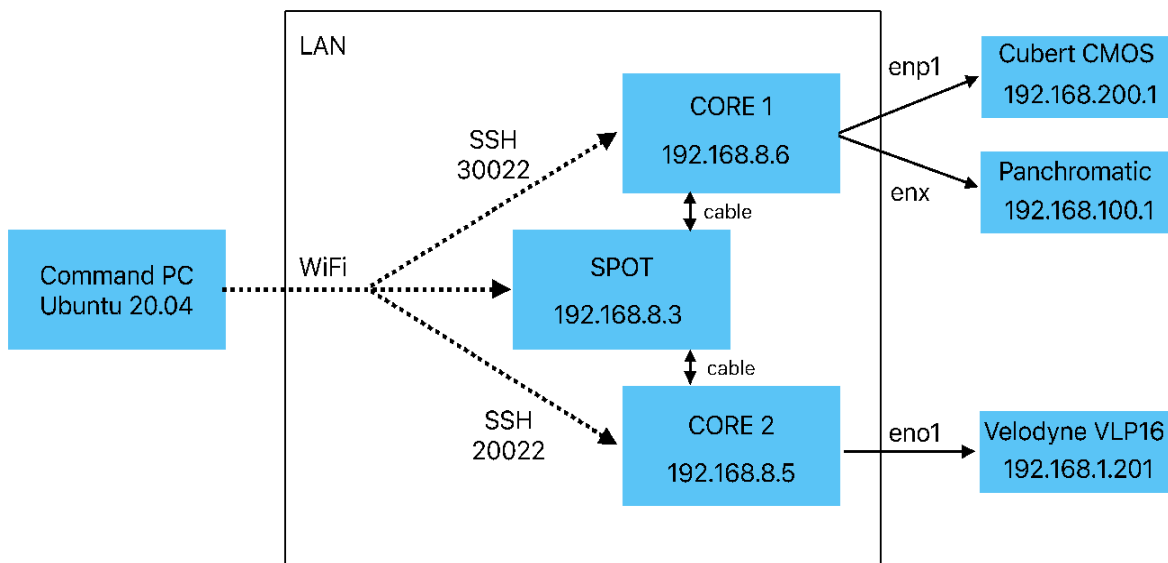


Figure 2.6. Command PC and network configuration.

# 3 Methods

## 3.1 General Workflow

To create interpretable geological products, spectral and geometric data are processed and combined into 3D 'hyperclouds' (Thiele et al., 2021). Hyperclouds are a combination of hyperspectral and 3D geometric information. The hyperspectral pixels containing spectral information are projected on the point cloud to form a hypercloud. This is done in a Python toolbox developed by HiF called *hylite* (Thiele et al., 2021). Each point in the 3D hypercloud has a spectral attribute, creating a 3D hyperspectral map of a rock surface.

The complete workflow of creating hyperclouds with the configured multi-sensor robotic platform consists of multiple processing steps, shown in Figure 3.1. The raw hyperspectral and geometric LiDAR data undergo several pre-processing steps before being combined into a hypercloud. The 3D pointcloud forms the basis for hypercloud projection. After the hypercloud projection, an RGB hypercloud can be visualised directly, or several spectral analysing techniques are performed on the hypercloud. This chapter describes the processing and creation of hyperclouds using the proposed workflow, followed by sections on applying the proposed workflow in a lab and underground setting.

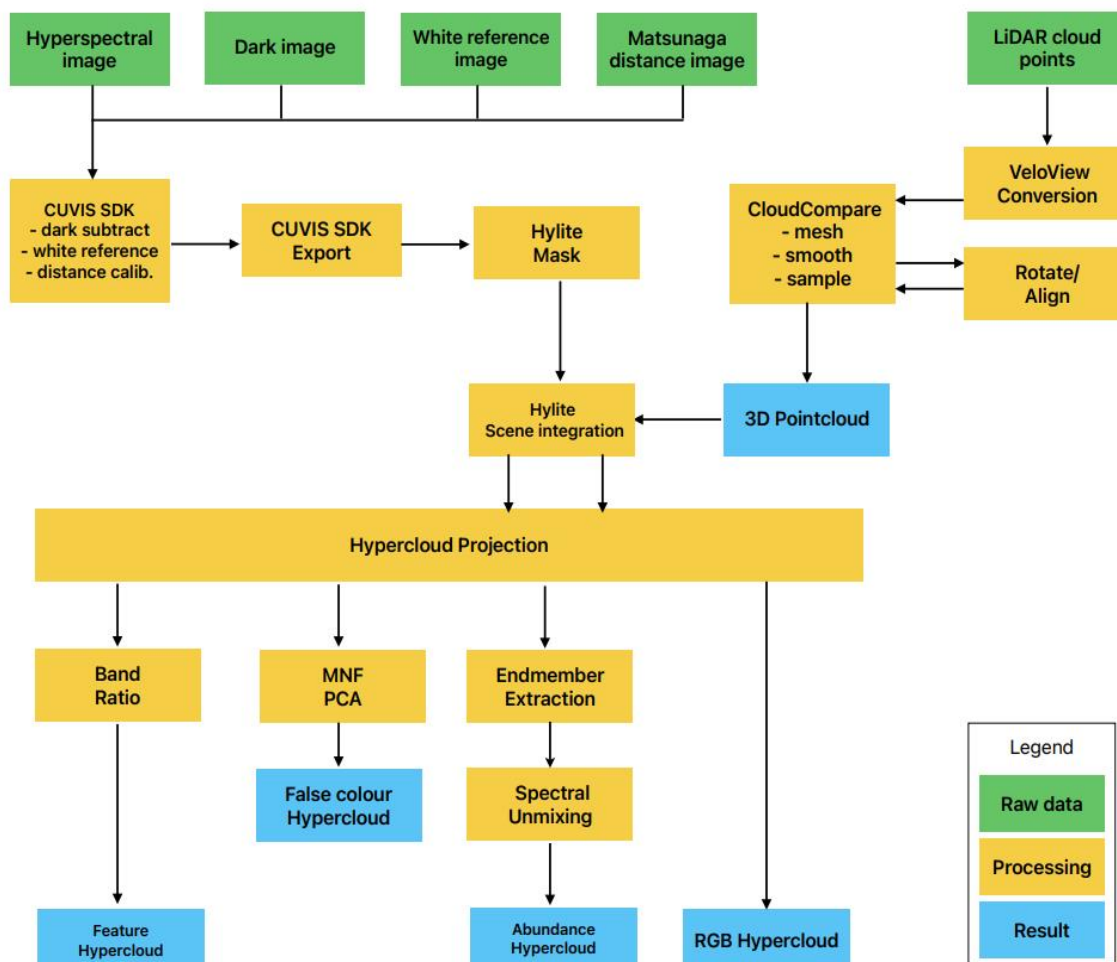


Figure 3.1. General data workflow for hypercloud creation.

## 3.2 Hyperspectral Data

Using the Spot ROS driver, the mobile robotic platform is positioned in front of the rock face so the Cubert X20P has the outcrop target in frame. There is currently no method of visualising and validating the camera's frame in real-time on the command device. Therefore, the distance to the target and viewing angle must be manually evaluated using the camera Field of View (FOV) as highlighted in Cubert X20P specifications in section 2.3.1 (Cubert GmbH, 2023d). To evaluate the camera frame and overlap between images, equation 2 is used. The frame dimensions on the target surface are determined by calculating the frame width using the distance to the target surface and the Field of View (35 degrees).

$$\text{Frame width} = \text{distance to target surface} \times \tan(17.5) \times 2 \quad (2)$$

When Spot and the hyperspectral camera are in position, hyperspectral data can be acquired. Each hyperspectral data file is captured in a hypercube shape. This means each data point has an x and y pixel coordinate in the image frame and unique spectral attributes, forming a spectral data cube. Besides taking a normal hyperspectral light hypercube of the target, an additional dark hypercube, a white reference hypercube and a hypercube with the Matsunaga board in the frame are needed. The sections below describe the method for acquiring each hypercube and the information on how it is used for correcting the hypercube data in the CUVIS SDK processing software. The hyperspectral data is captured by running an executable on the CORE payload computer connected to the hyperspectral camera (Appendix D). In this executable, the image capture exposure time is also defined. This should be adjusted accordingly depending on the current illuminating conditions. Each captured hypercube is formatted as a Cubert-native .cu3 file.

### Dark hypercube subtract

A dark hypercube is captured with the hyperspectral camera- and the panchromatic lens cap on. The dark hypercube (*DARK*) should be taken with the same exposure time as the light data. The dark hypercube is then subtracted from the raw light hypercube ( $I_{RAW}$ ), creating the dark subtracted hypercube ( $I_{DS}$ ) as shown in equation 3. Subtracting the dark noise offsets from the hyperspectral data will reduce noise in the final spectra (ElMasry & Sun, 2010).

$$I_{DS} = I_{RAW} - DARK \quad (3)$$

### White reference division

Each light source has its spectral properties, which must be accounted for in data processing. To best capture the pure spectra of the illuminating conditions, a hypercube is captured with a white (spectrally homogenous) reference panel covering the whole hypercube frame. Equation 4 shows the processing of the white reference hypercube to produce a spectral reflectance hypercube. The white hypercube (*WHITE*) also requires a dark hypercube (*DARK*) subtraction to account for dark noise offset. Dividing the dark subtracted hypercube from equation 3 ( $I_{DS}$ ) with the white reference hypercube creates a corrected reflectance hypercube ( $I_{REF}$ ) (Cubert GmbH, 2023b; ElMasry & Sun, 2010).

$$I_{REF} = \frac{I_{DS}}{WHITE - DARK} \quad (4)$$

### Distance calibration

Since the panchromatic camera is mounted on top of the CMOS camera (*H* in Figure 3.2), the panchromatic camera sees the target at an offset angle, as indicated by *a* Figure 3.2. This angled offset is accounted for in the default Cubert X20P distance calibration to operate for a distance to target range of 6 to 6.5 m.

Capturing a hypercube from a shorter distance with the default distance calibration will result in an offset ( $h$  in Figure 3.2) between the panchromatic- and CMOS hypercube (Cubert GmbH, 2023b). This results in the panchromatic hypercube being offset, as indicated in grey in Figure 3.2.

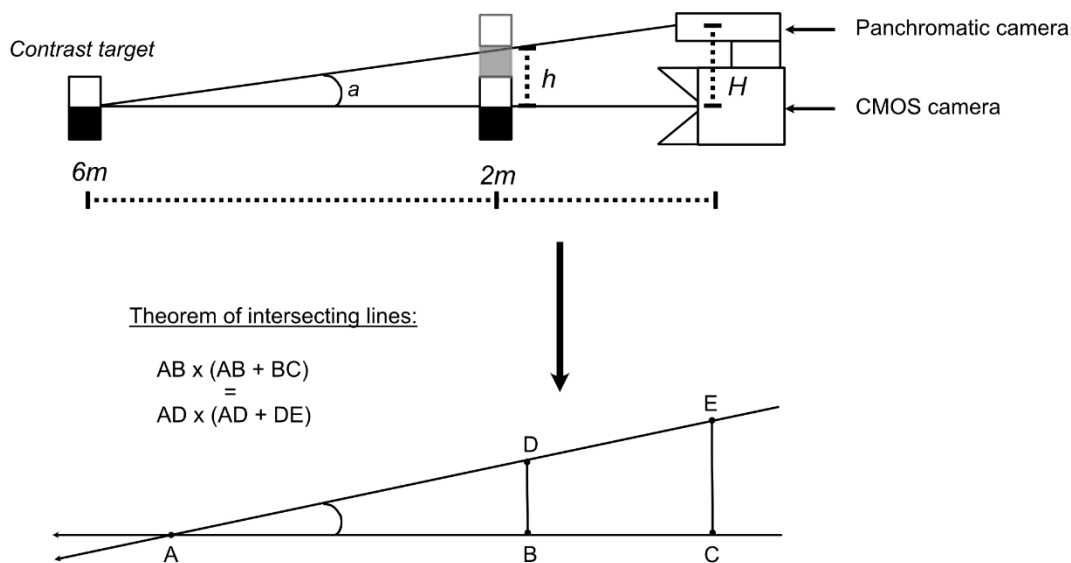


**Figure 3.2.** Distance calibration problem and solvable schematic view with theorem of intersecting lines.

The CUVIS SDK software performs a new distance calibration by using the theorem of intersecting lines. By providing a high-contrast target in the camera frame at the same distance as the rock surface, the software can correlate pixels in both the panchromatic and CMOS hypercube. Using the theorem of intersecting lines, as shown in Figure 3.2, the software can calculate the offset  $h$  and move the panchromatic down the same distance to align with the CMOS hypercube (Cubert GmbH, 2023c). For this workflow, the Cubert-supplied Matsunaga high-contrast panel is used. The Matsunaga high contrast panel has an irregular checkerboard-like pattern and is solely designed for custom distance calibration purposes.

### CUVIS SDK processing

The complete dark subtract, white reference and distance calibration are performed by executing the CUVIS SDK processing software. The software outputs the resulting corrected reflectance hypercube in the Cubert-native .cu3 format.

### Export

To visualise and use the processed hypercube in *hylite*, the hypercube is exported into the ENVI format using CUVIS SDK export functionalities as described in Appendix D. This ENVI format contains a .hdr and binary file, which can be used in the *hylite* toolbox for hypercloud projection.

### Analysis with *hylite*

Several spectral analysing techniques are performed on the hyperclouds, noted in Tables 3.1 and 3.2. This section describes the working principles and results of each analysing technique.

A spectral band ratio is calculated by dividing a common feature spectral maximum referred to as 'shoulder' by its minimum, or 'trench'. This is done for each unique pixel and adjacent spectra, resulting in a spectral ratio for individual pixels. Consequently, a high band ratio indicates a deeper spectral absorption in that pixel (Clark, 1999; van Ruitenbeek et al., 2006). Based on the expected mineralogy described in section 1.5.3, the ferric iron ( $Fe^{3+}$ ) is used for band ratio analysis. This feature ratio is calculated by dividing

600 and 570 nm spectral wavelengths. An iron band ratio map then shows the rock surface's relative intensity of ferric iron in minerals (Andrew Lassiter et al., 2020; Bula et al., 2020).

The Minimum Noise Fraction (MNF) analysis is a dimensionality reduction technique based on the signal-to-noise ratio of the data (ElMasry & Sun, 2010). Mapping the signal-to-noise ratio gives information about the amount of noise and heterogeneity of the data. MNF outputs a user-defined number of bands, each having a unique signal-to-noise ratio. The first band contains the most signal relative to noise. The following bands will have a gradual decrease in signal-to-noise ratio. Each band is evaluated for geological information and amount of noise. The bands showing most geological information and least noise are combined into a false colour map.

Principal component Analysis (PCA) is done to visualise the internal hypercube data heterogeneity and variance. The PCA function transforms the originally correlated variables into uncorrelated variables or principal components. These are then ordered in terms of importance and contribution to the total variance of the dataset. The PCA method's first component shows the most variance in the hypercube data. Combining the principal components with most geological information into a false colour map shows the heterogeneity of the dataset.

**Table 3.1.** Feature extraction and visualising techniques for hyperspectral data.

| <b>Technique</b>                          | <b>Description</b>  | <b>Result</b>                                     |
|---|---|---|
| <i>Band ratio</i>                         | Dividing the maximum and minimum of specific spectral features.   | Relative intensity of spectral feature.           |
| <i>Minimum Noise Fraction (MNF)</i>       | Compute the normalised linear combinations of original bands to maximise signal-to-noise ratio.                     | Signal-to-noise ratio maps and false colour maps. |
| <i>Principal Component Analysis (PCA)</i> | Compute the mutually orthogonal normalised linear combinations of the vector of observations with maximum variance. | Principal component maps and false colour maps.   |

After creating RGB composite false colour maps using MNF and PCA, the geological information in the hypercube can be assessed. An endmember extraction is done to distinguish between the geological information, as noted in Table 3.1. Through assessment of the geological information from MNF and PCA false colour maps, the amount of data endmembers is estimated, which is necessary as an input parameter in endmember extraction functions. Performing an automated endmember extraction ensures an unbiased analysis of the complete dataset.

Endmember extraction analyses the data set to group reflectance information into idealised spectral signature classes. This method is often called 'pure pixel extraction' because it aims to create pure spectral signatures (Kale et al., 2019). The number of endmembers is defined in the analysis, which, in our case, is based on the MNF and PCA analysis. Endmember extraction is done through an extraction algorithm called NFINDR. The algorithm plots the principal components of the hypercube data in terms of variance and finds the maximum distance between data points, creating endmembers.

Spectral unmixing is done through a supervised, Fully Constrained Least-Squares (FCLS) function. FCLS is used since we define the number of endmembers extracted from the hypercube data. The FCLS function is based on the Non-Negative Least Squares (NNLS) and Sum-to-one Constrained Least-Squares (SCLS) algorithms. Together, it assumes the total reflectance of a pixel to be a combination of all endmember signals (Michelsburg & Puente Lé, 2018). For each pixel, the highest endmember coefficient is determined, in which the pixel is classified. This creates a detailed map of the endmember distribution on the rock surface, expressed as the abundance of the endmember spectral class relative to the total spectral data and information.

**Table 3.2.** Analysing techniques for hyperspectral data.

| <b>Technique</b>                      | <b>Description</b>  | <b>Result</b>                                 |
|---------------------------------------|---|---|
| <i>Endmember extraction</i>           | Extracting idealised, pure pixel spectral classes (NFINDR).   | Identified endmembers with signature spectra. |
| <i>Spectral unmixing (supervised)</i> | Fully Constrained Least-Squares (FCLS) unmixing using Non-Negative Least Squares (NNLS) and Sum-to-one Constrained Least-Squares (SCLS) algorithms. | Abundance maps (endmembers).                  |

### 3.3 LiDAR Data

When Spot is turned on, the Velodyne VLP16 automatically powers up and starts spinning its fixed lasers. Initially, the generated data is only used for Spot navigation as part of the Enhanced Autonomy Payload (EAP). Therefore, the generated point cloud is directly copied from the network interface connection and not through a User Interface (UI), as demonstrated in Appendix E. The VLP16 LiDAR data acquisition is performed in the exact locations of the hyperspectral data acquisition. To prevent occlusion caused by Spot's main body frame and the Cubert X20P, we have Spot turn around 180° degrees relative to its original position and face away from the rock surface so that the VLP16 has an unobstructed view. The gap between generated data lines depends on the distance to the rock surface or target, as described in section 2.4.1. Reality capture studies using the VLP16 have shown that changing the viewing angle for multiple data acquisitions can effectively increase data density (Andrew Lassiter et al., 2020; Bula et al., 2020). Therefore, to increase the data density of the generated pointcloud, the data is captured from multiple angles (5, 10, 15 and 20 degrees) relative to the horizontal plane. Having Spot's body frame pitch in several specified angles and combining the generated clouds increases point density. The body pose and pitch can be adjusted in the RVIZ panel. Each body pose, with known specified angles, will have its own point cloud capture file. The data point of origin also rotates because the VLP16 rotates with the Spot body frame. Each data file must then be rotated back into Spot's neutral position using tools in Cloud Compare software or a Python script. A complete guide on acquiring pointcloud data from the VLP16 on Spot is included in Appendix E. The time the VLP16 captures pointcloud data is set to 60 seconds. Capturing data for a more extended period automatically creates multiple data files and does not increase point density, as described in section 2.4.1. The acquired data is saved on the CORE payload computer as a .pcap network capture file.

#### Veloview

To visualise the generated pointcloud, the data is imported into VeloView software. This pointcloud viewer is developed by Velodyne LiDAR and has multiple functionalities, including pointcloud visualisation and export (Velodyne LiDAR, 2021). VeloView is a first check to check data quality before exporting to CSV format and CloudCompare. VeloView is run on the command device with Ubuntu 20.04 to simplify data workflow.

#### CloudCompare

After exporting the pointcloud data to CSV format, it can be imported into CloudCompare (CloudCompare, 2023). Each pointcloud with a specific pitch angle is aligned using the align tool. The merge tool then combines all pointclouds into a single pointcloud. This pointcloud is segmented into an area of interest with the segment tool. The point cloud is transformed into a mesh using triangular interpolation to fill the data

line gaps. However, this tool will make a very rough surface representation of the rock surface; thus, a Laplacian smoothing tool is used. A relatively low smoothing factor is chosen to reduce curtaining effects and preserve the rock geometry. Lastly, mesh sampling converts the smoothed mesh back to a point cloud. This results in a dense pointcloud of the rock surface or target geometry, which can be used for projecting hyperspectral data on.

### 3.4 Hypercloud Projection

The hypercloud projection is performed in a Python environment using the *hylite* toolbox. Each analysing technique (Tables 3.1 and 3.2) can then be used on the hypercloud. The main principle of hypercloud creation relies on matching hypercube pixels to points in the pointcloud in the same 'true' location. This can either be done manually or automatically. The automatic matching is based on an additional intensity or RGB reflectance data in the pointcloud. Since we only acquire geometric information, the manual matching method is used. A virtual camera must be defined to merge the hyperspectral and pointcloud data correctly. The virtual camera view will specify the direction in which the hyperspectral data is projected onto the pointcloud. Ideally, the virtual camera has the same image frame as when the hyperspectral data was acquired with the Cubert X20P. After correctly matching, the hyperspectral data is pushed onto the pointcloud and merged with the pointcloud data, forming a hypercloud.

After creating multiple hyperclouds from the same rock surface, they are merged into a single large hypercloud. All hyperclouds require overlapping areas to prevent gaps in the resulting hypercloud.

### 3.5 Application of Proposed Workflow

The proposed method is applied to a lab- and underground environment. Testing the method in a lab environment allows all functionalities and their reliability to be assessed before taking the robotic platform into the field. The rocks used in the lab tests originate from the Zinnwald/Cinnovec visitor mine. Therefore, the lab test can be a reference for the underground test conducted in the outcrop of the Zinnwald/Cinnovec mine; the lab and underground data acquisition setups are explained in section 3.5.2. and 3.5.3 respectively.

#### 3.5.1 Exposure Time Study

Hyperspectral data is acquired at 100 ms, 200 ms and 400 ms exposure time for both the lab and underground application. As described in section 2.3.2, the ideal exposure time is not automatically adjusted. By comparing the quality of exposure times, an optimal exposure time is derived for each application. The dataset taken at the optimal exposure time is then used for further processing and analysis, described in section 3.2.

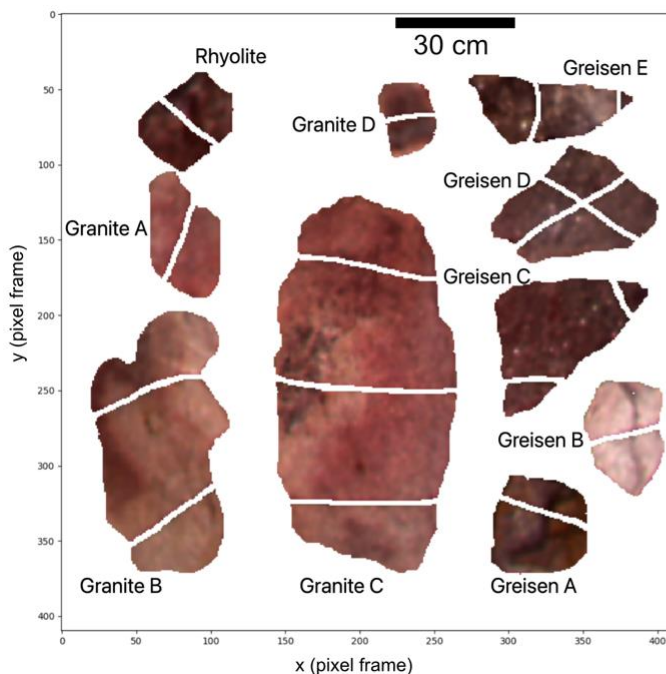
#### 3.5.2 Lab Application

The lab test is conducted at HIF in Freiberg, Germany. The rock samples are fixed on three wooden boards using iron straps and put up against the wall, as seen in Figure 3.3. Each wooden board is 380 mm in width and 1040 mm in length. The wooden boards and rocks are illuminated by two 500 W halogen floodlights on opposite sides facing the target. Spot is moved between the lights facing the rocks to acquire the sequence of hyperspectral images described in section 3.2. Afterwards, Spot rotates to acquire the LiDAR data described in section 3.3. To simulate underground conditions, the windows are blocked with panels to prevent sunlight from entering the experiment area.



**Figure 3.3.** Lab test setup showing the rock samples on three wooden boards, Spot, and light setup behind Spot on either side.

After hyperspectral data pre-processing using the CUVIS SDK, the data is loaded into *hylite*. The hyperspectral data is masked to remove the wooden board and wall backgrounds. (Figure 3.4). Each rock sample has a unique ID and is picked to represent the geological setting and lithological diversity of the outcrops in the Zinnwald/Cinnovec mine. Rock ID and characteristics are modified from Kirsch et al. (2023).



| Rock ID   | Characteristics                         |
|-----------|---|
| Granite A | Albite granite with hematite-alteration |
| Granite B | Sericite-alteration                     |
| Rhyolite  | Rhyolite                                |
| Granite C | Sericite-alteration                     |
| Granite D | Kaolinite-alteration                    |
| Greisen A | Quartz greisen                          |
| Greisen B | Kaolinite-rich greisen                  |
| Greisen C | Hematite-rich greisen                   |
| Greisen D | Quartz-mica greisen                     |
| Greisen E | Quartz-zinnwaldite-topaz greisen        |

**Figure 3.4.** Masked RGB image of rock samples with corresponding Rock ID and table with adjacent lithological characteristics, modified from Kirsch et al. (2023a).

### 3.5.3 Underground Application

The underground data acquisition and test of the proposed workflow is conducted at the Zinnwald/Cinnovec visitor mine. By acquiring data from a rock surface in an underground environment, the method is applied to a case study. The conditions in the mine resemble older underground mines with narrow and irregular passages. Spot acquires data from two rock surfaces along Floz 8 named UG-1 and UG-2.

At UG-1, hyperspectral data is acquired from two positions parallel to the rock surface at a distance of 2m. The hyperspectral data is acquired from 4 different vertical pitch angles of Spot: neutral, 7, 14 and 21 degrees. This results in an overlapping vertically extended image of the rock surface. Spot is then moved 50cm to the left into the second position facing the same rock surface, where angled acquisition is repeated. Combining the two positions at UG-1 results in a square data frame, as shown in Figure 6. After hyperspectral data acquisition, Spot turns 180 degrees to face away from the rock surface and executes the LiDAR acquisition sequence described in section 3.3. A photogrammetry cloud of the UG-1 rock surface is also created using a Nikon D850 35mm camera.

The acquisition method at UG-2 differs from UG-1 and does not involve vertical tilting of Spot and acquisition from two positions. At UG-2, Spot acquires data from the same position at a 4m distance but from three different horizontal angles by doing a body twist. Like UG-1, these separate frames are converted into hyperclouds and merged into one larger hypercloud to represent the complete UG-2 frame. This results in a rectangle data frame, as seen in Figure 3.6. After hyperspectral data acquisition, Spot turns around to execute the LiDAR acquisition sequence as described in section 3.3.

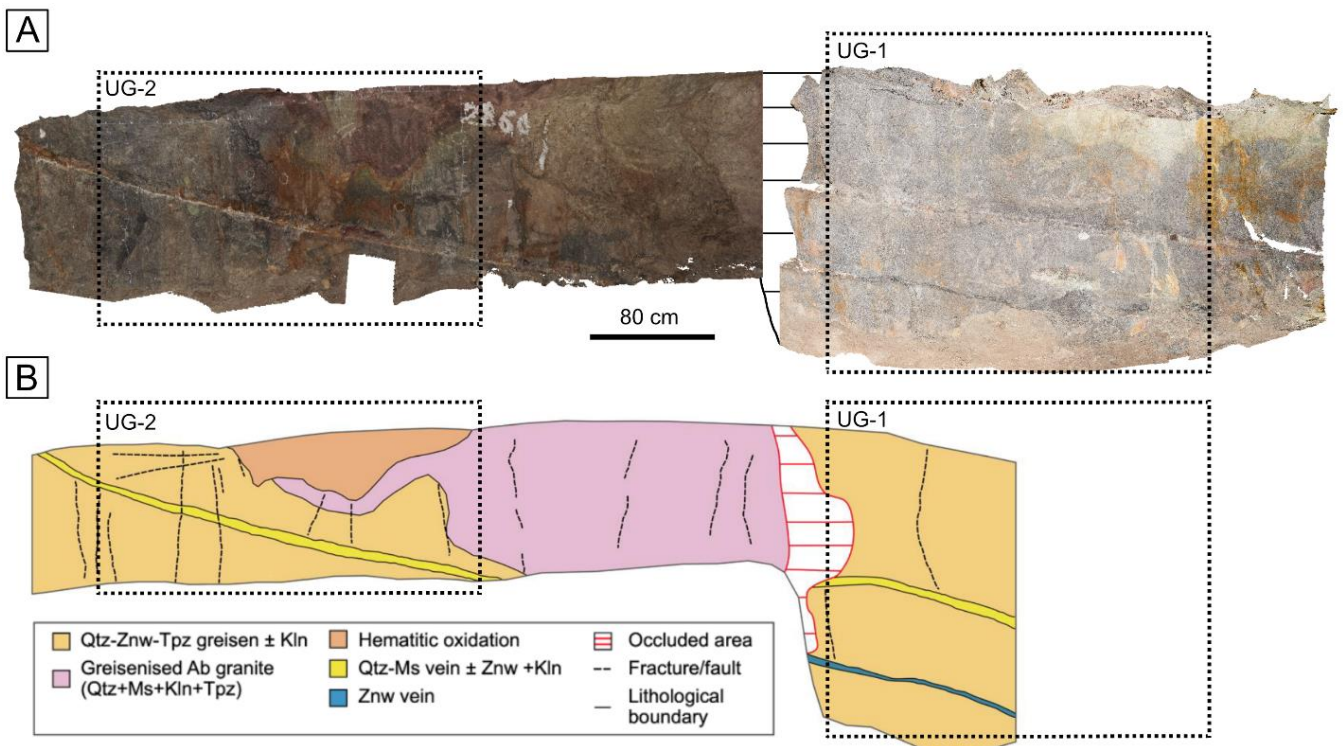


**Figure 3.5.** (A) RGB photogrammetry hyperclouds of rock surface UG-1 and UG-2 data frames indicated by dotted lines. UG-2 photogrammetry hypercloud obtained from (Kirsch et al., 2023c). (B) Field sketch rock surface UG-1 and UG-2 data frames indicated by dotted lines. Original sketch modified from Kirsch et al. (2023a). Mineral abbreviations from Whitney & Evans (2010).

For UG-1 and UG-2 data acquisitions, three halogen 500W floodlights are placed behind Spot to illuminate the rock surface, as shown in Figure 3.6. The lights are angled to not cast a shadow from the Spot body frame and evenly illuminate the rock surface.



**Figure 3.6.** Underground application setup in Floz 8 at Zinnwald/Cinnovec mine with Spot and payload instruments facing UG-1 rock surface.

### 3.6 Validation

To validate data quality and accuracy, the results are compared to data and results from Kirsch et al. (2023a). This includes hyperspectral data of the samples acquired using the SisuRock hyperspectral scanning system and generated underground hyperclouds. The SisuRock scanner uses the Fenix hyperspectral camera and is widely used in multiple studies and scanning campaigns (Booyesen et al., 2022; Kirsch et al., 2022). Since the Fenix camera can acquire more accurate and resolute hyperspectral data, it can be used as a ground truth for comparing it with the Cubert X20P hyperspectral data. Multiple aspects of the hyperspectral data are visualised and qualitatively compared, such as band ratios and endmember extraction spectra. The Fenix endmember spectra are generated by performing the same endmember extraction on the lab rock samples. Comparing the hyperspectral data increases confidence in correlating and interpreting results from the proposed workflow.

The VLP16 LiDAR generated pointcloud of UG-1 is quantitatively compared to the photogrammetry cloud created by the Nikon D850 photo camera. In CloudCompare, common points between the two clouds are registered. The clouds are then scaled, aligned and subtracted. The distance information between pointclouds is then projected on the photogrammetry cloud. By calculating the distance between the VLP16 pointcloud and the photogrammetry cloud, the accuracy of the VLP16 pointcloud can be assessed.

# 4 Results

## 4.1 Lab Application

### 4.1.1 Exposure Time Comparison

Before applying hyperspectral analysing techniques, different exposure times are compared, as described in section 3.5.1. To gather information about the illuminating quality of each exposure time, pixel spectra of the white background for each exposure time are highlighted in Figure 4.1. Since the background wall is white, this should reflect all light and show the total illuminating spectrum. When comparing the white pixel spectra of each exposure time (Figure 4.1) to the average reflectance of the white reference spectra (Figure 5.1) I identify over-illumination in the 200 and 400 ms exposure times.

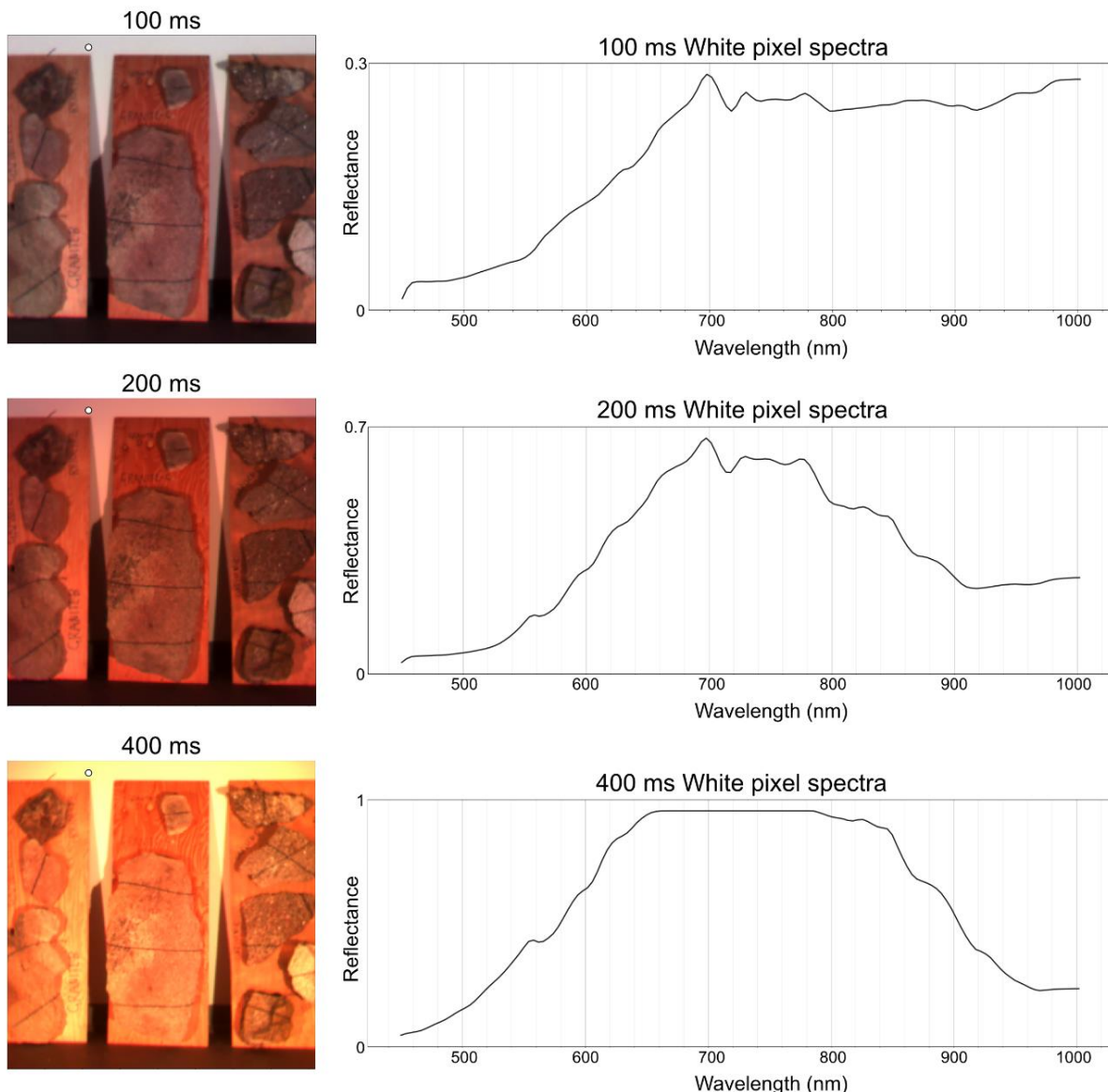


**Figure 4.1.** Lab application exposure time comparison. The left column shows RGB images of different exposure times. The right column shows the reflectance spectra of white pixels. The white pixel is highlighted as a white dot in the RGB images at (100, 40) in the pixel frame.

The 200 and 400 ms exposure times show a significant increase in the 600 to 900 nm wavelength range (Figure 4.1). While processing, the software gave an 'over-illumination' output message for the 200 and 400 ms. The 100ms image and spectra does not show an increase in the 600 to 900 nm wavelength range and did not cause any over-illumination alerts during processing. Thus, I decided to continue data analysis with the data collected at 100ms for the lab application.

#### 4.1.2 RGB Image

After hyperspectral data pre-processing, as described in section 3.1, the hyperspectral data can be directly visualised in *hylite* as an RGB image. Figure 4.2 shows an unmasked RGB visualisation of the rock samples and wooden board background. The spectral wavelengths used for RGB visualisation are 660, 550 and 480 nm. The granite rocks have an estimated mineral grain size of 0.1 to 0.5 cm, and the greisen rocks 0.1 to 2 cm,

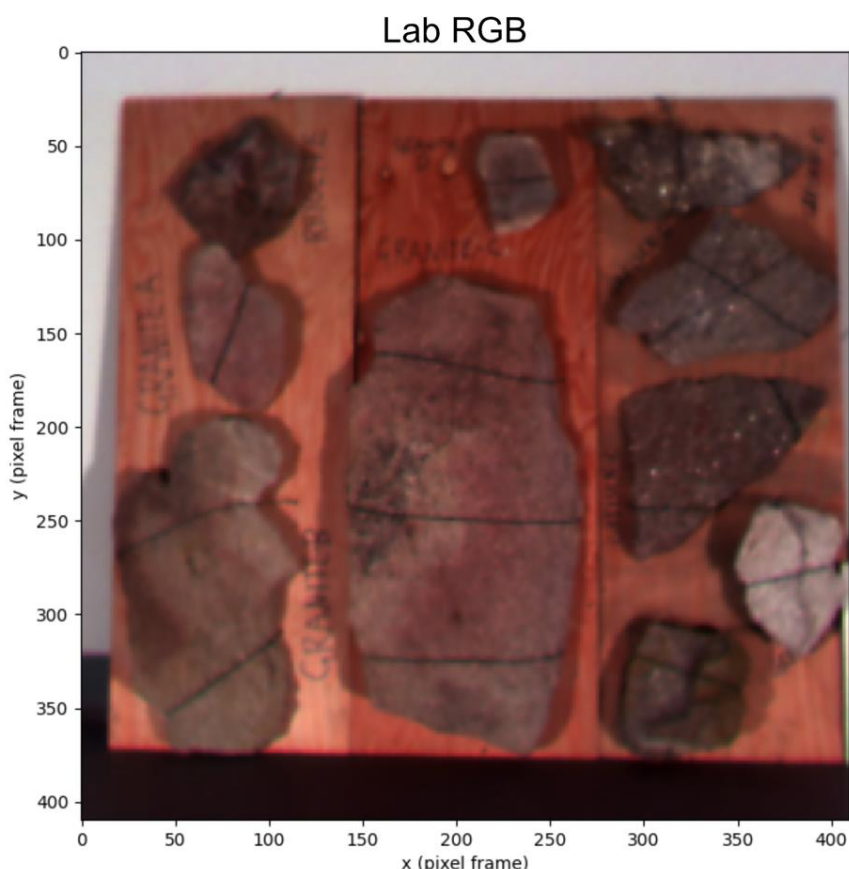


**Figure 4.2.** Lab application RGB image of wooden boards and rock samples. See Figure 3.4 for rock types.

#### 4.1.3 Band Ratio Analysis

Overall, the Cubert X20P visualisations of the Fe<sup>3+</sup> index look very similar to validation data from Kirsch et al. (2023a), acquired with the Specim Fenix in the SisuRock drill core scanner setup. The Cubert X20P and Fenix data show continuous shapes in absorbance features, as indicated by the red areas on Granite B and C (Figure 4.3). The Greisen E and D contain more singular and small specs that light up in the visualisation, indicated by black arrows in Figure 4.3. Greisen B appears relatively unreflective with a reflective index between 1.0 and 1.05 compared to more reflective areas in e.g. Granite A, B and C with reflective index 1.25. Features appear smoother in the Fenix visualisation and with less noise, such as in the shapes on Granite B and the overall shape of Granite C. The other low-intensity shape in Granite D is more defined in the Fenix image, as indicated by the green arrow in Figure 4.3.

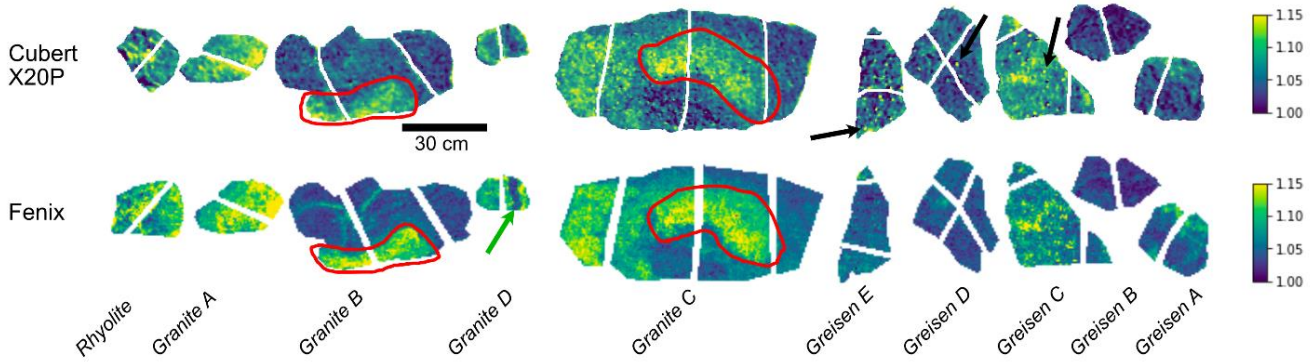


**Figure 4.3.** *Fe<sup>3+</sup> band ratio visualisation for Cubert X20P and Fenix from Kirsch et al. (2023a) with Rock ID and band ratio reflective index.*

#### 4.1.3 MNF and PCA

The MNF and PCA analysis outputs several bands/components that show geological information or noise in the hypercube dataset. To ensure all information is made visible, for both the MNF and PCA, nine bands/components are outputted. Appendix A-1,2 shows the output bands/components for MNF and PCA analysis. Granite B and C show different spectral signatures in the false colour maps, indicated by different colours (Figure 4.4). The Rhyolite, Granite A and Greisen B show a more homogeneous signature in the PCA analysis. Overall, a clear distinction between the granite and greisen rocks can be seen in the PCA false colour map in light green and pink in Figure 4.4. The Greisen B is again very distinguishable in both the MNF and PCA false colour maps. From the MNF and PCA analysis, six spectral classes are estimated for endmember extraction. This is estimated based on the amount of different spectral signatures seen in the false colour maps and trial-and-error when performing endmember extraction.

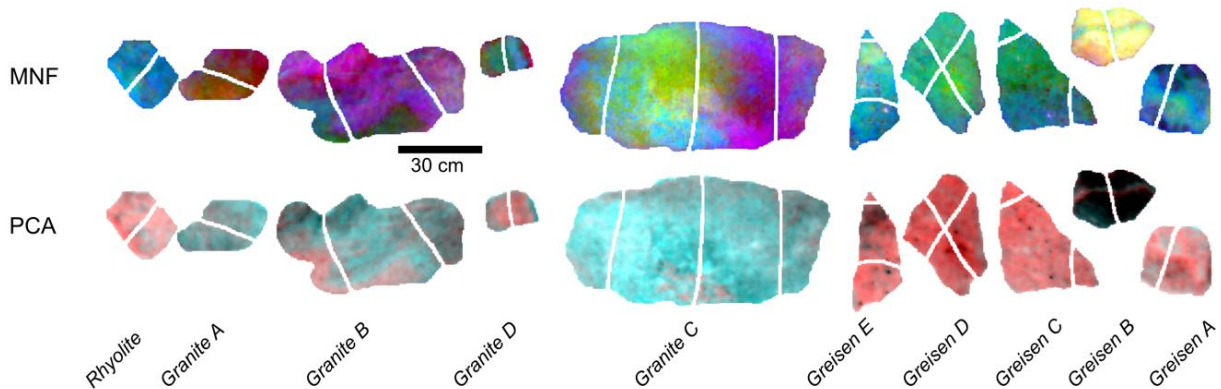


**Figure 4.4.** *MNF and PCA false colour visualisation with Rock ID. MNF false colour map is RGB composite from bands 1, 4 and 7. PCA false colour maps are RGB composite from components 1 and 2 (twice).*

#### 4.1.4 Endmember Extraction

The automated endmember extraction analysis takes the estimated six spectral classes derived from the MNF and PCA analysis above as a fixed input for the supervised NFINDR algorithm. The algorithm will then extract six spectral signatures from the hypercube data.

Endmembers 1 and 4, shown in the RGB scatter plot of Figure 4.5, appear close to the edge of the masked sample data. This is caused by the NFINDR algorithm possibly finding background spectra close to the edge, which is then grouped as a unique spectral class. Before being visualised, the end member spectra have been smoothed by a Savitzky-Golay filter (Savitzky & E, 1951). Endmembers 3 and 6 show relatively low absorption features and originate from the Rhyolite and Greisen B rock, respectively. The overall shape of the endmember 3 and 6 spectra is relatively similar. An absorption feature around 440-470

nm is present in most endmembers except endmembers 5 and 1. Other features are unique to specific endmembers, like the absorption feature of endmember 1 around 550 nm. The absorption feature around 900 nm is present in endmember 1 and 3. These endmembers are generated on the Greisen rocks E and D. Another feature around 750-800 nm shows in endmembers 4 and 3. The analysis in Chapter 5, section 5.1.1. correlates the endmember and mineral library spectra. The endmember extraction is also performed on the Fenix dataset from Kirsch et al. (2023a) and can be seen in Appendix B-4.

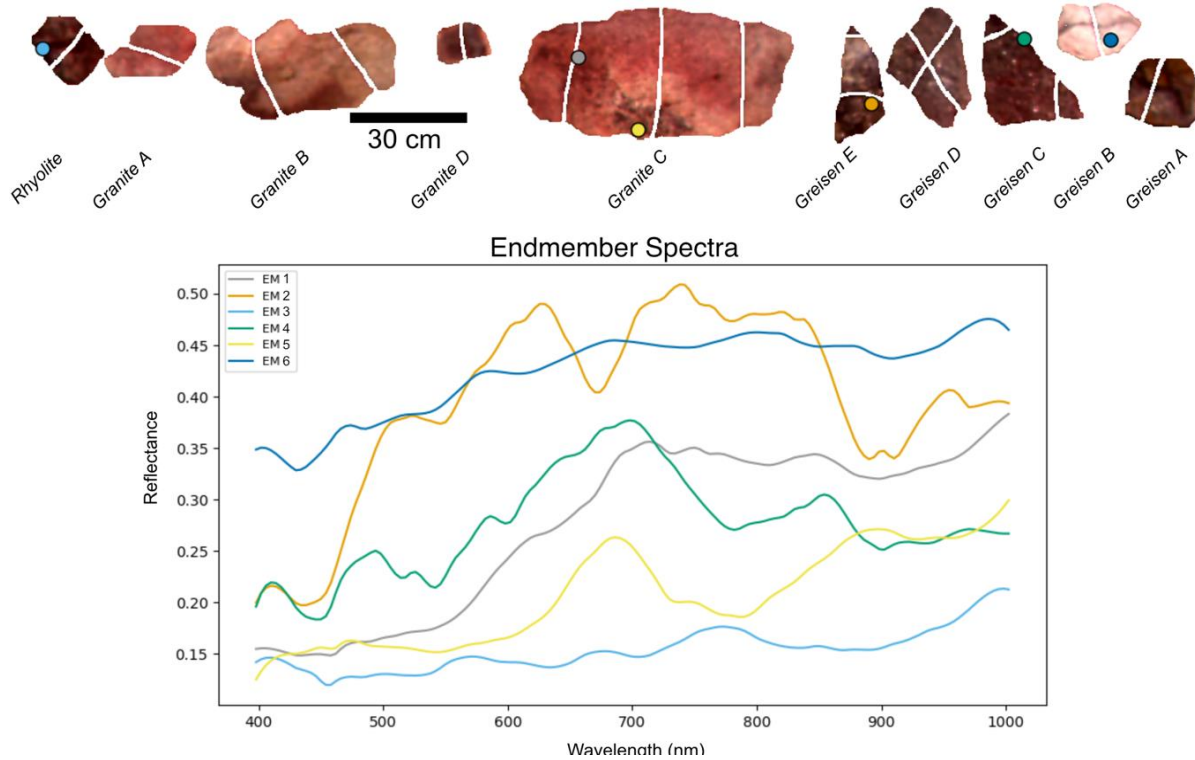


**Figure 4.5.** RGB visualisation of rock samples with corresponding unstacked endmember spectra.

#### 4.1.5 Abundance Maps

Using the endmember spectra, abundance maps are created using unmixing (Figure 4.6). Each map shows the relative abundance of a specific endmember spectrum on the lab sample surface. Each endmember map shows a distinct distribution on the rock samples. Endmembers 2 and 4 show features in intense specs in the Greisen rocks that only slightly appear in the granite rocks. Endmember 1 shows a distinct abundance in the granite rocks and is absent in the greisen samples. This is reversed in the distribution of endmember 3, where the granite rocks do not show abundance, and the greisen samples strongly do. The map for endmember 6 is unique for its intense abundance in the Greisen B rock, which is rich in kaolinite. Endmember 5 shows an increased abundance area in the centre of Granite C and low-intensity other granites and greisen rocks.

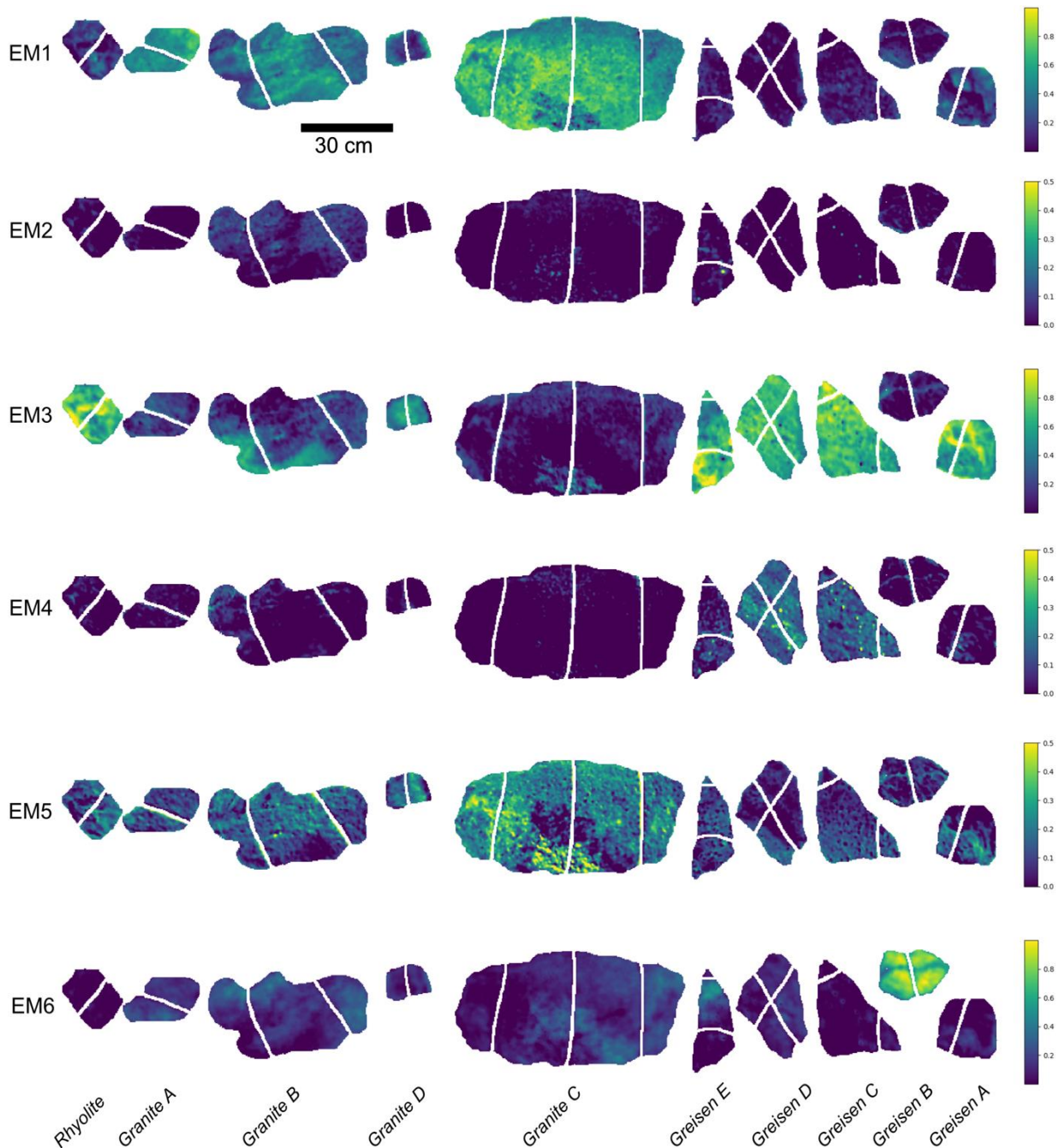


**Figure 4.6.** Endmember relative abundance maps with Rock ID. The scale shows the relative abundance of the spectral signal relative to the total spectral data. The scale is adjusted for abundance maps 2,3 and 4 to improve visualisation. EM1, 3 and 6 colour bars in the range 0.0 to 1.0 and EM2, 4 and 5 colour bars in the range 0.0 to 0.5.

#### 4.1.2 LiDAR Pointcloud

Combining the raw pointcloud data from all data capture angles forms a larger pointcloud, shown in Figure 4.7 (A). The pointcloud data does not contain a reflective intensity scalar or column, so the points are visualised in white. Because the LiDAR lasers do not reach the behind the rock samples and wooden boards, occlusions behind the Granite C rock are formed, indicated with the white arrow in Figure 4.7 (A). The data is gradually denser towards the bottom of the pointcloud. This is caused by only having additional pointcloud acquisition pitching Spot downward. The downward pitching pointclouds have an increased overlap, increasing the point density.

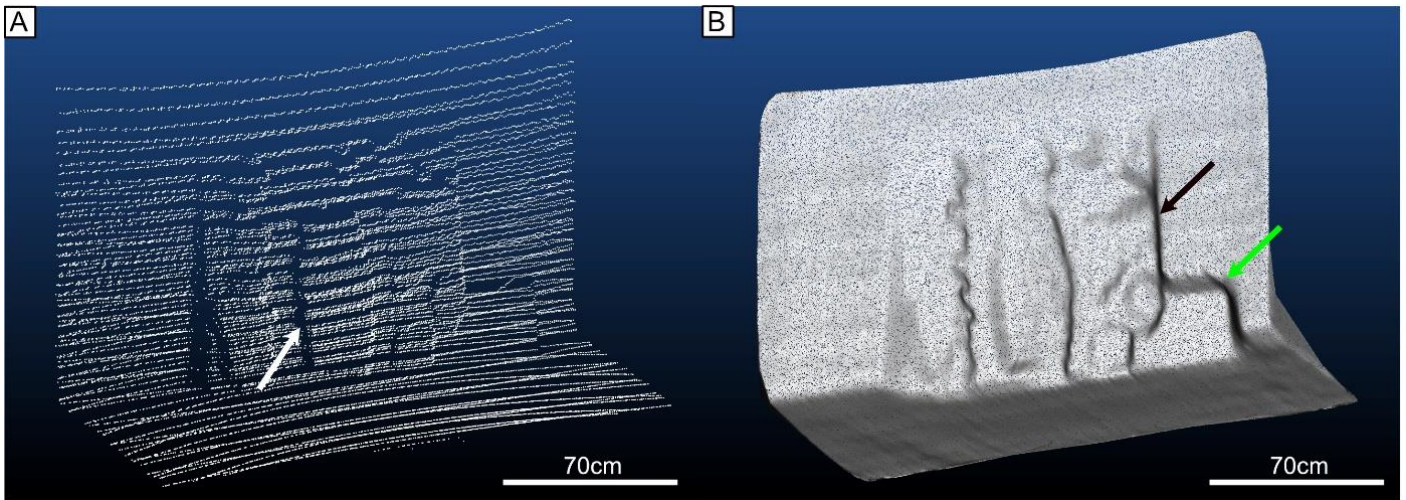


**Figure 4.7.** Raw (A) and processed (B) pointcloud in CloudCompare.

After processing in CloudCompare as described in section 3.3, the resulting pointcloud has increased point density, as shown in the comparison between Figure 4.7 A and B. The overall geometry of the sample boards is visible as sharp edges on either side, indicated by the black arrow in Figure 4.7 (B). The floor and wall sections are flat. However, we see a draping or curtaining effect on the rocks and wooden boards, losing some rough edges and creating inaccuracy at the board and floor contact. The square geometry on the scene's lower right indicated with the green arrow in Figure 4.7 (B), is an extra panel placed next to the wooden boards. Similar to the rock and wooden boards, this panel shows a curtaining effect in the processed pointcloud.

#### 4.1.3 Hyperclouds

After creating a virtual camera and manually matching data pixels with individual points in the cloud in our Python *hylite* environment, hyperclouds are created. The hyperclouds results are found in the digital Appendix C. In the RGB hypercloud, the left board and Granite B show a distortion or stretch towards the back wall, as indicated by the yellow arrow in Figure 4.8 (RGB). The top of the hypercube appears to be projected slightly too low relative to its pointcloud geometry, which is visible in all hyperclouds in Figure 4.8. For the Fe<sup>3+</sup> band ratio hypercloud, the sample mask has also been projected on the pointcloud, causing the background to be coloured grey, in contrast to the black background of the RGB and endmember abundance hyperclouds.

The endmember abundance maps are projected onto the pointcloud to create hyperclouds with endmember abundance information as scalars. These endmember scalars are then used as RGB colouring to form a false colour endmember hypercloud, as shown in Figure 4.8 (EM). Here, endmembers 1, 4 and 6 are chosen as RGB composite. A clear distinction can be seen between the granite (red/purple), greisen (green) and kaolinite-altered (blue) rocks.

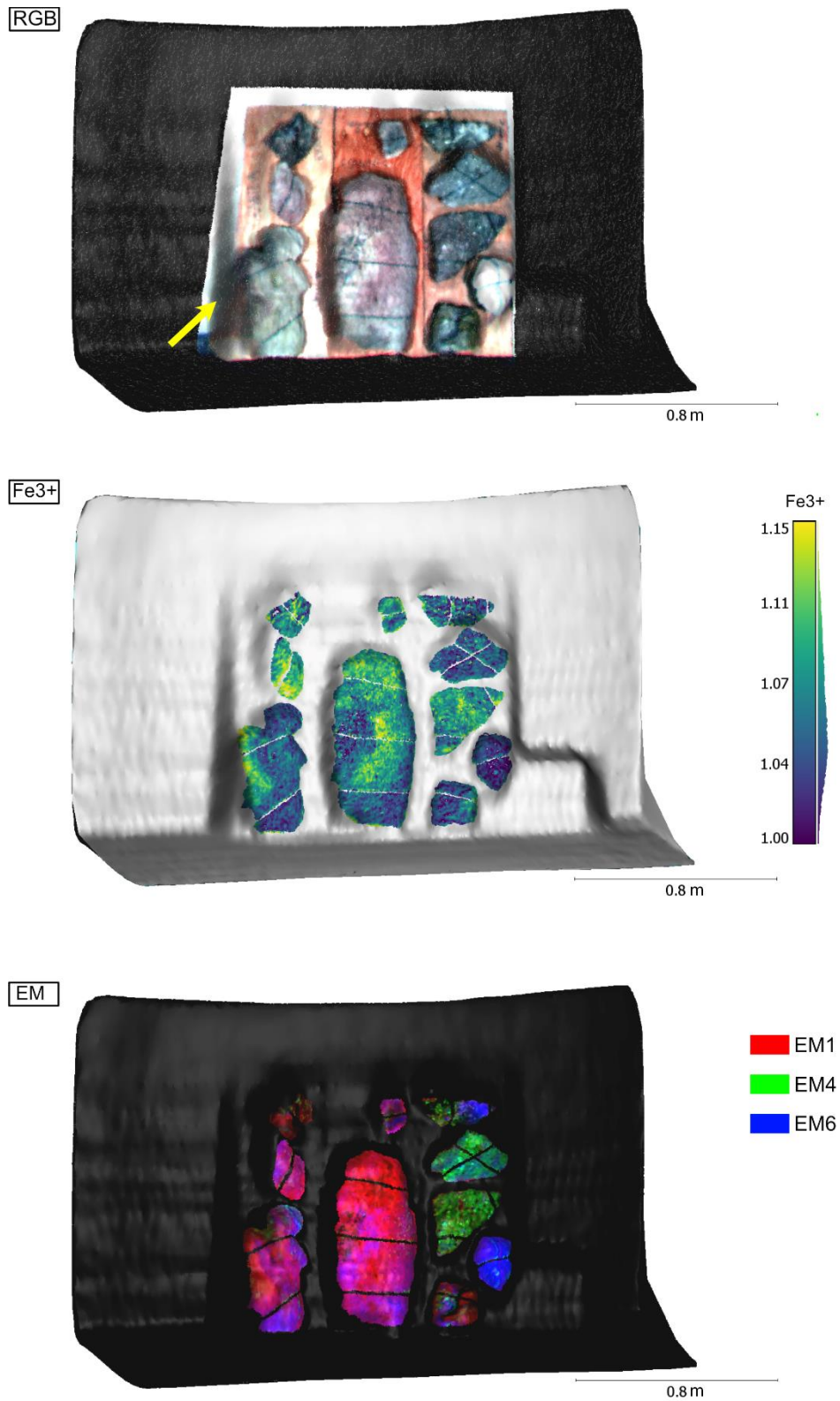


**Figure 4.8.** RGB,  $Fe^{3+}$  band ratio and endmember false colour projected hyperclouds. The background is coloured black and grey, containing no spectral attribute.

## 4.2 Underground

### 4.2.1 Exposure Time Comparison

Since the underground illuminating conditions differ from the lab application, a second exposure time comparison was done to determine optimal illuminating conditions (Figure 4.9). The average spectra of the white reference panel are compared for each exposure time in Appendix B-5. The comparison shows that all three exposure times show increased reflectance in the 400 to 900 nm range. However, when loading the hyperspectral data into the CUVIS SDK, the software would only indicate over-illuminated conditions for 400ms.

During Fe<sup>3+</sup> band ratio analysis, the 100 ms visualisation showed an unsharp image and vertical lines appear over the entire image, as seen in Figure 4.9 (100 ms). The 400 ms band ratio visualisation in Figure 4.9 notably shows a halo-shaped artefact over the image frame, creating dark areas around the frame corners and centre, indicated the white and red arrows respectively (Figure 4.9). The 200 ms dataset does not show vertical or halo-shaped artefacts or an unsharp image, and is therefore chosen to continue further analysis with.

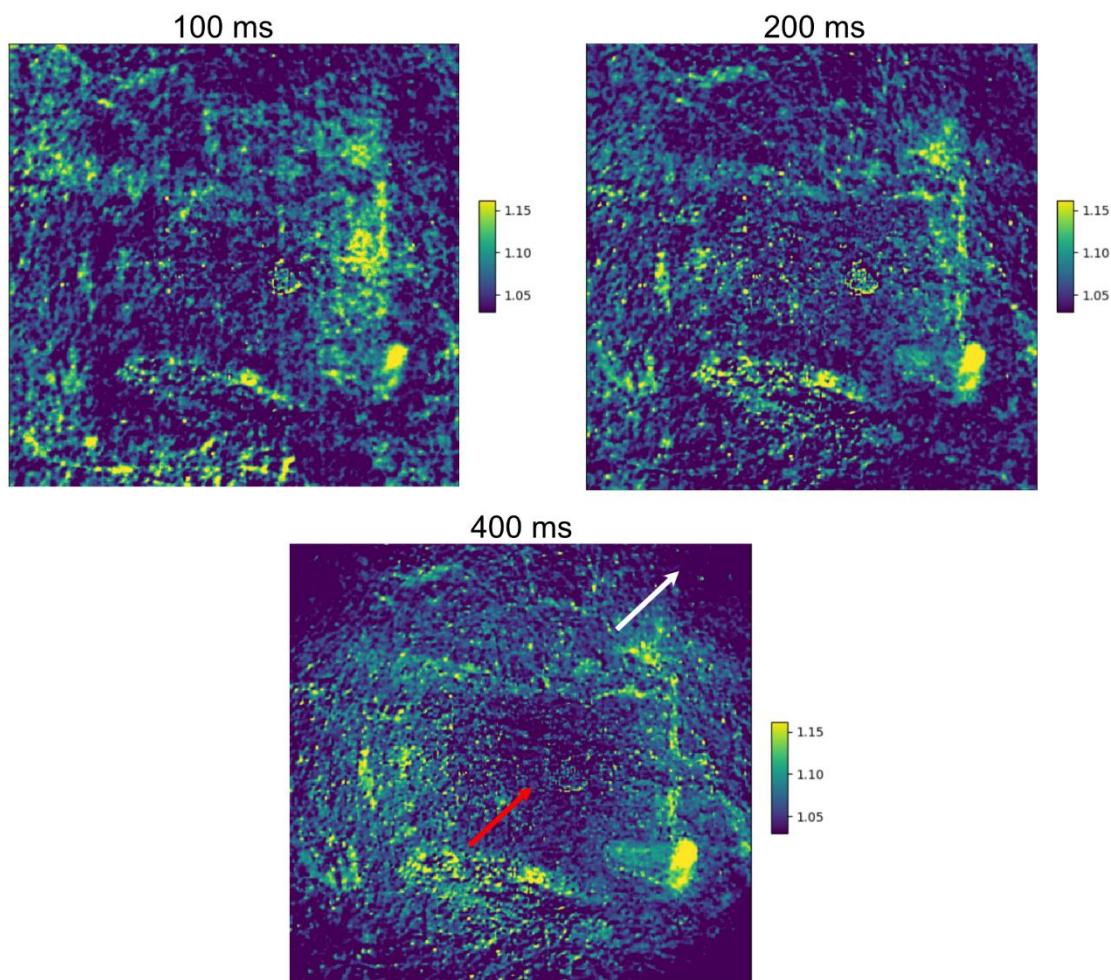


**Figure 4.9.** The Fe<sup>3+</sup> band ratio (600/570nm) analysis visualisations from UG-1 (neutral angle) for each exposure time. Image frame 1.2 by 1.2 m.

### 4.2.2 LiDAR Pointcloud

The underground pointcloud data was collected from positions UG-1 and UG-2 in Flöz 8, close to the entrance, as shown in Figure 4.10. The raw and fully processed point clouds can both be accessed and viewed online through the digital Appendix C.

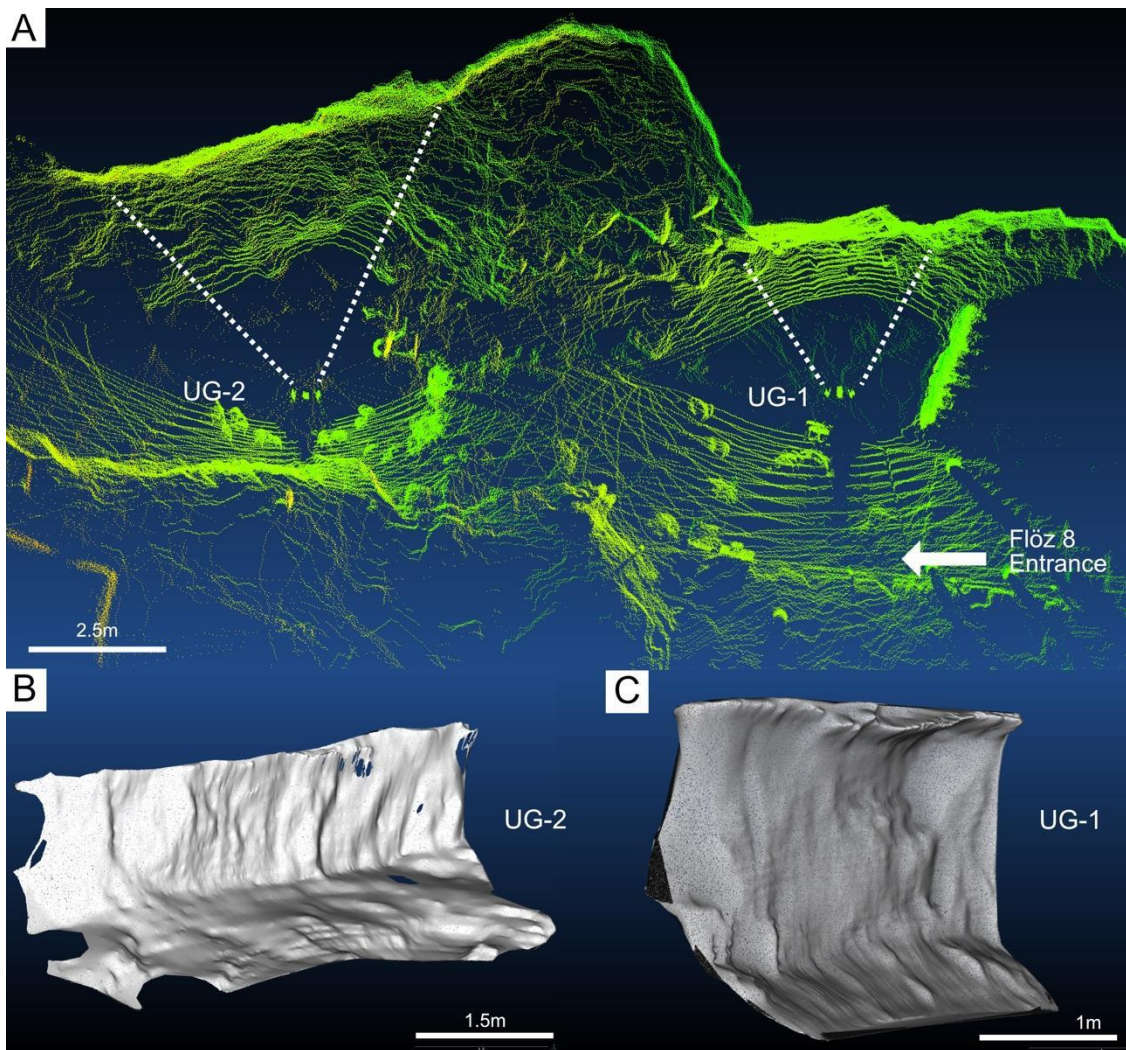


**Figure 4.10.** Top view of raw pointcloud of Floz 8 view (A) with indicated data acquisition surfaces (UG-1 and UG-2) and indicated Field of View (dotted lines). (B): processed pointcloud from UG-2 in indicated view. (C): processed pointcloud form UG-1 in indicated view.

The UG-1 processed pointcloud (Figure 4.10 C) shows no holes in the cloud surface but it does show some meshing errors in the ceiling points. The UG-2 processed pointcloud (Figure 4.10 B) shows holes in the point data and does not extend on the rock ceiling. As described in section 2.4.1, the angled lasers and the distance to the target create the spacing between data lines. The UG-1 pointcloud data was captured at 2 m and UG-2 4 m distance to the rock surface. UG-1 raw pointcloud has a relatively high point density compared to the UG-2 raw pointcloud since the point data was captured from different distances to the target.

### 4.2.3 UG-1 Hyperclouds

As described in the underground workflow of section 3.1, the underground hyperspectral data is directly converted into *hylite* scenes and then merged to create a single complete hypercloud. This hypercloud is

then used for hyperspectral analysis and visualisation. All resulting hyperclouds are shown in the digital Appendix C.

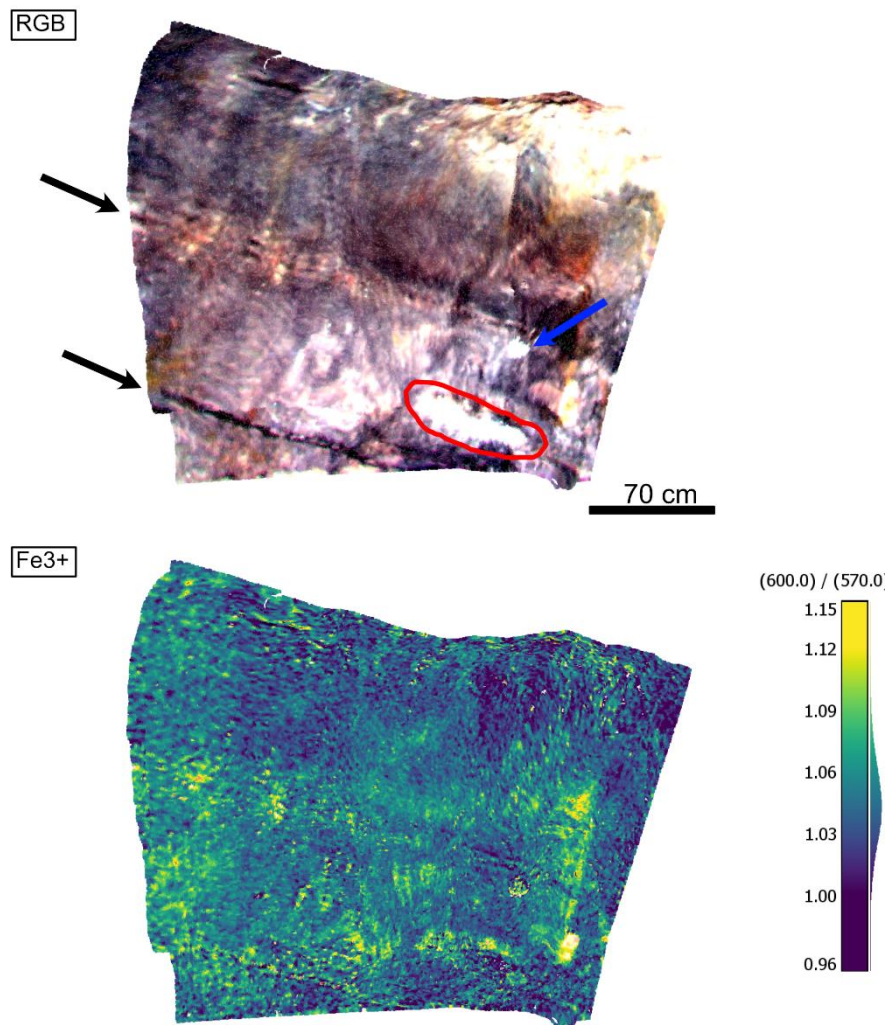


**Figure 4.11.** UG-1 hypercloud RGB and Fe3+ band ratio with absorbance intensity. Black arrows: veins, red area: lens structure, blue arrow: bright circular spot.

Both the RGB and Fe3+ hyperclouds show a slightly unsharp image (Figure 4.11). However, from the RGB image, two sub-horizontal vein structures dipping from left to right are distinguishable, indicated by black arrow in Figure 4.11 (RGB). A bright lens-like structure on the bottom right is indicated in red, and a bright circular shape on the rock surface by a blue arrow in Figure 4.11. The vein structures align with the schematic field sketch of the rock surface shown in section 3.5.3. These structures are not as apparent in the Fe3+ visualisation due to the unsharp nature of the hypercloud.

MNF and PCA hyperspectral analysis is performed on the UG-1 hypercloud and is shown in Appendix A-5. The MNF false colour map is based on band output 0, 3 and 5 (Appendix A-3). These bands were chosen for the false colourisation because they did not show shadowing effects or artefacts introduced by merging *hylite* scenes. The PCA false colour map is based on principal components 0, 1 and 2 (Appendix A-4). The first three output components showed the most variance and no processing artefacts. The MNF and PCA false colour maps show an extensive heterogeneity in the hyperspectral data as shown in Appendix A-5. The veins, lens-shaped structure and bright spec as indicated in Figure 4.11 are also visible in the MNF and PCA false colour maps.

Based on the MNF and PCA false colour maps, 5 to 7 spectral classes are determined as input for the endmember extraction. Varying the amount of spectral classes revealed an ideal result for five endmembers as input for automated extraction. With an increased number of endmembers spectral signatures above five would repeat. The Figure 4.12 RGB scatter plot shows that the end member extraction points are poorly distributed across the entire rock surface. The bright circular spot on the right of the surface has multiple endmember points in roughly the exact location but shows different spectra.

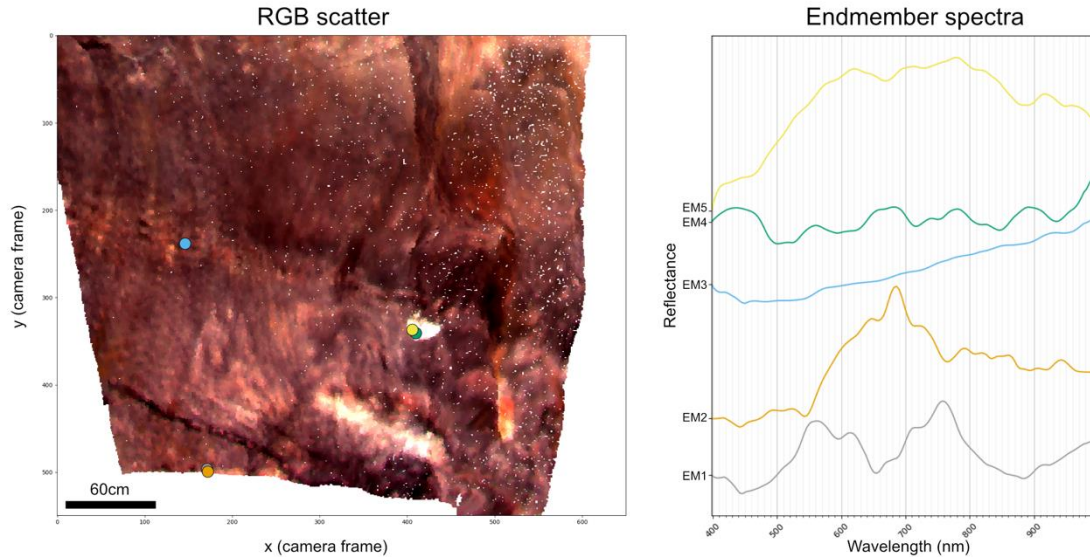


**Figure 4.12.** UG-1 endmember RGB scatter plot with custom camera object axes and corresponding stacked endmember spectra.

After the endmember extraction, the resulting spectra are used for spectral unmixing to create abundance maps. Appendix B-2 shows the spatial distribution of each endmember as a result of spectral unmixing. Endmembers 2, 4 and 5 show a similar spatial distribution over the rock surface, mainly located at the circular and lens-shaped feature on the right of the rock surface. This is consistent with the location of endmember extraction on these features, as shown in the Figure 4.13 RGB scatter plot. The analysis in Chapter 5, section 5.1.1. correlates the endmember to mineral library spectra.

The endmember distribution of EM 1, EM 2 and EM 3 are used to colourise the hypercloud RGB composite, as shown in Figure 4.13. These endmembers are used as an RGB composite based on their relative variability in spatial distribution on the rock surface. Endmembers 2, 4 and 5 all show similar spatial distribution in the circular and lens shapes on the right side of the rock surface. Therefore, the visualisation of endmember 2 in the RGB composite of Figure 4.13 also represents the spatial distribution of endmember 4 and 5. A circular and lens-shaped feature and an additional region on the top of the rock surface are highlighted by endmember 2 in blue in Figure 4.13. Two sub-horizontal vein structures are visible in the lower left and middle of the rock surface, highlighted by black arrows in Figure 4.13. The top vein is less defined and shows more hypercloud merging artefacts.

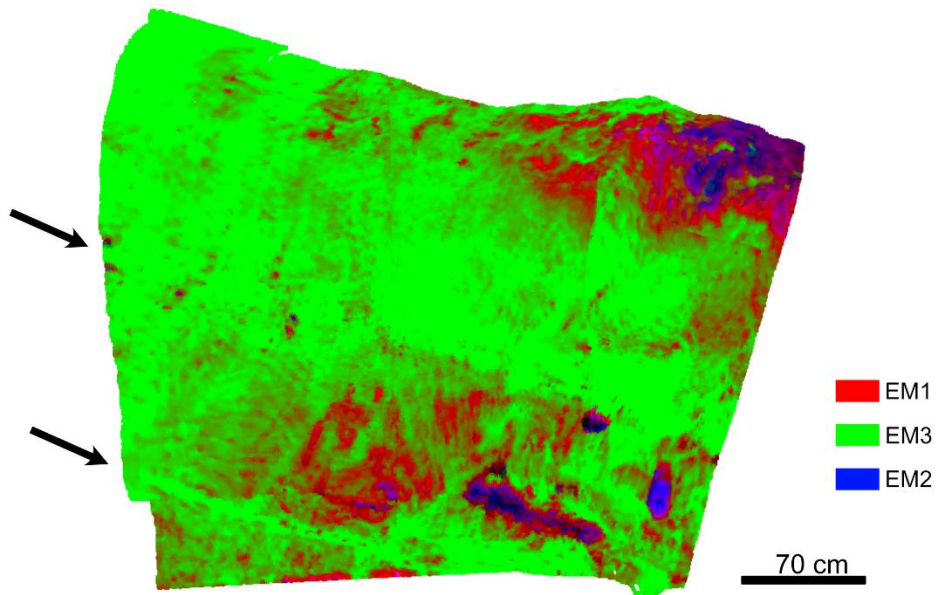


**Figure 4.13.** UG-1 endmember 1, 3 and 2 abundance map RGB colourisation.

#### 4.2.4 UG-2 Hyperclouds

The UG-2 RGB hypercloud (Figure 4.14) shows a reddish area in the middle of the rock surface and an angled vein structure. Similar to the UG-1 RGB, we see a slightly unsharp projection due to hypercloud merging artefacts. This can also be seen in the Fe<sup>3+</sup> band ratio visualisation (Figure 4.14), where the left area shows a different, distorted resolution. The right area of high intensity (in yellow) in the Fe<sup>3+</sup> band ratio hypercloud shows extensive shapes in the Fe<sup>3+</sup> band ratio visualisation, which correspond to the reddish surface area seen in the RGB hypercloud (blue arrows in Figure 4.14). The sub-horizontal vein can also be seen in the Fe<sup>3+</sup> band ratio visualisation.

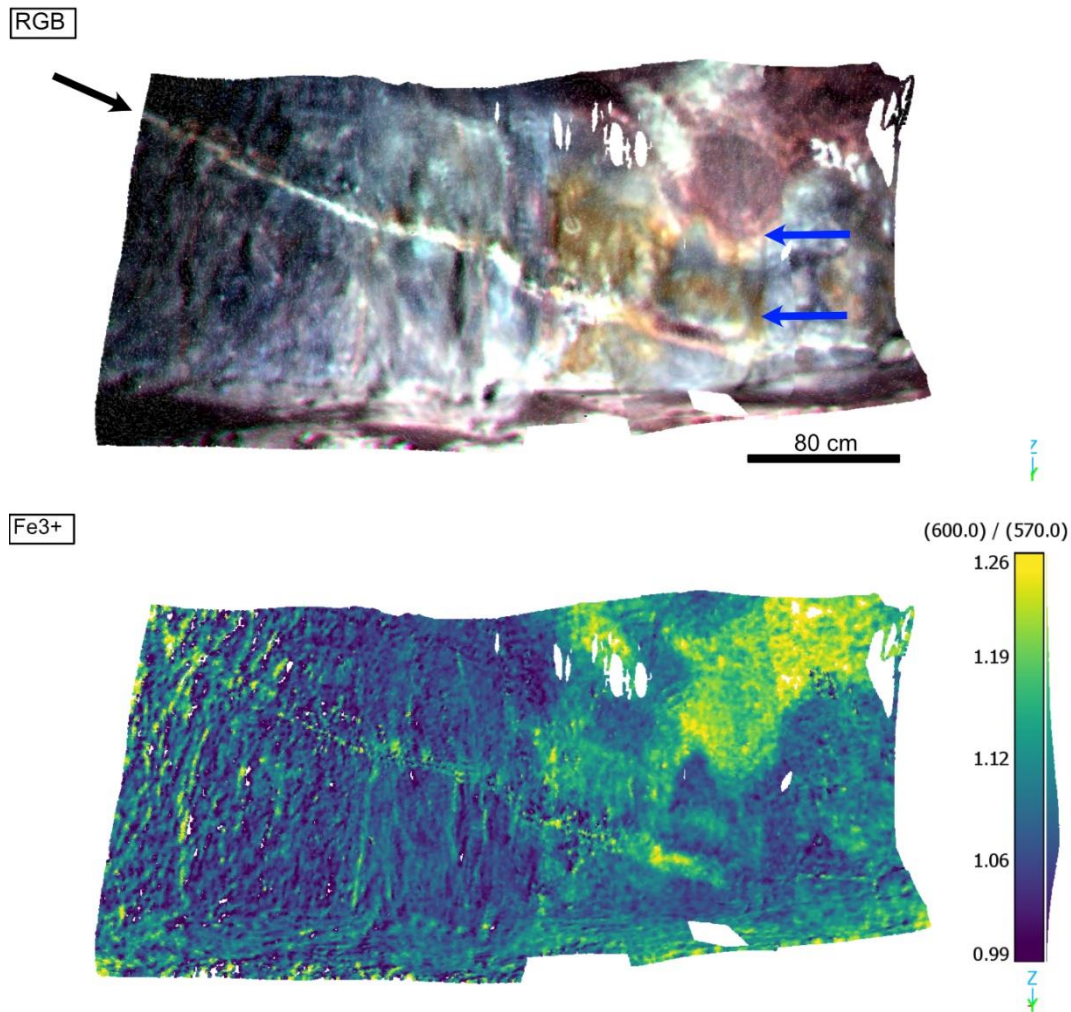


**Figure 4.14.** UG-2 hypercloud RGB and Fe3+ band ratio with absorbance intensity.

The output bands/components of MNF and PCA analysis performed on the UG-2 scene are found in Appendix A-5,6. The MNF false colour visualisation shown in Figure 4.14 consists of output bands 2, 3 and 4. The first MNF output band showed shadows on the rock surface and was therefore not used. The other bands all showed merging and or halo-shaped camera artefacts. The PCA false colour map is formed by principal components 1 and 2 since the other principal components again showed shadow effects or camera artefacts. The MNF and PCA, false colour visualisations, clearly show the sub-horizontal vein structure and the distinguishable shapes on the right of the rock surface. Additionally, the MNF and PCA false colour visualisation shows thin vertical lines on the left side of the UG-2 rock face (Appendix A-8).

Since the UG-2 scene comprises a larger rock surface, the MNF and PCA false colour colourisation show various spectra signatures. Based on the MNF and PCA analysis, 6 to 7 spectral classes can be distinguished and are used as input for the endmember extraction. Varying the amount of endmembers as extraction input showed that using seven spectral classes creates the best spatial coverage of the UG-2 surface. The RGB scatter in Figure 4.15 shows the seven endmember extraction points are well distributed across the rock face, resulting in extraction spectra on the vein structure and colorised (reddish) surfaces as seen in the RGB visualisation. In the resulting spectra, endmember 6 and 7 show similar shapes, whereas the other spectra all have unique features or shapes. The analysis in Chapter 5, section 5.1.1. correlates the endmember to mineral library spectra.

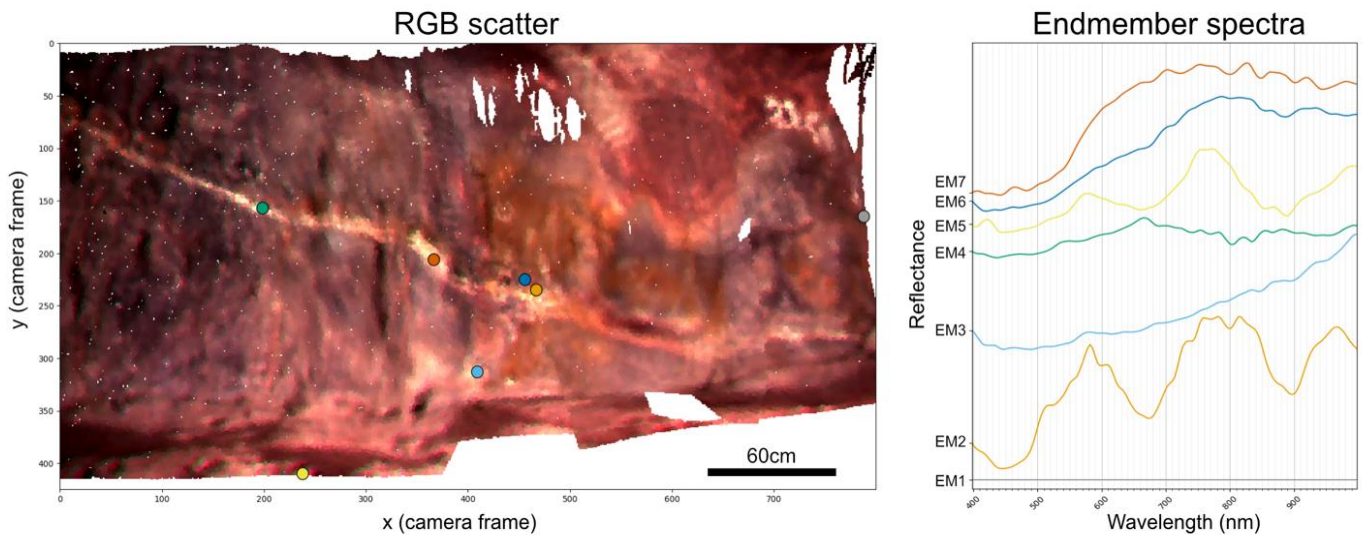


**Figure 4.15.** UG-2 endmember RGB scatter plot with custom camera object axes and corresponding endmember spectra.

The endmember spectra are unmixed, and abundance maps with information on spatial distribution are formed, which can be found in Appendix B-3. Endmembers 2 and 6 appear to have similar spatial distributions. In contrast, the other abundance maps are relatively unique. The endmember 1 abundance map resembles the MNF and PCA shadow output bands, which can be confirmed by its lack of spectral signature, as seen in Appendix A. Endmembers 3, 4 and 7 show the most variety in spatial distribution and are therefore combined as an RGB composite, as shown in Figure 4.16.

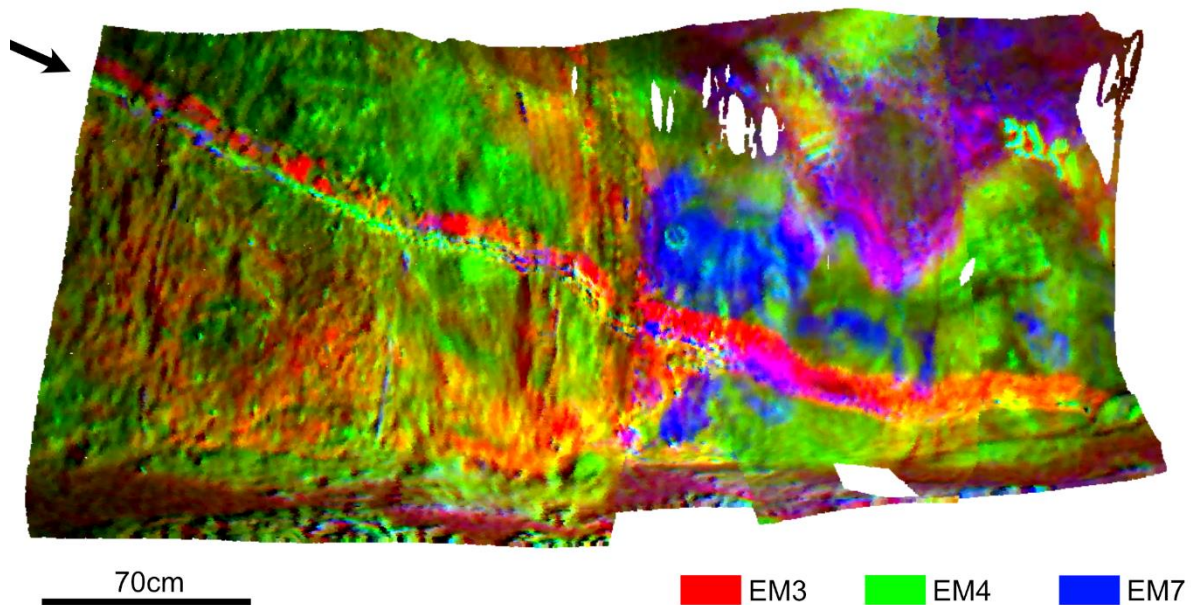


**Figure 4.16.** UG-1 endmember 3, 4 and 7 abundance map RGB colourisation.

# 5 Discussion

## 5.1 Hyperspectral

### 5.1.1 Exposure Time

In the lab and underground exposure time comparisons, we see an increased reflectance in the 500 to 900 nm wavelength range. This increased reflectance is caused by over-illumination of the halogen floodlights. The halogen floodlight spectra also show a slight increase in the 500 to 900 nm wavelength range, as shown in Figure 5.1. A longer exposure time allows more illuminating characteristics or noise to be captured in the data, thus causing an increased reflectance of the illuminating conditions (EIMasry & Sun, 2010). We see this in the 200 and 400 ms hyperspectral data of the lab application and all the hyperspectral data of the underground setting.

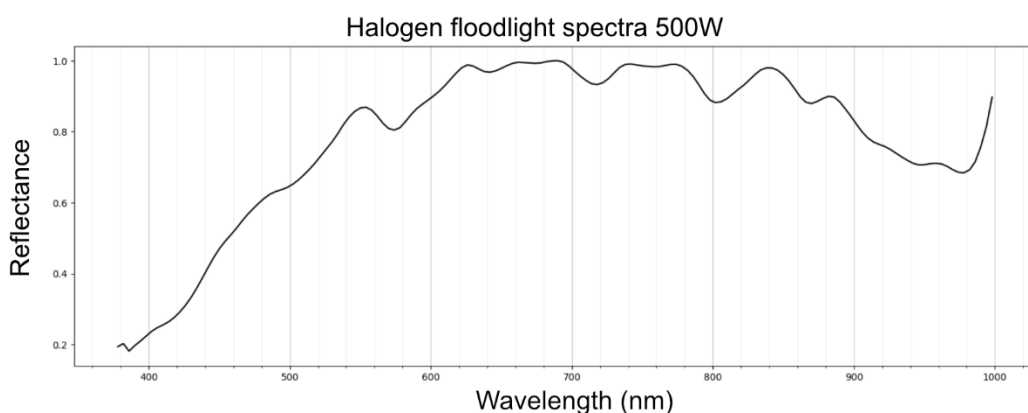


**Figure 5.1.** Halogen floodlight 500 W average spectra from white reference hypercube.

### 5.1.2 Band Ratio Analysis

The granite rocks in the lab application band ratio analysis showed more connected circular shapes, while the features in the greisen rocks appeared to be more singular in bright specs, as seen in section 4.1.3. This can be caused by two different effects: (1) crystal size and (2) mineral reflectance (Pontual et al., 1997). The fine-grained texture of the granite seems to be below the resolution of the Cubert20X and Fenix, which leads to a mix of absorption features per recorded pixel compared to the greisen, where larger crystals can be resolved, leading to the formation of single specs (Clark, 1999; Pontual et al., 1997). Therefore, the relatively large crystal size of the greisen rocks causes the singular bright specs in the spectral results.

The UG-1 Fe<sup>3+</sup> hyperclouds also show these singular bright specs because the hypercubes are captured from a distance of 2 m to the target surface. The UG-2 hyperclouds do not show singular bright specs, because it was taken from a larger distance of 4 m. Taking images from a larger distance decreases resolution and thus eliminates small features from the rock surface on the final image. In the UG-1 and UG-2 hypercloud, multiple sub-horizontal veins can be seen cutting through the granite host rock. These veins are secondary alteration features and contain large crystallisations of Li-Fe mica and zinnwaldite (Müller et al., 2018). The zinnwaldite's large mineral size and iron content cause the veins to light up in the underground band ratio hyperclouds. Other high-intensity areas in the underground Fe<sup>3+</sup> band ratio hyperclouds correspond to reddish areas in the RGB hypercloud. These areas are coloured red by iron oxide alterations, common on the greisen rocks of the Zinnwald Lithium mine (Štemprok & Šulcek, 1969). The high-intensity

Fe<sup>3+</sup> band ratio areas of the hyperclouds align with the hematite alteration areas in the schematic field sketch (Kirsch et al., 2023b) in section 3.5.3, confirming that the high-intensity contain iron minerals. Figure 5.2 shows that the Fe<sup>3+</sup> band ratio hypercloud of scene UG-2 has significant similarity to the generated hypercloud of the same rock surface from the Fenix hypercloud generated by Kirsch et al. (2023). The Fenix hypercloud (Figure 3B) shows an overall better resolution than the Cubert X20P hyperclouds (Figure 3A). Nevertheless, the sub-horizontal vein, hematite alteration zones and vertical faults in both hyperclouds.

Thin secondary vertical faults occur on the UG-2 rock surface (Kirsch et al., 2023b), which can be seen as thin vertical high-intensity lines on the left side of the Fe<sup>3+</sup> band ratio hypercloud in both Figure 5.2 A and B. Iron-rich fluids have likely been able to flow along the fault planes and oxidise, creating a Fe<sup>3+</sup> spectral feature in the band ratio analysis (Figure 5.2).

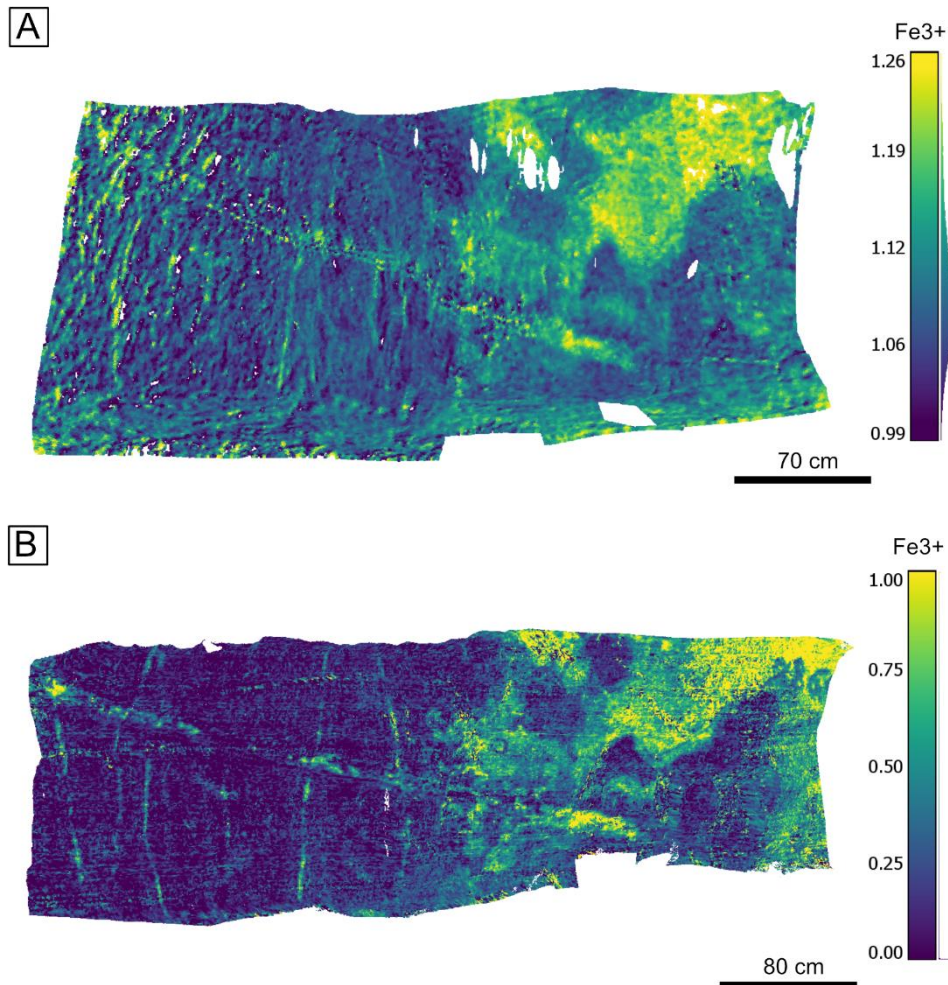


**Figure 5.2.** UG-1 (A) and Fenix (B) Fe<sup>3+</sup> band ratio hypercloud analysis comparison. Fenix hypercloud from Kirsch et al. (2023).

### 5.1.3 Mineral Correlation

The resulting lab and underground endmember spectra correlate with multiple VNIR spectral features from the mineral library spectra (section 1.5.3.), as shown in Figure 5.3. This section discusses each resulting endmember in terms of resulting spectra, spatial distribution and known lithology. If possible, the endmembers are then correlated to a mineral proxy. For the lab and underground application, the endmember-mineral correlations are summarised in Tables 5.1, 5.2 and 5.3 to provide a complete overview.

For the lab application, endmember 1 shows the Fe<sup>3+</sup> and Fe<sup>2+</sup> spectral features similar to hematite and goethite library spectra (Figure 5.3). Additionally, the spatial distribution of endmember 1, as seen in section 4.1.5, shows that the endmember is present on the altered granite rocks. Therefore, endmember 1 is correlated to hematite or goethite. Endmember 6 does not show iron spectral features, but the similarity in spectral shape and unique abundance on the kaolinite-altered greisen and granite rocks correlate to kaolinite minerals. Endmember 2, 4 and 5 are not correlated to a mineral due to a lack of diagnostic spectral and spatial features.

For the UG-1 application, endmember 2 shows features of Fe<sup>3+</sup> and Fe<sup>2+</sup> spectral absorbance features and is located in the hematite-altered zone of the UG-1 rock surface. The overall shape of the spectrum does not correspond to hematite or goethite (Pontual et al., 1997). Considering the possible absorbance features and location on the endmember extraction scatter and the overall shape of the spectra, endmember 2 is correlated to jarosite minerals. The overall spectrum shape of endmember 5 shows similarities to the hematite or goethite and is abundant in the altered zone of the UG-1 rock surface. Endmember 5 is, therefore, correlated to hematite and goethite minerals. Endmember 1 and 4 are not correlated to a mineral due to a lack of diagnostic spectral and spatial features.

For the UG-2 application, endmember 4 has faint iron absorption features that are present all over the rock surface. Because of the iron absorption features, endmember 4 is correlated to hematite, goethite or jarosite. Endmember endmembers 6 and 7 show apparent similarity between the hematite and goethite library spectra (Pontual et al., 1997). Looking at the spatial distribution of endmember 6 and 7, we see that endmember 6 is located on the sub-horizontal vein and altered area. In contrast, endmember 7 is more abundant in the hematite-altered zone. This distinction in spatial distribution leads to endmember 6 being correlated to goethite and endmember 7 to hematite. Endmember 1, 2 and 4 are not correlated to a mineral due to a lack of diagnostic spectral and spatial features.

In both the lab and underground applications, the endmember 3 spectra show remarkable similarity in overall shape. Although not able to correlate the endmember 3 spectra directly to mineral library spectra, the spatial distribution in all three scenes is unique compared to other endmember spatial distributions. Endmember 3 is located on the greisen rock zones and the vein structure in UG-1 and UG-2 for all three applications. The endmember 3 spectral signal could consist of several mineral spectral signals in the greisen rocks (Clark, 1999; Pontual et al., 1997). Therefore, endmember 3 indicates greisen zones on the rock surface, as noted in Tables 5.1, 5.2 and 5.3.

#### *5.1.4 Mineral Context*

The hematite and goethite iron minerals form in the Zinnwald/Cinnovec mine as a result of Fe-oxidation on the rock surface (Štemprok & Šulcek, 1969). This oxidation occurs by either iron rich fluids flowing across the rock surface or oxidation of iron from the greisen granite minerals itself. The Fe rich nature of the greisen granite micas could form a good supply for iron oxidation to occur on the rock surface. The hematite alteration forms extensive oxidised areas which generate diagnostic spectral iron features in the VNIR. Kaolinisation is able to occur in two ways: formation of clay minerals supplied by fluids along the rock surface or break down of feldspar minerals in the greisen and granite rocks (Štemprok & Šulcek, 1969; Stoch & Sikora, 1976). Hence, we see a strong kaolinite spectral signal, which is visible in the endmember abundance maps.

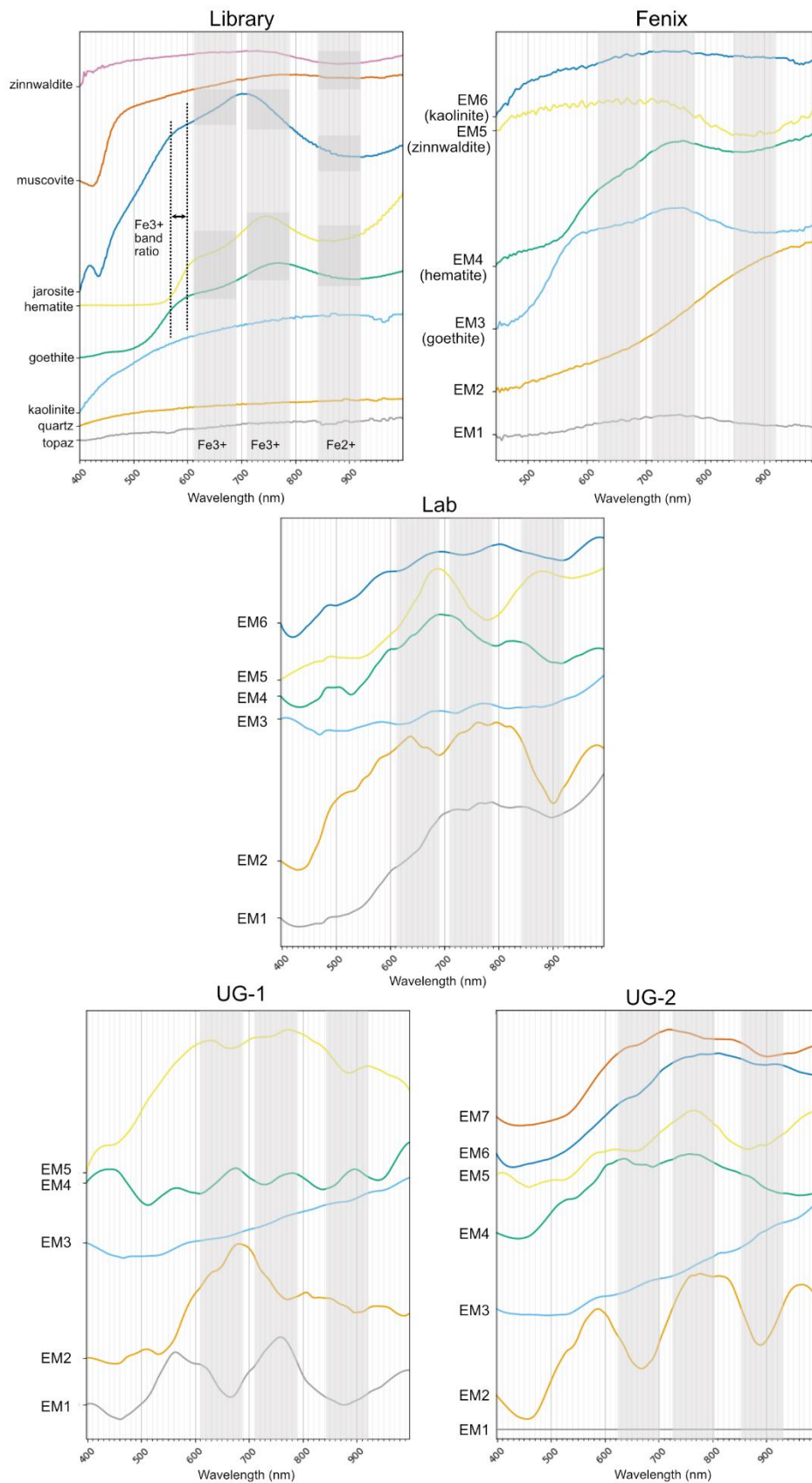


**Figure 5.3.** Mineral spectral library with Fenix, Lab an Underground application spectra from endmember extraction. Grey boxes indicate iron spectral feature zones.

**Table 5.1.** Lab endmember characteristics with interpreted mineral correlation.

| Lab | Spectral features and spatial distribution  | Mineral correlation  |
|-----|---|----------------------|
| EM1 | Fe3+ and Fe2+ absorption and iron ratio slope, alteration zones on granites.                              | Hematite or goethite |
| EM2 | Jarosite/muscovite spectra shape, single spec in greisen rock.  | -                    |
| EM3 | No iron features, abundant on greisen and rhyolite rocks.   | (Greisen)            |
| EM4 | No apparent iron features, bright specs on greisen rocks.   | -                    |
| EM5 | No apparent iron features, abundant on altered Granite C.   | -                    |
| EM6 | No spectral absorption but similar to kaolinite library spectra, abundant on kaolinite altered Greisen B. | Kaolinite            |

**Table 5.2.** UG-1 endmember characteristics with interpreted mineral correlation.

| UG-1 | Spectral features and spatial distribution                                      | Mineral correlation  |
|------|---|----------------------|
| EM1  | No iron features, abundant on greisen rocks.                                    | -                    |
| EM2  | Iron ratio slope and Fe3+ absorption features are abundant on the altered rock. | Jarosite             |
| EM3  | No iron features, abundant on greisen rocks.                                    | (Greisen)            |
| EM4  | No iron features are abundant on the altered rock.                              | -                    |
| EM5  | Iron ratio slope, roughly similar shape to iron minerals spectra.               | Hematite or goethite |

**Table 5.3.** UG-2 endmember characteristics with interpreted mineral correlation.

| UG-2 | Spectral features and spatial distribution   | Mineral correlation            |
|------|--|--------------------------------|
| EM1  | No iron features, possibly shadow.   | -                              |
| EM2  | No iron features, bright specs along vein structure.   | -                              |
| EM3  | No iron features, distributed along vein and greisen rock.                                     | (Greisen)                      |
| EM4  | Fe3+ and Fe2+ absorption, abundant on the vein, greisen rock and paint.                        | Hematite, Goethite or Jarosite |
| EM5  | No iron features, abundant on an entire rock surface.  | -                              |
| EM6  | Fe3+ and Fe2+ absorption and iron ratio slope features are abundant on veins and altered rock. | Goethite                       |
| EM7  | Fe3+ and Fe2+ absorption and iron ratio slope features are abundant on hematite-altered rock.  | Hematite                       |

## 5.2 LiDAR Pointcloud

Pitching the Spot and VLP16 LiDAR on multiple angles during data acquisition increases the pointcloud density in both the lab and underground application. However, processed pointcloud shows some horizontal artefacts caused by the line-based acquisition of the lasers in the VLP16. With an increased distance to the target, acquisition errors along the data laser line occur (Chan et al., 2020). These errors cause slight bumps in the resulting processed smoothed pointcloud. Additionally, the wooden boards and rocks show a curtaining effect towards the bottom due to the smoothing function of the generated mesh in CloudCompare. The smoothing factor can be reduced to reduce this curtaining effect, which also helps maintain the original rock geometry.

Since the UG-1 pointcloud was acquired closer to the target surface than the UG-2 surface, the UG-1 raw pointcloud shows greater point density and a better-processed pointcloud without any holes. This means that UG-2 has relied more heavily on the CloudCompare meshing tool for interpolating 'new' points. Meshing and a curtaining effect caused by the smoothing tool results in a slightly flattened lower quality pointcloud. This means that pointclouds acquired closer to the target surface require less processing and are of higher quality.

By calculating the absolute distance between the UG-1 and photogrammetry pointcloud in CloudCompare, the UG-1 pointcloud quality can be validated. Before calculating the absolute distance, the photogrammetry and UG-1 pointclouds are scaled and aligned, which is shown in Appendix B-6. The absolute distance is projected on the photogrammetry pointcloud since it has a higher point resolution than the raw UG-1 pointcloud. The lower part, ceiling and left part of the pointclouds have the highest absolute distance meaning the UG-1 pointcloud is least realistic in these areas, indicated by red arrow in Figure 5.4. This is caused by a curtaining effect in the lower and top parts of the pointcloud due to the CloudCompare smoothing tool connecting the vertical rock surface mesh with horizontal floor and ceiling mesh surfaces, creating a curtain effect between vertical and horizontal mesh surfaces. A curved line can be seen on the absolute distance visualisation indicated by the white arrow in Figure 5.4. This effect is caused by the UG-1 pointcloud cutting the photogrammetry cloud, causing a zero absolute distance to each other.

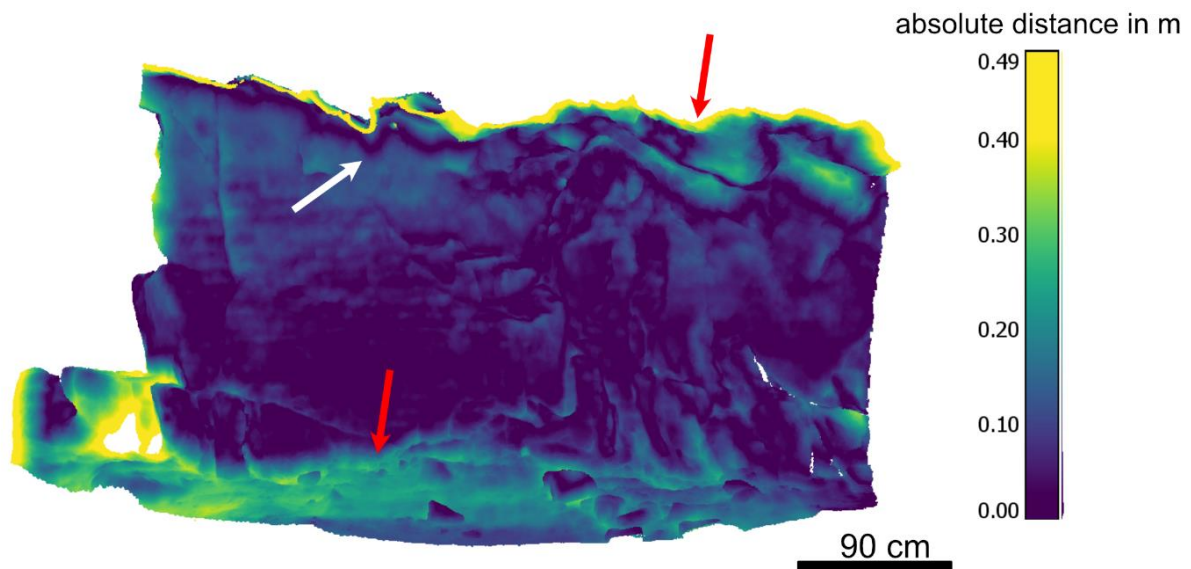


**Figure 5.4.** Absolute distance between UG-1 raw pointcloud and photogrammetry pointcloud.

# 6 Error Analysis

## 6.1 Hypercloud Merging Artefacts

The resulting hyperclouds of the lab application show a reasonable projection of the hyperspectral information on the pointcloud. However, the projection appears to have a downward offset at the top of the wooden boards. This is caused by the boards leaning onto the wall and thus not being perfectly vertical relative to the camera focus. A similar projecting artefact is seen on the RGB hypercloud in section 4.1.3, where the left of the projection appears to be stretched towards the back. This is caused by the projection being performed manually in Python, causing a discrepancy between the actual and projected camera frames. Projecting the hyperspectral data on the generated pointcloud in the lab application shows that the proposed workflow can produce corrected 3D hyperclouds containing hyperspectral and geometric information.

The underground hyperclouds are created by merging data from different angles. The merging is done by manually creating projection scenes in *hylite* based on the processed pointcloud and pixel information. Since each scene is created manually, slight offsets might occur between overlapping areas, causing merging artefacts in the resulting hypercloud. The heavily processed pointcloud is more flattened and thus makes it hard to estimate a corresponding point for hypercloud projection. This can be solved by increasing pointcloud density to improve manual projection or enabling automatic projection. To improve pointcloud density, the LiDAR data acquisitions can be optimised to create custom acquisition missions based on target conditions. By merging the possibly misaligned hypercloud projections, some data can appear duplicated or unsharp in visualisation. The merging artefacts can be seen in the UG-1 RGB and Fe3+ hypercloud in section 4.2.3. some features, like the sub-horizontal veins, are offset or appear duplicated. The UG-1 hyperclouds are created from a total of six merged *hylite* scenes. The UG-2 hyperspectral data is captured from a single position at three different horizontal angles, meaning only three *hylite* scenes were manually merged, reducing the amount of merging artefacts. The difference between the amount of merging scenes in UG-1 and UG-2 is seen in the quality of the hyperspectral data when comparing the overall hypercloud sharpness and endmember spectra quality, where the UG-2 hypercloud contains fewer merging artefacts.

The reduced sharpness in the UG-1 RGB and Fe3+ band ratio visualisations could also be caused by the custom distance calibration performed by the CUVIS SDK processing software. As mentioned in section 2.3, the Cubert X20P is calibrated for a 6m distance to the target by default and therefore need distance correction. Every hypercube is captured at a 6m distance calibration and later reprocessed to a custom distance using the CUVIS SDK software, as described in section 3.2. The hypercubes used in UG-1 and UG-2 were taken at 2 and 4 m distance to the target, respectively. This means the CUVIS SDK software had to correct for a greater distance in the UG-1 scene, potentially reducing data quality and sharpness. The increased CUVIS SDK distance processing combined with merging artefacts cause the UG-1 hypercloud to be of inferior quality relative to the UG-2 hyperclouds.

## 6.2 Halo Effect

During analysis for both Lab and underground applications, many visualisations showed a halo-shaped noise artefact in the data. The halo-shaped artefact creates dark corners and centres with a bright ring in between. Figure 5 shows the similarities between the halo-shaped artefact in the lab and UG-1 MNF band visualisation. PCA analysis does not show these features. As described in the exposure time comparison for the underground application in section 4.2.1, this halo effect is only present in the 400 ms exposure time visualisation, suggesting the effect is caused by over-illuminating conditions. However, even in 100 ms analysis output, like the Lab MNF band 2 in Figure 5.5, shows the halo effect present in the data. The halo effect is similar to what is called vignetting in photogrammetry. This can either be done on purpose or due to

illuminating, mechanical or software issues. The Cubert ULTRIS hardware and operation guide does not mention halo-shaped artefacts or vignetting issues (Cubert GmbH, 2023b). However, it mentions the possibility of the camera lens hood to cast a shadow on the suboptic lens, causing data errors. For all acquired hyperspectral data, the light sources have been located behind the camera, possibly casting a shadow on the lens. However, this is unlikely since the halo-shaped artefact appears vertically and horizontally symmetrical, meaning the light source must have caused perfectly symmetrical shadows on the lens. Therefore, the halo effect is likely caused by mechanical or software related issues causing a vignette effect in the data and images.

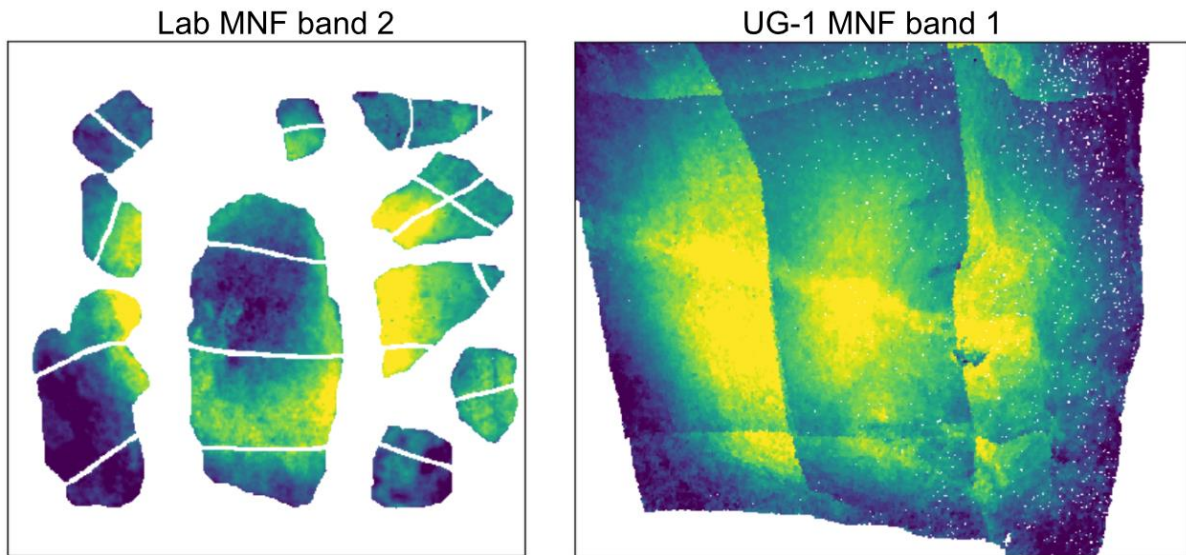


**Figure 5.5.** Lab application Minimum Noise Fraction (MNF) band 2 output and UG-1 MNF band 1 output.

# 7 Conclusion

The configured multi-sensor robotic platform has been shown to successfully acquire hyperspectral and geometric data in an underground mining environment to be processed into hyperclouds for various analytical purposes. It is surprising to see that with only a minor hyperspectral sensor setup, extensive results and information can already be created. The proposed workflow can process and enhance data quality in pre-processing, followed by manual hypercloud projection in *hyllite*. Spectral analysis on the generated hyperclouds provides interpretable results on the lab samples and underground rock surfaces from the Zinnwald/Cinnovec mine.

Some of the hyperspectral and geological outcomes are:

- Fe<sup>3+</sup> band ratio analysis can be used to recognise faults, vein type structures and alteration areas due to the oxidation of iron along the rock surface.
- Iron minerals such as hematite, goethite and jarosite can be confidently correlated to endmember extraction and spectral unmixing results of both the lab and underground applications.
- Kaolinite does not have diagnostic spectral features in the VNIR but can confidently be correlated to endmembers based on spatial distribution and overall spectra shape in both the lab and underground applications.
- Similarities between spectral endmembers between lab and underground applications suggest a spectral signature unrelated to a specific mineral but an indicator for greisen lithology in the VNIR for the analysed samples and rock surfaces. This spectra signature is likely a mixture of multiple mineral spectra or an undiagnostic mineral in the VNIR range.

Some workflow and instrument-related outcomes are:

- The ideal exposure times are determined to be 100 and 200 ms for the lab and underground applications, respectively (Figure 4.1 and 4.9).
- LiDAR data acquisition from multiple angles of the same target effectively increases point density. Processing the combined pointcloud in CloudCompare using a meshing, smoothing, and sampling tool creates a dense pointcloud for hypercloud projection. However, the Extensive use of tools smooths the real rock geometry and introduces several processing artefacts (Figures 4.7 and 4.10) like the curtaining effect.
- A curtaining effects occurs between the intersection of vertical and horizontal meshes at the pointcloud ceiling and floor, caused by extensive processing in CloudCompare (Figure 5.4).
- Merging of manually projected hyperclouds introduces duplicating effects in the hyperspectral attributes which reduces data quality (Figure 4.11).
- The Cubert X20P camera or processing software generates halo-shaped artefacts in the hyperspectral data, related to either mechanical or software issues (Figure 5.5).

The results have been validated using an existing study on the Zinnwald/Cinnovec mine rocks, showing similar spectral features in the VNIR and comparable 3D pointclouds. The versatile nature of Spot allows the configured system to acquire data in rugged underground mining environments. With a comprehensive manual on the Cubert X20P and performing data acquisition missions, the multi-sensor robotic platform shows excellent potential to complement mineral exploration research and create a safer underground work environment.

## 7.1 Recommendations and Future Research

Instrumental characteristics limit the current capabilities and quality of geological products. The Cubert X20P is limited to the VNIR spectra range, meaning only iron spectral absorption features are captured. Expanding the spectral range of the hyperspectral sensor would increase the spectral capabilities and resulting geological products. However, the Spot robotic platform is limited by a maximum payload weight, and an unobstructed view for the VLP16 LiDAR should be maintained (Boston Dynamics, 2022, 2023d). An ideal solution here is to mount a small and lightweight hyperspectral sensor that can capture a more extensive range of the electromagnetic spectrum. This way, future research will be able to potentially explore a greater range of mineral assemblages and settings.

Highly optimised LiDAR acquisition missions have been shown to significantly improve point density in aerial and terrestrial scanning systems (Andrew Lassiter et al., 2020; Bula et al., 2020). Increasing pointcloud density makes the proposed workflow less reliant on CloudCompare tools and processing, creating a more realistic pointcloud without curtaining or line artefacts. This way, manual projection of hyperspectral on the 3D pointcloud is more straightforward, reducing the error. Automating the hypercloud projection is possible when the LiDAR pointcloud has an additional spectral attribute in the data that can be automatically matched and co-registered to the hyperspectral data. Implementing more automation in future research and development of the robotic platform will create a realistic hypercloud projection and reduce error significantly. With accurately projected hypercloud, they can be merged without duplicating any hyperspectral information and create a sharp hypercloud.

In future research, a step towards autonomous data acquisition should be made to increase the impact on underground safety. The current method is manual and requires the operator to be in proximity (5 m max) of the robotic platform. Implementing a Simultaneous Localisation and Autonomous Mapping (SLAM) algorithm would allow Spot and the sensor to acquire data entirely autonomously. Existing SLAM algorithms can effectively map using Boston Dynamics Spot and the VLP16 LiDAR (Morenville et al., 2022; Nilsson, 2022). However, hyperspectral data is essential in geologically mapping underground environments and is not obtainable through existing SLAM algorithms for mineral exploration. Therefore, developing and implementing a 'hyperspectral SLAM' algorithm would allow autonomous data acquisition in underground environments and increase the impact on underground safety. Developing an autonomous data acquisition method in future research fully unlocks the safety potential of the multi-sensor robot platform proposed in this thesis.

In the current method, the halogen light source must be manually placed, focused on the target surface, and visually evaluated. Mounting the light source for hyperspectral imaging on a robotic platform has improved data acquisition workflows for robot platforms (Hyunseob et al., 2023b). To improve illuminating conditions in future research a light source could be mounted on Spot's back, rotating with the Spot body frame and Cubert X20P focus to improve illuminating conditions and remove a data correction step in the workflow.

## 7.2 Outlook

With underground mining becoming increasingly deeper due to the complex nature of ore bodies, this method can potentially form a safe and efficient method for mineral exploration. For the platform to be applied industry-wide, improvements must be on the platform autonomous capabilities and hyperspectral- and pointcloud quality. However, this study configures a basis for the multi-sensor robotic platform, which can be further optimised and is able to perform custom underground data acquisition missions. Data acquisition is done manually but the created platform has a lot of scope to improve in the future. The current method is able to detect minerals in the VNIR range only, but can already give geological information with only a small hyperspectral setup. Expanding the sensor range on the electromagnetic spectrum would significantly increase the quality of geological products and enable the exploration of more ore body types.

# Bibliography

- Andrew Lassiter, H., Whitley, T., Wilkinson, B., & Abd-elrahman, A. (2020). Scan pattern characterization of velodyne VLP-16 lidar sensor for UAS laser scanning. *Sensors (Switzerland)*, 20(24), 1–21. <https://doi.org/10.3390/s20247351>
- Ares, R. (2018). *The MIN-GUIDE Policy Guide Guidance for EU and MS mineral policy and legislation Deliverable 1.3, Version 1 Minerals Policy Guidance for Europe*. [www.min-guide.eu/](http://www.min-guide.eu/)
- Bertrand, G., Cassard, D., Arvanitidis, N., & Stanley, G. (2016). Map of Critical Raw Material Deposits in Europe. *Energy Procedia*, 97, 44–50. <https://doi.org/10.1016/j.egypro.2016.10.016>
- Booyesen, R., Jackisch, R., Lorenz, S., Zimmermann, R., Kirsch, M., Nex, P. A. M., & Gloaguen, R. (2020). Detection of REEs with lightweight UAV-based hyperspectral imaging. *Scientific Reports*, 10(1), 1–12. <https://doi.org/10.1038/s41598-020-74422-0>
- Booyesen, R., Lorenz, S., Thiele, S. T., Fuchsloch, W. C., Marais, T., Nex, P. A. M., & Gloaguen, R. (2022). Accurate hyperspectral imaging of mineralised outcrops: An example from lithium-bearing pegmatites at Uis, Namibia. *Remote Sensing of Environment*, 269(May 2021). <https://doi.org/10.1016/j.rse.2021.112790>
- Boston Dynamics. (n.d.). *SPOT User Guide*.
- Boston Dynamics. (2022). *Spot CORE payload reference*. <https://bostondynamics.my.site.com/SupportCenter/s/article/Spot-CORE-payload-reference>
- Boston Dynamics. (2023a). *Spot Specifications*. <https://support.bostondynamics.com/s/article/Robot-specifications>
- Boston Dynamics. (2023b). *Payload device network configuration*. <https://support.bostondynamics.com/s/article/Payload-device-network-configuration>
- Boston Dynamics. (2023c). *Spot Developer Documentation*. 3.3.0. <https://dev.bostondynamics.com>
- Boston Dynamics. (2023d). *Spot Enhanced Autonomy Payload (EAP)*. <https://support.bostondynamics.com/s/article/Spot-Enhanced-Autonomy-Package-EAP>
- Boston Dynamics. (2023e). *Spot, The Agile Mobile Robot*. <https://www.bostondynamics.com/products/spot>
- Breiter, K., Förster, H. J., & Seltmann, R. (1999). Variscan silicic magmatism and related tin-tungsten mineralization in the Erzgebirge-Slavkovsky les metallogenic province. *Miner Deposita*, 34(5–6), 505. <https://doi.org/10.1007/s001260050217>
- Buckley, S. J., Kurz, T. H., Howell, J. A., & Schneider, D. (2013). Terrestrial lidar and hyperspectral data fusion products for geological outcrop analysis. *Computers and Geosciences*, 54, 249–258. <https://doi.org/10.1016/j.cageo.2013.01.018>

- Bula, J., Derron, M.-H., & Mariethoz, G. (2020). Dense point cloud acquisition with a low-cost Velodyne VLP-16. *Geosci. Instrum. Method. Data Syst*, 9, 385–396. <https://doi.org/10.5194/gi-9-385-2020>
- Casas-García, R., Rapprich, V., Repstock, A., Magna, T., Schulz, B., Erban Kochergina, Y. V., & Breitzkreuz, C. (2021). Crustal vs. mantle contributions in the Erzgebirge/Krušné hory Mts. magmatism: Implications for generation of zoned, A-type silicic rocks in the late-Variscan Altenberg-Teplice Caldera, Central Europe. *Lithos*, 404–405. <https://doi.org/10.1016/j.lithos.2021.106429>
- Chan, T. O., Cosandier, D., Systems, N., & Durgham, K. (2020). Range Scale-Factor Calibration of the Velodyne VLP-16 LiDAR System for Position Tracking Applications. *The 11th International Conference on Mobile Mapping Technology, April*, 350–355. <https://www.researchgate.net/publication/340600566>
- Clark, R. N. (1999). *Spectroscopy of Rocks and Minerals, and Principles of Spectroscopy* (Vol. 3). Wiley and Sons.
- CloudCompare. (2023). *CloudCompare User Guide*. [https://www.cloudcompare.org/doc/wiki/index.php/Main\\_Page](https://www.cloudcompare.org/doc/wiki/index.php/Main_Page)
- Cubert GmbH. (2023a). *Application Notes Cuvis SDK for Linux*.
- Cubert GmbH. (2023b). *ULTRIS / ULTRIS Plus Hardware and Operation Guide*.
- Cubert GmbH. (2023c). *ULTRIS X20 and ULTRIS X20 pan - set Custom Distance*.
- Cubert GmbH. (2023d). *ULTRIS X20 PLUS Specifications*. <https://www.cubert-hyperspectral.com/products/ultris-x20-plus>
- Cubert GmbH. (2023e). *Cubert X20 PLUS*. <https://www.cubert-hyperspectral.com/products/ultris-x20-plus>
- Dittrich, T. (2020). *The Zinnwald Lithium Project: Transferring legacy exploration data into new mineral resources*.
- ElMasry, G., & Sun, D. W. (2010). Principles of Hyperspectral Imaging Technology. *Hyperspectral Imaging for Food Quality Analysis and Control*, 3–43. <https://doi.org/10.1016/B978-0-12-374753-2.10001-2>
- European Commission. (2014). *Report of the Ad hoc Working Group on defining critical raw materials*.
- European Commission. (2020). *Critical Raw Materials Resilience: Charting a Path towards greater Security and Sustainability*. <http://info.worldbank.org/governance/wqi/>.
- Förster, N. (1999). Late-Collisional Granites in the Variscan Erzgebirge, Germany. *J Petrol*, 40(11), 1613. <https://doi.org/10.1093/petrology/40.11.1613>
- Glennie, C. L., Kusari, A., & Facchin, A. (2016). CALIBRATION AND STABILITY ANALYSIS OF THE VLP-16 LASER SCANNER. *The International Archives of the Photogrammetry, Remote Sensing and Spatial Information Sciences*, XL-3/W4, 55–60. <https://doi.org/10.5194/isprs-archives-xl-3-w4-55-2016>

- heuristics. (2023). *Spot ROS (package) driver*. [https://github.com/heuristicus/spot\\_ros](https://github.com/heuristicus/spot_ros)
- Howden Company. (2019). *We Need To Talk About Mining: Death, Dangers & Prevention*. <https://www.howden.com/en-us/articles/mining/we-need-to-talk-about-mining>
- Hyunseob, B., Son, Y.-S., & Kim, K.-E. (2023a). *Development and Application of 3D Hyperspectral Scanning System for Underground Mine and Tunnel Exploration*. 0–9. <https://doi.org/10.36227/techrxiv.21815508.v1>
- Hyunseob, B., Son, Y.-S., & Kim, K.-E. (2023b). *Development and Application of 3D Hyperspectral Scanning System for Underground Mine and Tunnel Exploration*. 0–9. <https://doi.org/10.36227/techrxiv.21815508.v1>
- Kale, K. V., Solankar, M. M., Nalawade, D. B., Kale, K. V., Solankar, M. M., & Nalawade, D. B. (2019). Hyperspectral Endmember Extraction Techniques. *Processing and Analysis of Hyperspectral Data*. <https://doi.org/10.5772/INTECHOPEN.88910>
- Kirsch, M., Lorenz, S., Zimmermann, R., Tusa, L., Möckel, R., Hödl, P., Booyesen, R., Khodadadzadeh, M., & Gloaguen, R. (2018). Integration of terrestrial and drone-borne hyperspectral and photogrammetric sensing methods for exploration mapping and mining monitoring. *Remote Sensing*, 10(9). <https://doi.org/10.3390/rs10091366>
- Kirsch, M., Mavroudi, M., Thiele, S., Lorenz, S., Tusa, L., Herrmann, E., Fatihi, A., Möckel, R., & Dittrich, T. (2023a). *Underground hyperspectral outcrop scanning for automated mine-face mapping — the Lithium deposit of Zinnwald / Cínovec*. 1–22. <https://doi.org/10.1111/phor.12457>
- Kirsch, M., Mavroudi, M., Thiele, S. T., Lorenz, S., Tusa, L., Herrmann, E., Fatihi, A., Möckel, R., Dittrich, T., Mapping, L. F., Thiele, S. T., Bnoulkacem, Z., Lorenz, S., Bordenave, A., Menegoni, N., Madriz, Y., Dujoncquoy, E., Gloaguen, R., Kenter, J., ... Gloaguen, R. (2022). Mineralogical mapping with accurately corrected shortwave infrared hyperspectral data acquired obliquely from uavs. *Scientific Reports*, 70(1), 1–12. <https://doi.org/10.1111/1365-2478.13231>
- Kokaly, R. F., Clark, R. N., Swayze, G. A., Livo, K. E., Hoefen, T. M., Pearson, N. C., Wise, R. A., Benzel, W., Lowers, H. A., Driscoll, R. L., & Klein, A. J. (2017). USGS Spectral Library Version 7. *Data Series*. <https://doi.org/10.3133/DS1035>
- Koval, A., Karlsson, S., & Nikolakopoulos, G. (2022). Experimental evaluation of autonomous map-based Spot navigation in confined environments. *Biomimetic Intelligence and Robotics*, 2(1), 100035. <https://doi.org/10.1016/j.birob.2022.100035>
- Kurz, T. H., Buckley, S. J., Howell, J. A., & Schneider, D. (2011). Integration of panoramic hyperspectral imaging with terrestrial lidar data. *Photogrammetric Record*, 26(134), 212–228. <https://doi.org/10.1111/j.1477-9730.2011.00632.x>
- Laukamp, C., Rodger, A., LeGras, M., Lampinen, H., Lau, I. C., Pejčić, B., Stromberg, J., Francis, N., & Ramanaidou, E. (2021). *minerals Mineral Physicochemistry Underlying Feature-Based Extraction of Mineral Abundance and Composition from Shortwave, Mid and Thermal Infrared Reflectance Spectra*. <https://doi.org/10.3390/min11040347>

- Lindqvist, B., Karlsson, S., Koval, A., Tevetzidis, I., Haluška, J., Kanellakis, C., Agha-mohammadi, A. akbar, & Nikolakopoulos, G. (2022). Multimodality robotic systems: Integrated combined legged-aerial mobility for subterranean search-and-rescue. *Robotics and Autonomous Systems*, 154. <https://doi.org/10.1016/j.robot.2022.104134>
- Lu, B., Dao, P. D., Liu, J., He, Y., & Shang, J. (2020). Recent advances of hyperspectral imaging technology and applications in agriculture. *Remote Sensing*, 12(16), 1–44. <https://doi.org/10.3390/RS12162659>
- Mahmud, A. L. (2021). *Development of Collision Resilient Drone for Flying in Cluttered Development of Collision Resilient Drone for Flying in Cluttered Environment Environment*.
- Martino, R., Mccann, P., Ray, R. K., & Van Der Ende, O. (2021). *Digging deeper: Trends in underground hard-rock mining for gold and base metals*.
- Michalakopoulos, T. N. (2000). *Mine Planning and Equipment Selection* (Vol. 1).
- Michelsburg, M., & Puente Lé, F. (2018). *Spectral and spatial unmixing for material recognition in sorting plants*.
- Morenville, A. ;, Vermeulen, & Lucas. (2022). "Simultaneous localization and mapping and autonomous navigation on SPOT robot from Boston Dynamics." <http://hdl.handle.net/2078.1/thesis:35688>
- Müller, A., Herklotz, G., & Giegling, H. (2018). Chemistry of quartz related to the Zinnwald/Cínovec Sn-W-Li greisen-type deposit, Eastern Erzgebirge, Germany. *Journal of Geochemical Exploration*, 190, 357–373. <https://doi.org/10.1016/j.gexplo.2018.04.009>
- Murphy, R. J., & Monteiro, S. T. (2012). *Mapping the distribution of ferric iron minerals on a vertical mine face using derivative analysis of hyperspectral imagery (430-970 nm)*. <https://doi.org/10.1016/j.isprsjprs.2012.09.014>
- Nilsson, O. (2022). *Building dense reconstructions with SLAM and Spot*.
- Nwaila, G. T., Frimmel, H. E., Zhang, S. E., Bourdeau, J. E., Tolmay, L. C. K., Durrheim, R. J., & Ghorbani, Y. (2022). The minerals industry in the era of digital transition: An energy-efficient and environmentally conscious approach. *Resources Policy*, 78. <https://doi.org/10.1016/j.resourpol.2022.102851>
- Pontual, S., Merry, N., & Gamsom, P. (1997). GMEX Spectral Interpretation Field Manual. In *Spectral Analysis Guides for Mineral Exploratoin*. *GMEX AuSpec International Pty. Ltd.*, 92.
- Rieder, M. (1970). Chemical Composition and Physical Properties of Lithium-Iron Micas from the Krusne hory Mts. (Erzgebirge) Part A: Chemical Composition. In *Contr. Mineral. and Petrol* (Vol. 27).
- Romer, R. L., Thomas, R., Stein, H. J., & Rhede, D. (2007a). Dating multiply overprinted Sn-mineralized granites-examples from the Erzgebirge, Germany. *Miner Deposita*, 42, 337–359. <https://doi.org/10.1007/s00126-006-0114-2>

- Romer, R. L., Thomas, R., Stein, H. J., & Rhede, D. (2007b). Dating multiply overprinted Sn-mineralized granites-examples from the Erzgebirge, Germany. *Miner Deposita*, 42, 337–359. <https://doi.org/10.1007/s00126-006-0114-2>
- Sahu, H. B., Prakash, N., & Jayanthu, S. (2015). Underground Mining for Meeting Environmental Concerns – A Strategic Approach for Sustainable Mining in Future. *Procedia Earth and Planetary Science*, 11, 232–241. <https://doi.org/10.1016/j.proeps.2015.06.030>
- Savitzky, A., & E, M. J. (1951). Smoothing and Differentiation of Data by Simplified Least Squares Procedures. *Z. Physiol. Chem*, 40(2), 1832. <https://pubs.acs.org/sharingguidelines>
- Seifert, T., Atanasova, P., Gutzmer, J., & Pfander, J. (2011). *Mineralogy, geochemistry and age of greisen mineralization in the Li-Rb-Cs-Sn-W deposit*. [www.minersoc.org](http://www.minersoc.org)
- Štemprok, M., Holub, F. V., & Novák, J. K. (2003). Multiple magmatic pulses of the Eastern Volcano-Plutonic Complex, Krušné hory/Erzgebirge batholith, and their phosphorus contents. *Bulletin of Geosciences*, 78(3), 277–296.
- Štemprok, M., & Šulcek, Z. (1969). Geochemical profile through an ore-bearing lithium granite. *Economic Geology*, 64(4), 392–404. <https://doi.org/10.2113/gsecongeo.64.4.392>
- Stoch, L., & Sikora, W. (1976). Transformations of Micas in the Process of Kaolinitization of Granites and Gneisses. *Clays and Clay Minerals*, 24(4), 156–162. <https://doi.org/10.1346/ccmn.1976.0240402>
- Thiele, S. T., Lorenz, S., Kirsch, M., Cecilia Contreras Acosta, I., Tusa, L., Herrmann, E., Möckel, R., & Gloaguen, R. (2021). Multi-scale, multi-sensor data integration for automated 3-D geological mapping. *Ore Geology Reviews*, 136(May). <https://doi.org/10.1016/j.oregeorev.2021.104252>
- Tischendorf, G., & Förster, H. -J. (1990). Acid magmatism and related metallogensis in the Erzgebirge. *Geological Journal*, 25(3–4), 443–454. <https://doi.org/10.1002/GJ.3350250326>
- Tomek, F., Opluštil, S., Svojtka, M., Špillar, V., Rapprich, V., & Míková, J. (2022). Altenberg–Teplice Caldera sourced Westphalian fall tuffs in the central and western Bohemian Carboniferous basins (eastern Variscan belt). *International Geology Review*, 64(4), 441–468. <https://doi.org/10.1080/00206814.2020.1858357>
- van der Meer, F. D., van der Werff, H. M. A., van Ruitenbeek, F. J. A., Hecker, C. A., Bakker, W. H., Noomen, M. F., van der Meijde, M., Carranza, E. J. M., de Smeth, J. B., & Woldai, T. (2012). Multi- and hyperspectral geologic remote sensing: A review. *International Journal of Applied Earth Observation and Geoinformation*, 14(1), 112–128. <https://doi.org/10.1016/j.jag.2011.08.002>
- van Ruitenbeek, F. J. A., Debba, P., van der Meer, F. D., Cudahy, T., van der Meijde, M., & Hale, M. (2006). Mapping white micas and their absorption wavelengths using hyperspectral band ratios. *Remote Sensing of Environment*, 102(3–4), 211–222. <https://doi.org/10.1016/j.rse.2006.02.012>
- Velodyne LiDAR. (2015). *Velodyne LiDAR PUCK*.
- Velodyne LiDAR. (2019). *VLP-16 User Manual*. <http://www.velodynelidar.com/downloads.html#firmware>.

- Velodyne LiDAR. (2021). *VeloView User Guide User*. <https://www.paraview.org/VeloView>
- Velodyne LiDAR. (2023). *Velodyne driver ROS*. <https://github.com/ros-drivers/velodyne>
- Wang, R., Guo, Z., Chen, Y., Wang, X., & Chen, B. M. (2023). *Air Bumper: A Collision Detection and Reaction Framework for Autonomous MAV Navigation*.
- Wetzel, E. M., Liu, J., Leathem, T., & Sattineni, A. (2022). The Use of Boston Dynamics SPOT in Support of LiDAR Scanning on Active Construction Sites. *Proceedings of the International Symposium on Automation and Robotics in Construction, 2022-July*, 86–92. <https://doi.org/10.22260/isarc2022/0014>
- Whitney, D. L., & Evans, B. W. (2010). Abbreviations for names of rock-forming minerals. *American Mineralogist*, 95(1), 185–187. <https://doi.org/10.2138/am.2010.3371>
- Zhou, X., Jara, C., Bardoux, M., & Plasencia, C. (2017). Multi-Scale Integrated Application of Spectral Geology and Remote Sensing for Greenfield Gold Exploration. *Proceedings of Exploration: 6th Decennial International Conference on Mineral Exploration*, 17(November), 899–910.

# 8 Appendices

## Appendix A: MNF and PCA Output

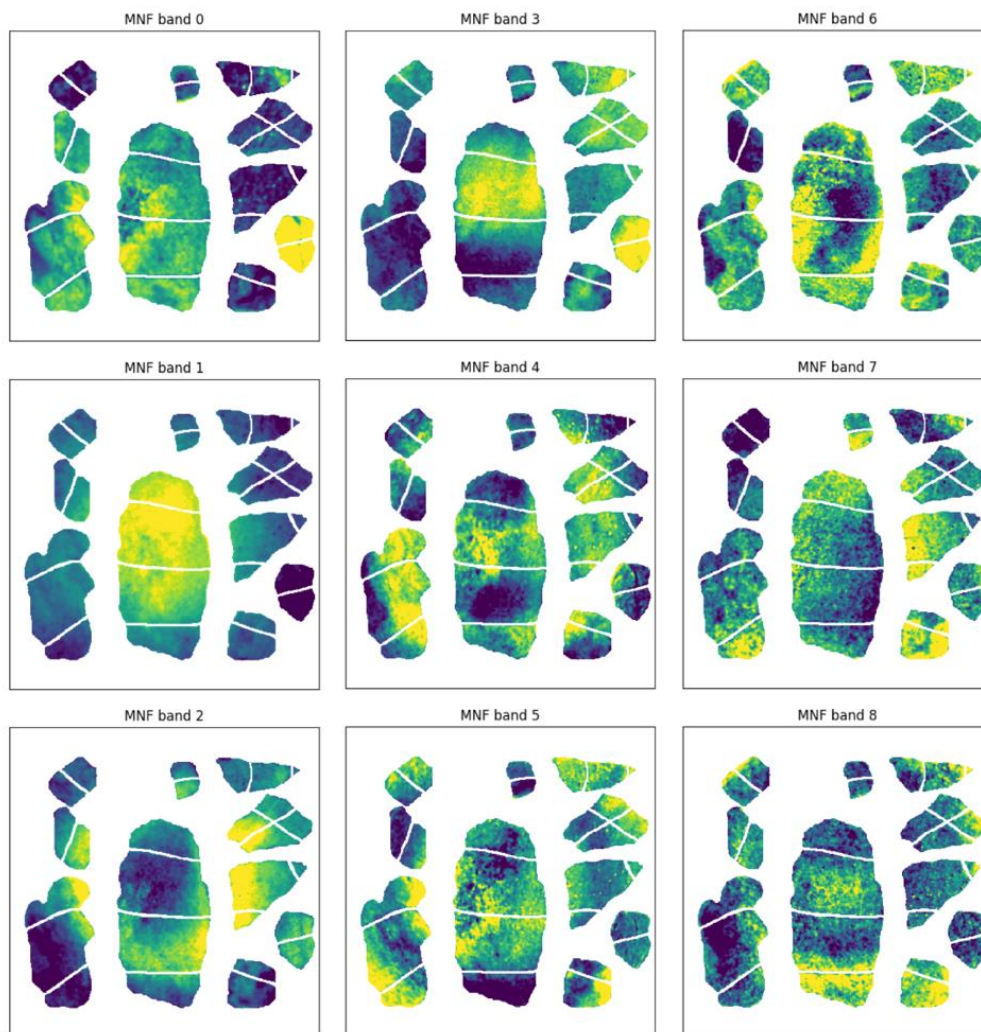


*Figure A-1. Lab application MNF output bands.*

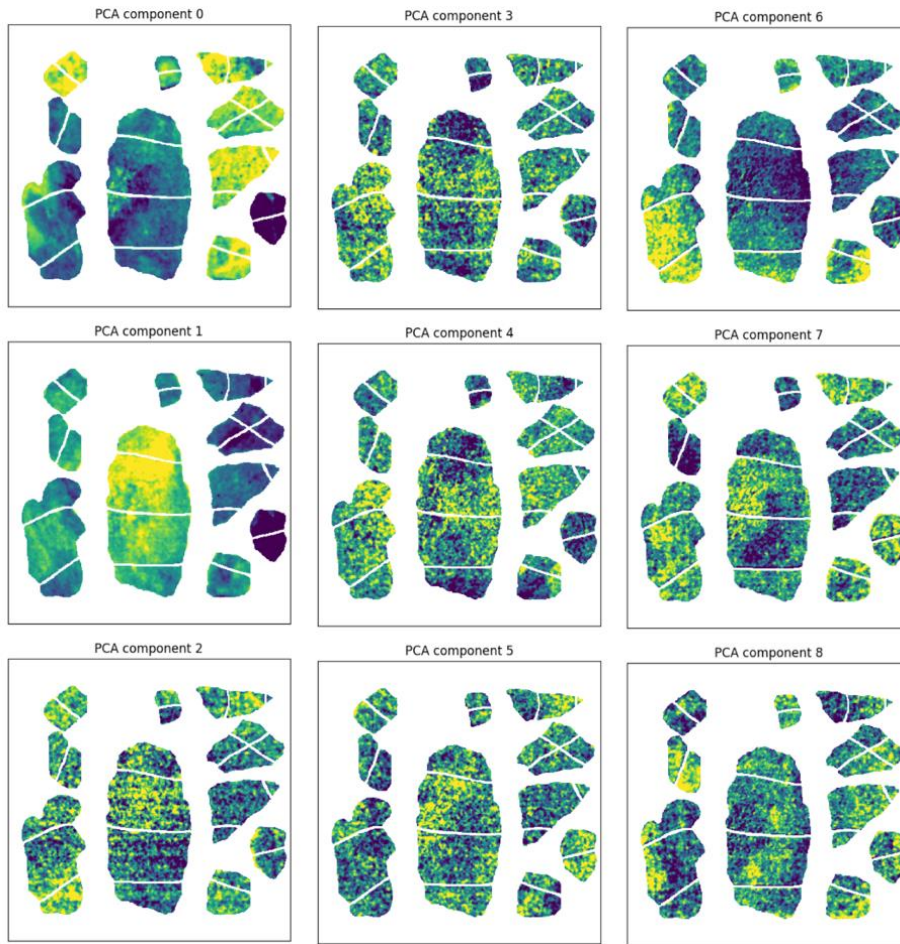


**Figure A-2.** Lab application PCA output components.

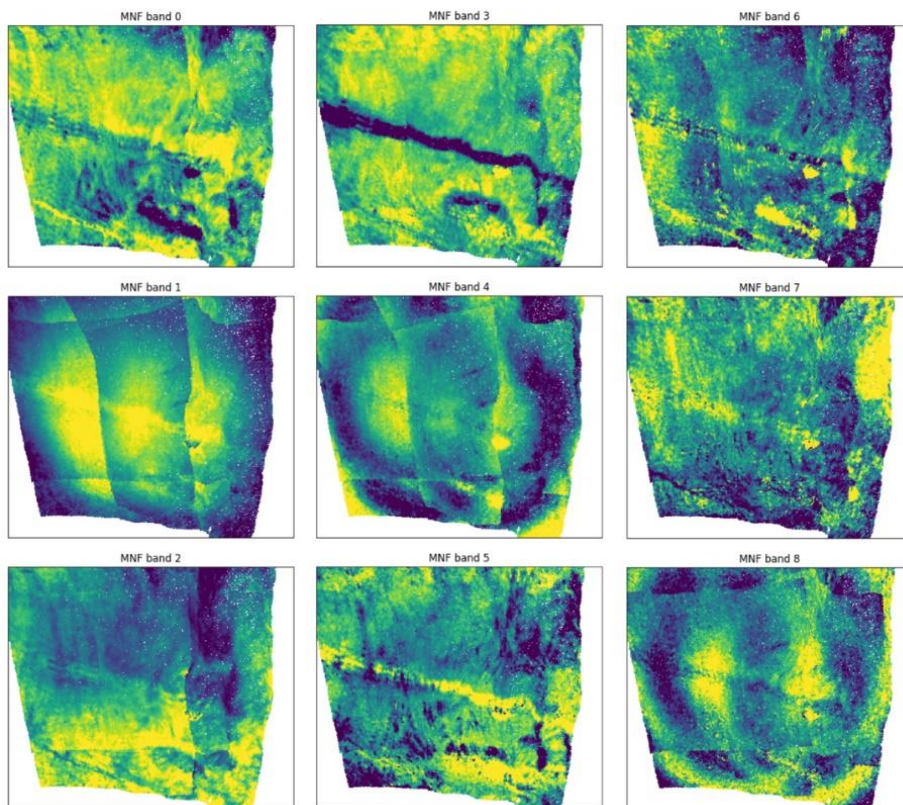


**Figure A-3.** UG-1 application MNF output bands.

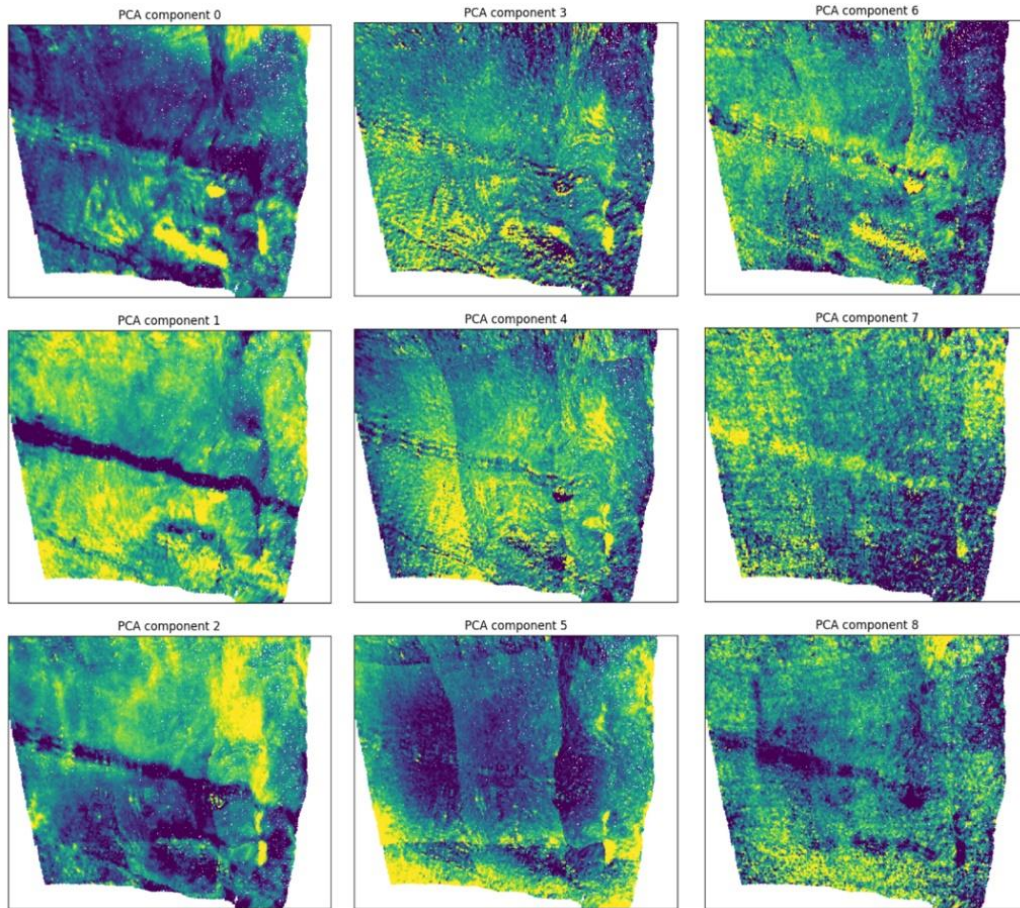


**Figure A-4.** UG-1 application PCA output components.

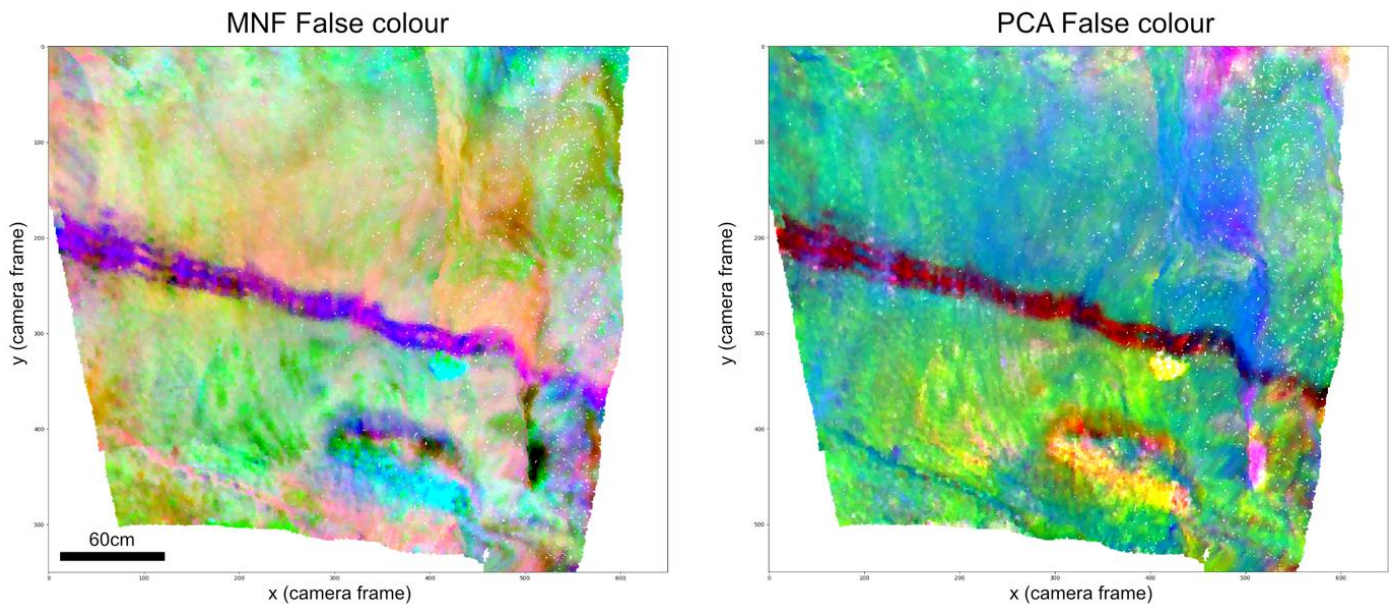


**Figure A-5.** UG-1 MNF and PCA false colour visualisation. Axes represent the frame of the defined custom camera object in hylite scenes.

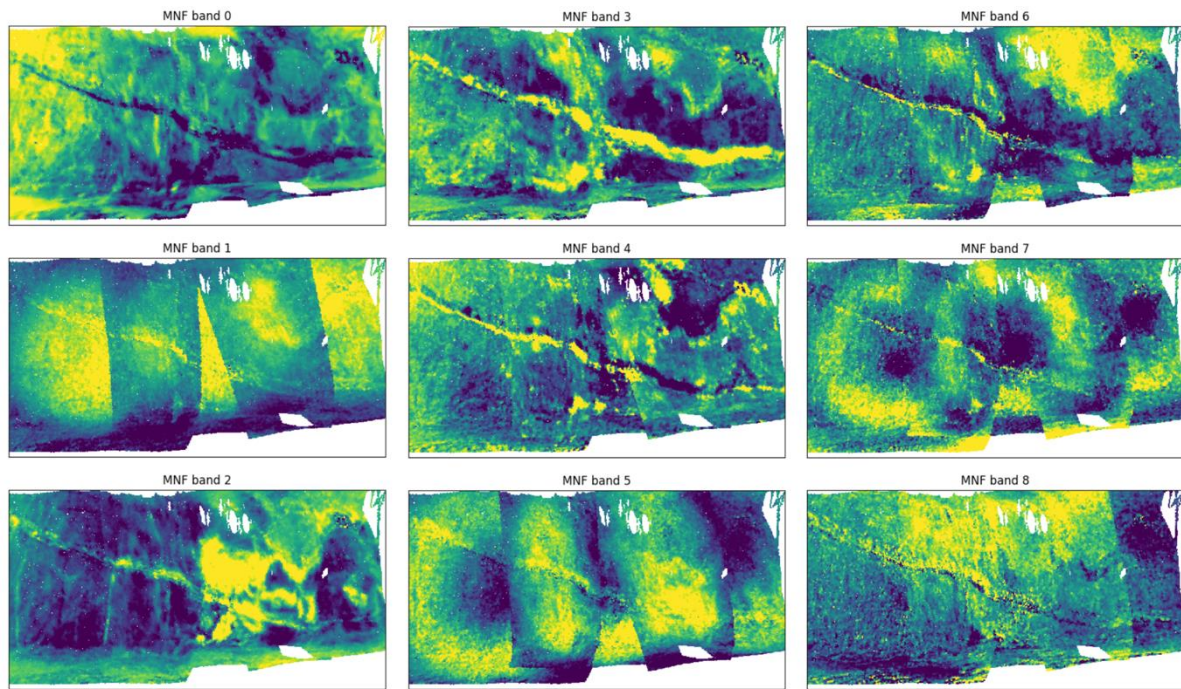


**Figure A-6.** UG-2 application MNF output bands.

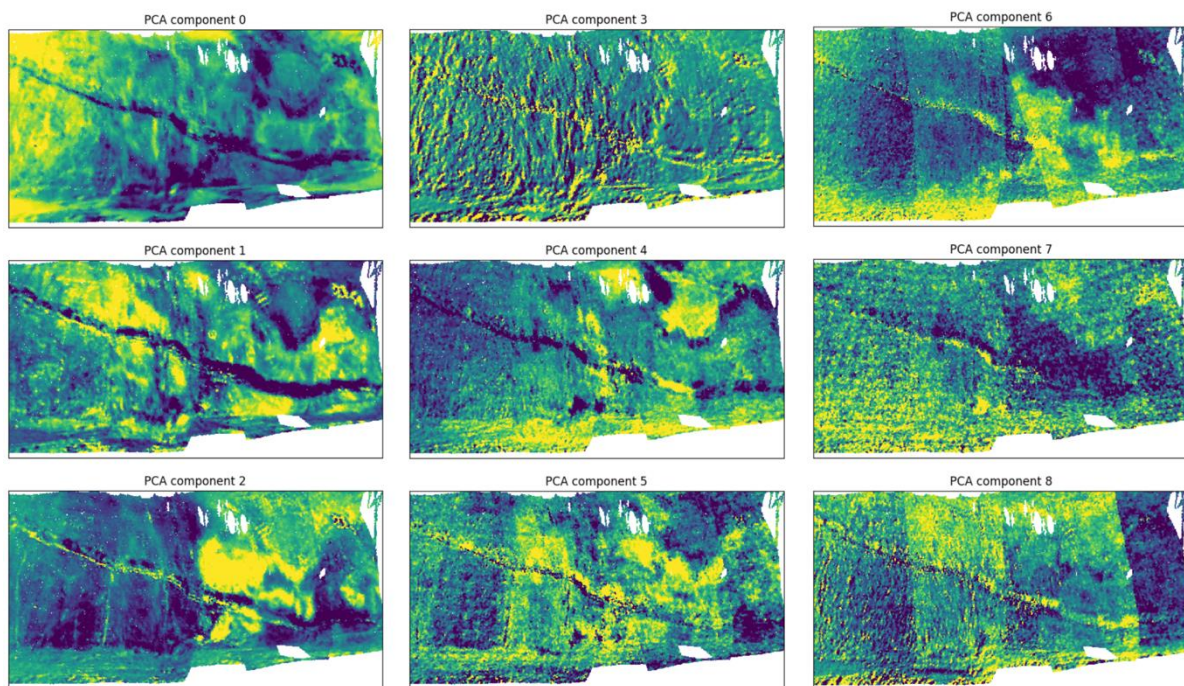


**Figure A-7.** UG-2 application PCA output components.

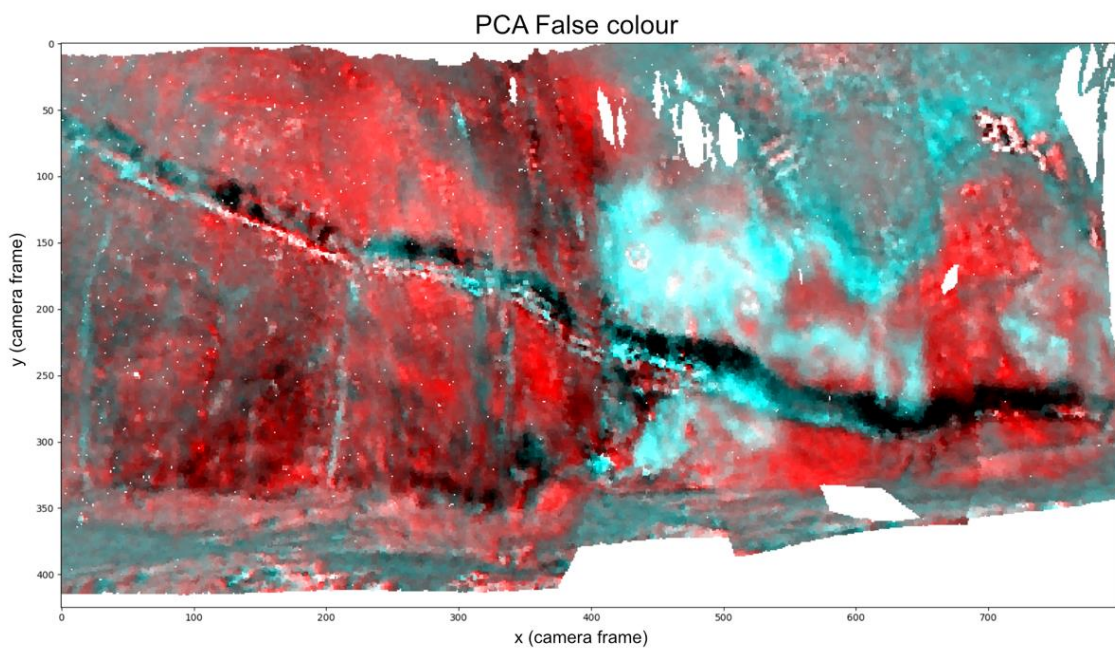
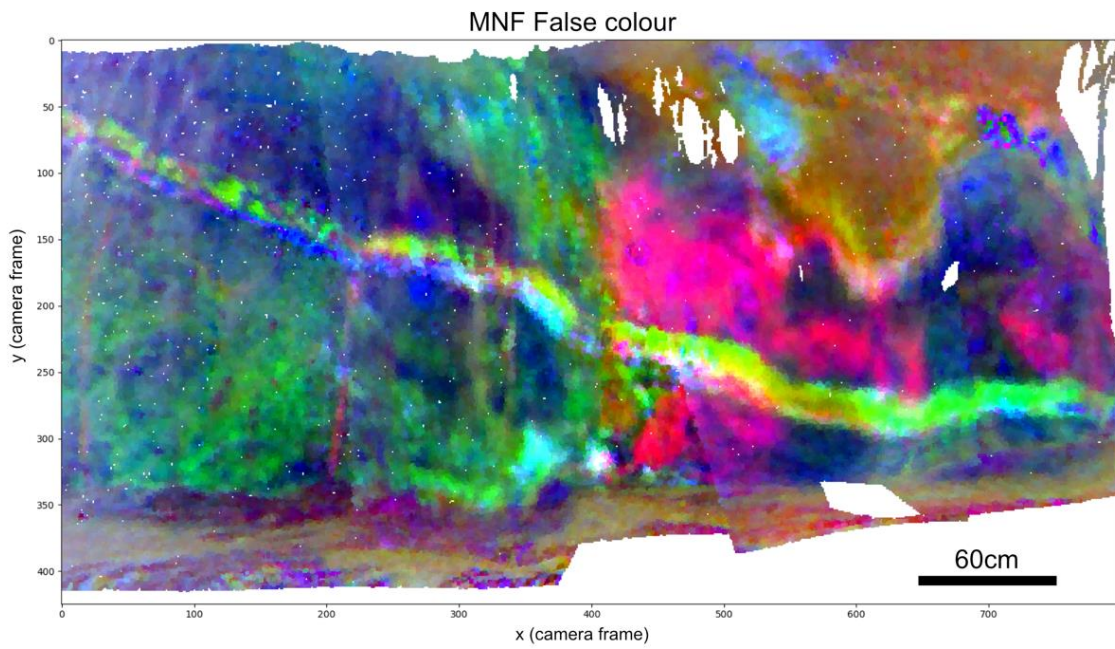


**Figure A-8.** UG-2 MNF and PCA false colour visualisation. Axes represent the frame of the defined custom camera object in hylite scenes.

## Appendix B: Analysis

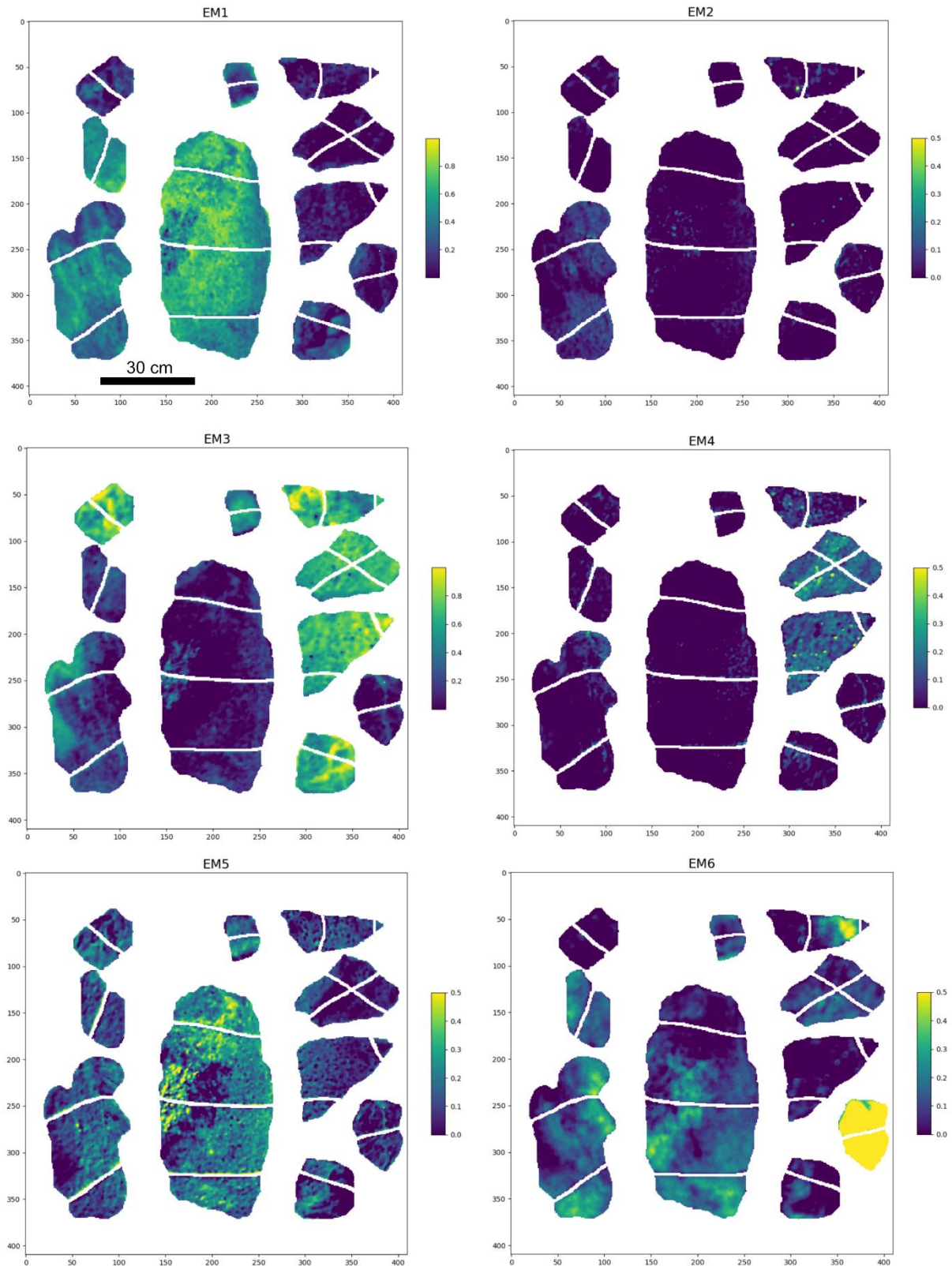


**Figure B-1.** Lab application endmember abundance maps. EM1, 3 and 6 colour bar in range 0.0 to 1. EM2, 4 and 5 with adjusted colourbar in range 0.0 to 0.5 in order to enhance visual differentiation of features.

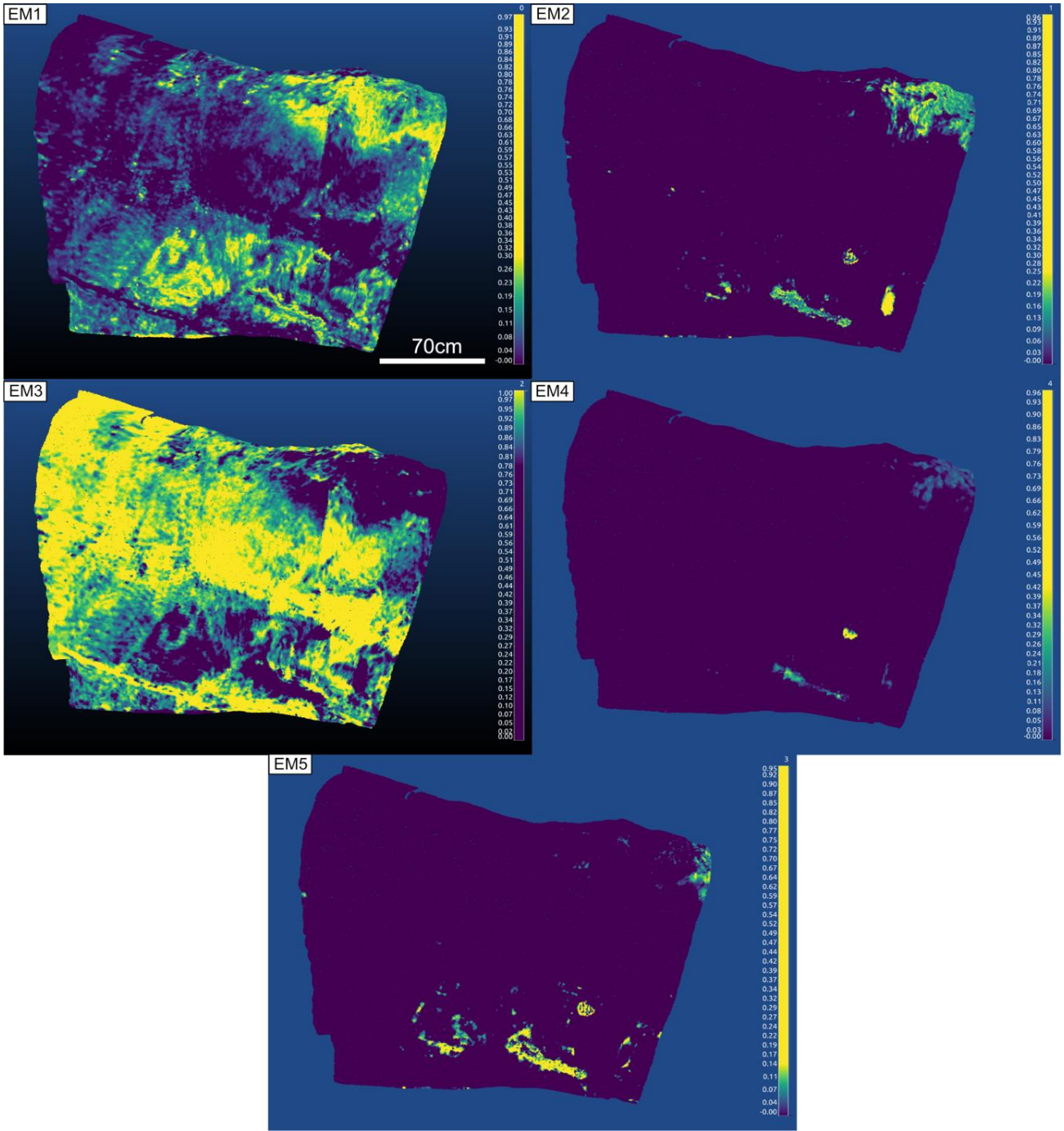


**Figure B-2.** UG-1 application endmember abundance maps. EM 3 with adjusted colourbar in order to enhance visual differentiation of low intensity features.

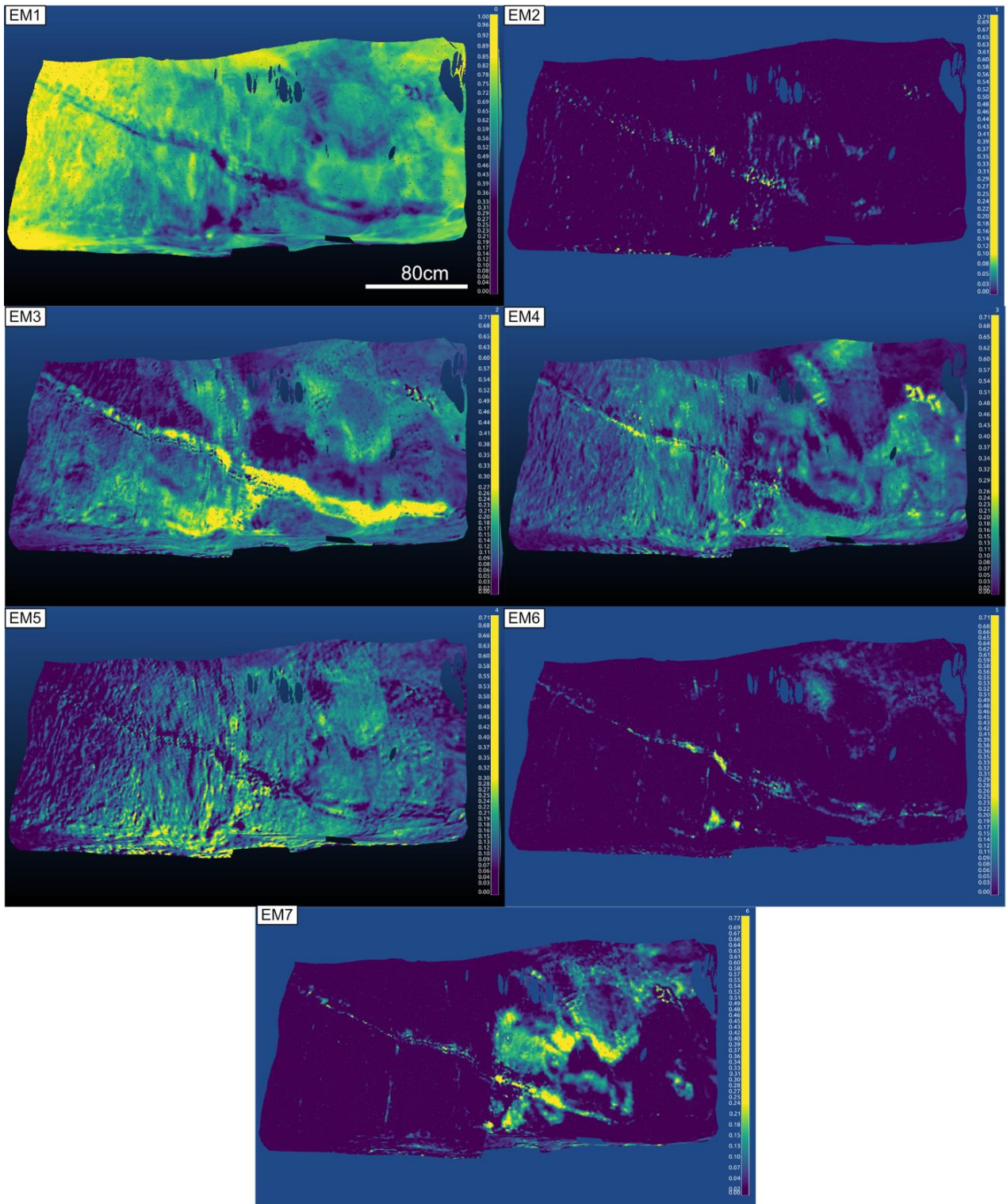


**Figure B-3.** UG-2 application endmember abundance maps. EM 1 with adjusted colourbar in order to enhance visual differentiation of low intensity features.

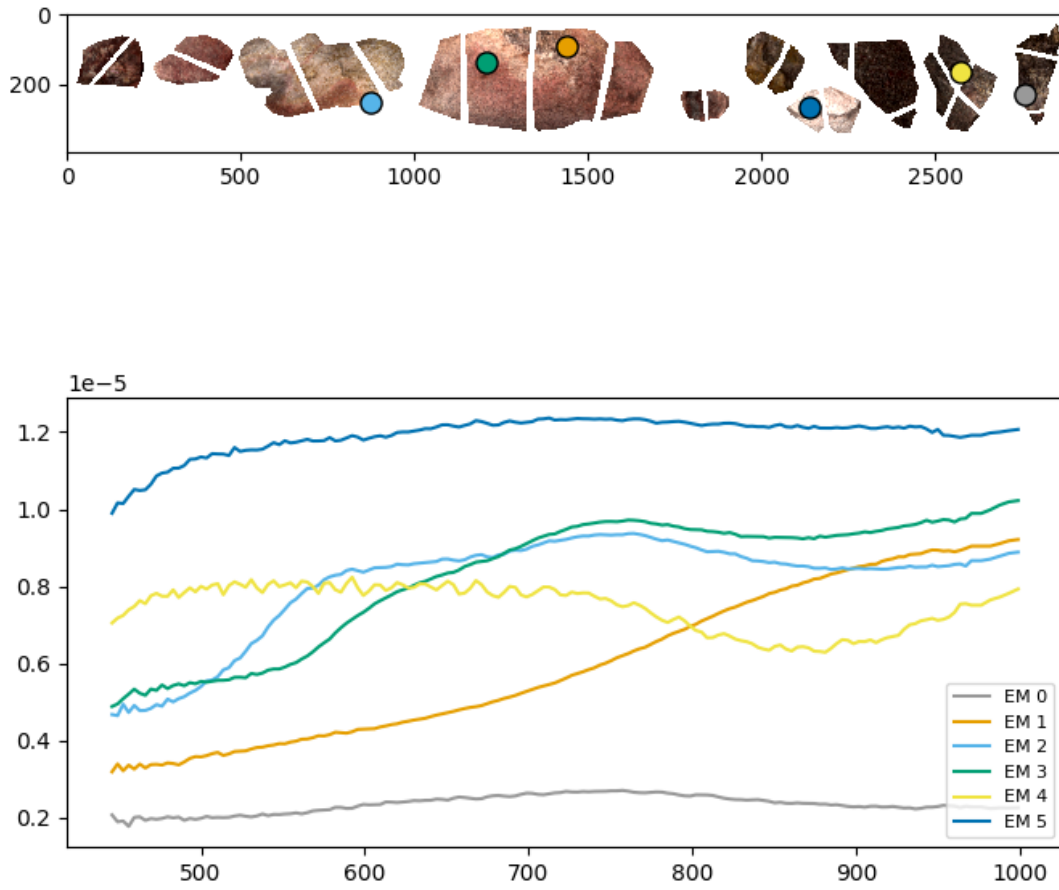


**Figure B-4.** Fenix endmember extraction RGB scatter plot and spectra on lab application rock samples.

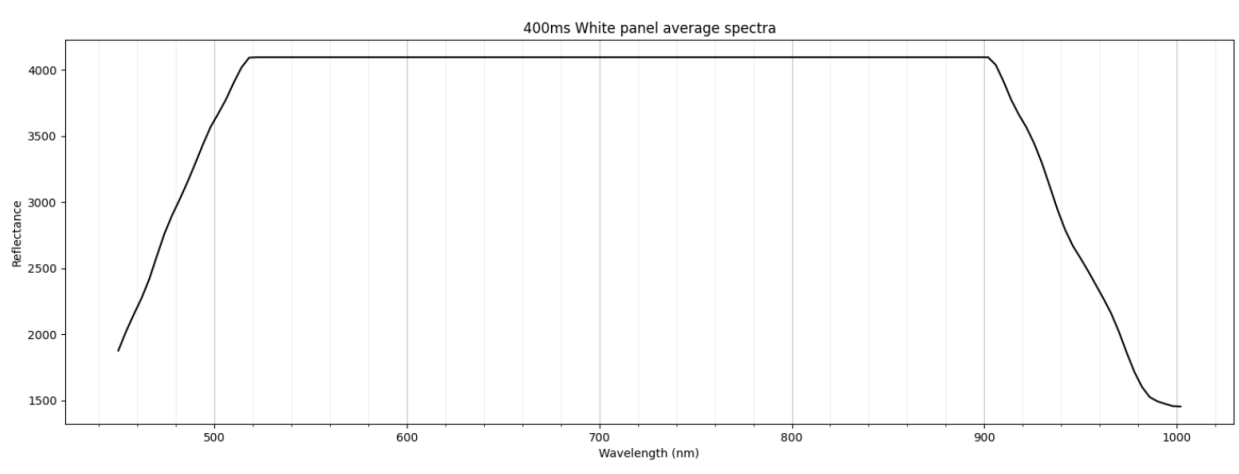
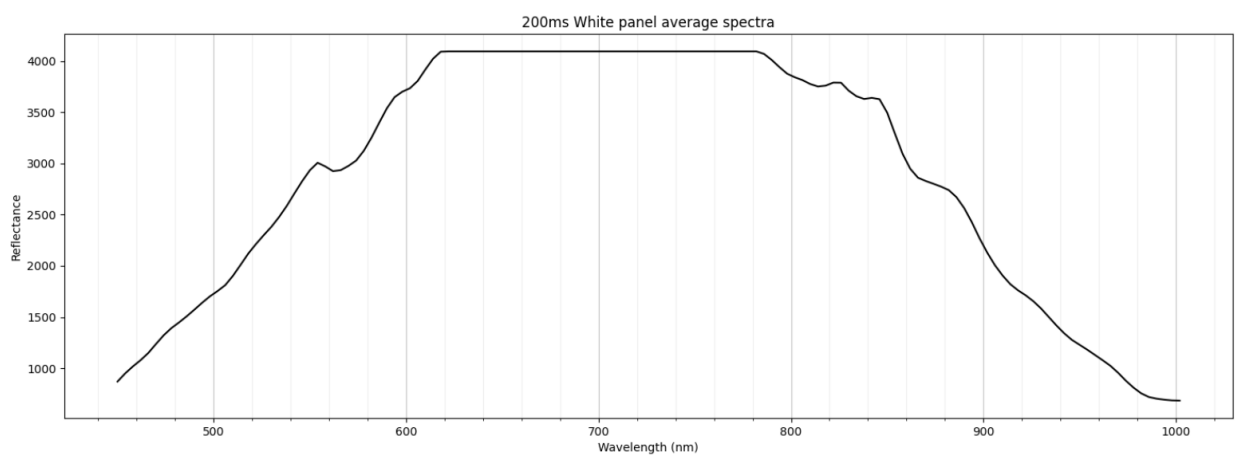
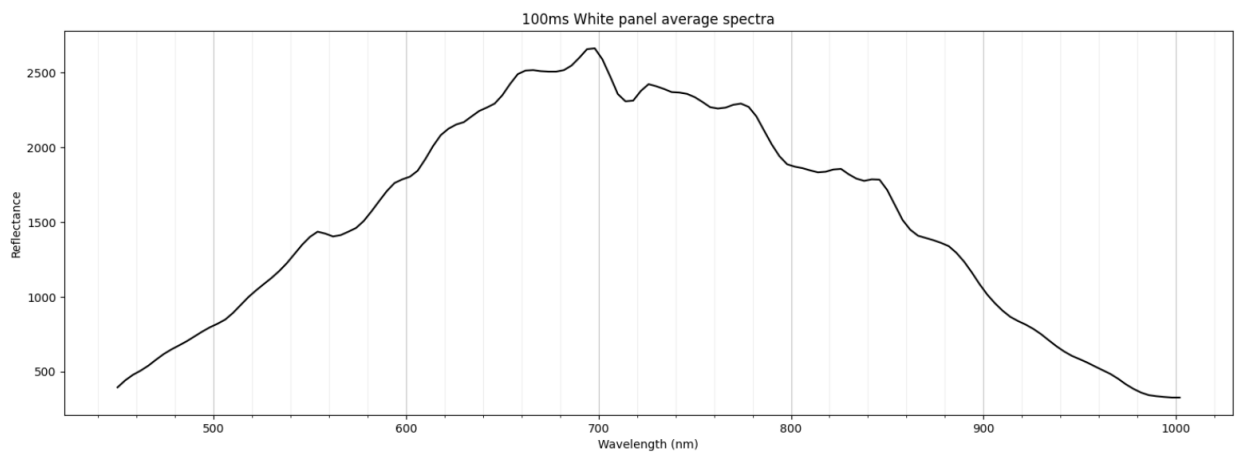


**Figure B-5.** Underground application white reference panel average spectra for 100, 200 and 400 ms exposure time.

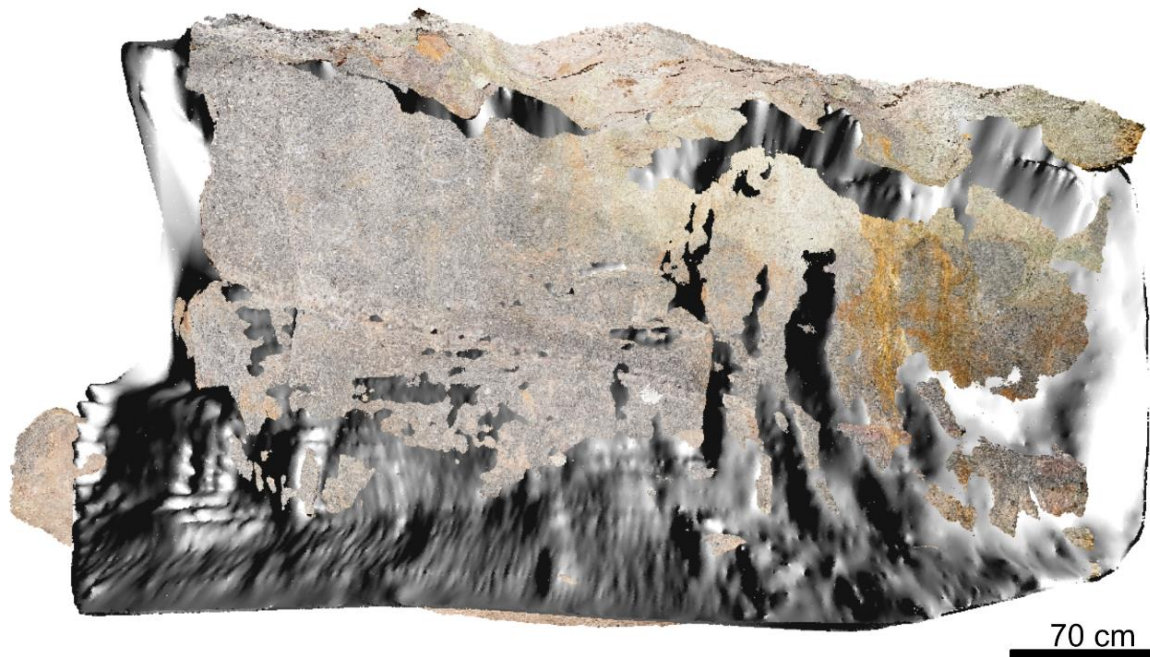


**Figure B-6.** Photogrammetry (coloured) and UG-1 (grey) raw pointcloud comparison.

## Appendix C: Digital Hyperclouds

Link: <https://www.hzdr.de/FWG/FWGE/Hyperclouds/Rex.html>

**Table C-1.** Digital hypercloud appendix legend with object name and description.

| Object name        | Description   |
|--------------------|---|
| Lab RGB            | Lab application RGB hypercloud.                             |
| Lab Fe3+           | Lab application Fe3+ band ratio hypercloud.                 |
| Lab EM1            | Lab application endmember 1 hypercloud.                     |
| Lab EM4            | Lab application endmember 4 hypercloud.                     |
| Lab EM6            | Lab application endmember 6 hypercloud.                     |
| Lab EM146 merge    | Endmember 1, 4 and 6 hypercloud RGB composite merge (Lab).  |
| UG cloud total     | Raw total underground Flöz 8 pointcloud.                    |
| UGP12 RGB          | UG-1 application RGB hypercloud.                            |
| UGP12 Fe3+         | UG-1 application Fe3+ band ratio hypercloud.                |
| UGP12 EM1          | UG-1 application endmember 1 hypercloud.                    |
| UGP12 EM2          | UG-1 application endmember 2 hypercloud.                    |
| UGP12 EM3          | UG-1 application endmember 3 hypercloud.                    |
| UGP12 EM132 merge  | Endmember 1, 3 and 2 hypercloud RGB composite merge (UG-1). |
| UGP345 RGB         | UG-2 application RGB hypercloud.                            |
| UGP345 Fe3+        | UG-2 application Fe3+ hypercloud.                           |
| UGP345 EM3         | UG-2 application endmember 3 hypercloud.                    |
| UGP345 EM4         | UG-2 application endmember 4 hypercloud.                    |
| UGP345 EM7         | UG-2 application endmember 7 hypercloud.                    |
| UGP345 EM347 merge | Endmember 3, 4 and 7 hypercloud RGB composite merge (UG-2). |

## Appendix D: Cubert X20P Manual for HIF

Link: <https://www.overleaf.com/read/ympnmpgcggy#f12d60>

## Appendix E: Operation and Data Acquisition Guide for HIF

Link: <https://www.overleaf.com/read/nxyqxyhsjxmk#72be3d>